

**İSTANBUL TECHNICAL UNIVERSITY ★ GRADUATE SCHOOL OF SCIENCE**  
**ENGINEERING AND TECHNOLOGY**

**EXPERIMENTAL INVESTIGATION OF LOCAL SCOUR PATTERNS  
AROUND HEXAGONALLY ARRAYED CYLINDER GROUPS**

**M.Sc. THESIS**

**Işıl YILDIRIM**

**Department of Civil Engineering**

**Hydraulics and Water Resources Engineering Programme**

**JUNE 2016**



**İSTANBUL TECHNICAL UNIVERSITY ★ GRADUATE SCHOOL OF SCIENCE**  
**ENGINEERING AND TECHNOLOGY**

**EXPERIMENTAL INVESTIGATION OF LOCAL SCOUR PATTERNS  
AROUND HEXAGONALLY ARRAYED CYLINDER GROUPS**

**M.Sc. THESIS**

**Işılso YILDIRIM  
(501141508)**

**Department of Civil Engineering**

**Hydraulics and Water Resources Engineering Programme**

**Thesis Advisor: Assoc. Prof. Dr. Oral YAĞCI**

**JUNE 2016**



**İSTANBUL TEKNİK ÜNİVERSİTESİ ★ FEN BİLİMLERİ ENSTİTÜSÜ**

**ALTİGEN DİZİLİMLİ SİLİNDİR GRUPLARI ETRAFINDAKİ YERSEL  
OYULMA DESENLERİNİN DENEYSEL OLARAK ARAŞTIRILMASI**

**YÜKSEK LİSANS TEZİ**

**Işılso YILDIRIM  
(501141508)**

**İnşaat Mühendisliği Anabilim Dalı**

**Hidrolik ve Su Kaynakları Mühendisliği Programı**

**Tez Danışmanı: Doç. Dr. Oral YAĞCI**

**HAZİRAN 2016**



Işılsu Yıldırım, a M.Sc. student of İTÜ Graduate School of Science Engineering and Technology student ID 501141508, successfully defended the thesis/dissertation entitled “EXPERIMENTAL INVESTIGATION OF LOCAL SCOUR PATTERNS AROUND HEXAGONALLY ARRAYED CYLINDER GROUPS”, which she prepared after fulfilling the requirements specified in the associated legislations, before the jury whose signatures are below.

**Thesis Advisor :**      **Assoc.Prof. Dr. Oral YAĞCI**      .....  
İstanbul Technical University

**Jury Members :**      **Prof. Dr. Hafzullah AKSOY**      .....  
İstanbul Technical University

**Prof. Dr. Yalçın YÜKSEL**      .....  
Yıldız Technical University

**Date of Submission : 2 May 2016**

**Date of Defense : 6 June 2016**





*To my family and friends,*



## FOREWORD

This thesis is written during my Master of Science study at Istanbul Technical University where I am proud to be a part of. As I was studied to be a civil engineer, I realised that every decision we make, creates a difference in the world and we can choose our designs as engineers and our actions as human beings in order to make this planet a better place. Science is one of the best ways to do so. I was lucky enough to work with a scientist who sees science the same way as me. This is the greatest reason why I would like to thank my supervisor Assoc. Prof. Dr. Oral Yağcı. His way of teaching and his great perspective helped me to study joyfully.

I would like to thank Research Assistant Mehmet Furkan Çelik for giving me an incredibly valuable technical support by creating the three dimensional models for the experiments. Without him, this study would be incomplete.

Another important person I would like to thank is my fellow traveller on this road, Research Assistant Dila Demiral who is always by my side when I need her. She is a lifetime friend who I can trust on anything I can imagine.

I would like to thank Assoc. Prof. Dr. Özgür Kırca, Dr. Vasileios Kitsikoudis and Dr. Jafar Safari who helped and support me in the creation of this thesis.

During the experiments Mevlüt Uluçınar, Hasan Yalçın and Yaşar Aktaş helped me for experimental setup and they gave me valuable advices on life. I would like to thank them for these reasons.

Friends are family by choice. I would like to thank my choosen family for always being there for me. Nothing in my life would be this good without İlkin, Gülce and Burak. I would never be this happy without the ever similing face and positivity of Seda who makes our apartment a lovely home. I would not spend the nights of long, tiring days by laughing without Banu and Pınar. My days in the university would not be the greatest times of my life without Anıl and Emre Can. I would not love this city as much as I do now without Ayşe. They all are the creators of my happiest moments. I cannot thank them enough.

I would like to thank my cousins who are like my sisters and brothers. Special thanks to Eviş who is my mentor in life and Begüm who is one of the most important people in my life.

Finally, I would like to give my special thanks to my family. My mother, who is the greatest support of my life, thought me how to be a strong woman and how to believe in myself. My father, who is the smartest person I know, thought me love and trust is the key for everything by loving and trusting me endlessly. My lovely sister who always makes me feel like I am the most important part of her life, thought me that I can be myself even in the hardest times. They gave me love and support all my life and I could not be luckier.

May 2016

Işıl YILDIRIM  
(Civil Engineer)



## TABLE OF CONTENTS

	<u>Page</u>
<b>FOREWORD .....</b>	<b>ix</b>
<b>TABLE OF CONTENTS.....</b>	<b>xi</b>
<b>ABBREVIATIONS .....</b>	<b>xiii</b>
<b>SYMBOLS .....</b>	<b>xv</b>
<b>LIST OF TABLES .....</b>	<b>xvii</b>
<b>LIST OF FIGURES .....</b>	<b>xix</b>
<b>SUMMARY .....</b>	<b>xxvi</b>
<b>ÖZET .....</b>	<b>xxix</b>
<b>1. INTRODUCTION.....</b>	<b>1</b>
1.1 Aim of the Study .....	1
1.2 Fundamental Background .....	3
1.2.1 Flow around a cylinder body .....	3
1.2.2 Scour around a cylindrical body .....	4
1.2.3 Scour depth .....	4
1.2.3.1 Shields parameter .....	5
1.2.3.2 Sediment gradation.....	6
1.2.3.3 Boundary layer depth to pile size ratio .....	6
1.2.3.4 Sediment size to pile size ratio .....	7
1.2.3.5 The shape factor .....	7
1.2.3.6 The alingment factor .....	7
1.3 Literature Review .....	8
1.3.1 Flow-altering countermeasures against scour around bridge piers .....	8
1.3.2 Flow and scour around porous structures and pile groups .....	10
<b>2. EXPERIMENTAL SETUP .....</b>	<b>21</b>
2.1 Experimental Facilities .....	21
2.1.1 The flume .....	21
2.1.2 The bed material.....	22
2.1.3 The pumps.....	23
2.1.4 The measurement devices .....	23
2.2 Model Pile Characteristics .....	24
2.3 Experimental Procedure .....	25
<b>3. RESULTS AND DISCUSSION .....</b>	<b>29</b>
3.1 The Change in the Bottom Distance Over Time .....	30
3.2 Comparison of HACCs with 9 cm Solid Cylinder .....	35
3.3 The Change in Velocities in Three Dimensions.....	36
3.4 Pattern Based Assesments .....	37
3.5 The Morphometric Analysis.....	47
<b>4. CONCLUSIONS AND RECOMMENDATIONS.....</b>	<b>53</b>
<b>REFERENCES .....</b>	<b>57</b>
<b>APPENDICES .....</b>	<b>59</b>
<b>APPENDIX A .....</b>	<b>61</b>
<b>APPENDIX B .....</b>	<b>69</b>

<b>CURRICULUM VITAE .....</b>	<b>77</b>
-------------------------------	-----------

## **ABBREVIATIONS**

**ADV** : Acoustic Doppler Velocimeter  
**HACC** : Hexagonally Arrayed Circular Cylinders





## SYMBOLS

$A$	: Cross-sectional area of the flow
$D$	: Circumambient cylinder diameter
$D_h$	: Deposition height
$D_v$	: Deposition volume
$D_a$	: Deposition area
$d$	: Cylinder diameter
$g$	: Acceleration of gravity
$I_u$	: Upstream slope of the scour hole
$I_d$	: Downstream slope of the scour hole
$J$	: Bed elevation
$L_d$	: The length between the top point of deposition and cylinder center
$Q$	: Flow discharge
$q$	: Discharge per unit width
$R$	: Hydraulic radius
$r_{ds}$	: The efficiency of scour depth reduction
$r_{ws}$	: The efficiency of scour width reduction
$r_{vs}$	: The efficiency of scour volume reduction
$S_a$	: Scour area
$S_d$	: Scour depth
$S_v$	: Scour volume
$S_w$	: Scour width
$t$	: Time
$U$	: Wetted perimeter
$u, v, w$	: Velocities in directions $x, y, z$
$u_f$	: Skin friction velocity
$\theta$	: Shields parameter
$\theta_{cr}$	: Critical Shields parameter
$\rho$	: Density of water
$\gamma$	: Specific weight of water
$\tau$	: Bed shear stress in undisturbed bed
$\Psi$	: Packing density



## LIST OF TABLES

	<u>Page</u>
<b>Table 2.1</b> : Geometric characteristics of obstacle types. ....	<b>25</b>
<b>Table 2.2</b> : The experimental characteristics.....	<b>28</b>
<b>Table 3.1</b> : The efficiencies of HACCs according to 9 cm solid cylinder. ....	<b>36</b>
<b>Table 3.2</b> : The morphometric parameters for each experiment. ....	<b>47</b>
<b>Table 3.3</b> : Packing densities belonging to the different configurations of HACCs. ....	<b>48</b>



## LIST OF FIGURES

	<u>Page</u>
<b>Figure 1.1</b> : Flow pattern around the bridge pier (Nohani et al., 2015). ....	3
<b>Figure 1.2</b> : The Shields diagram giving the threshold value $\theta_c$ as a function of Re (Fredsoe and Deigaard, 1992; p.203). ....	5
<b>Figure 1.3</b> : Scour depth against Shields parameter for uniform sediment. (Melville and Coleman, 2000; Sumer and Fredsoe, 2002, p.178). ....	6
<b>Figure 1.4</b> : Effect of sediment size. Data compiled by (Melville and Sutherland, 1988; Sumer and Fredsoe, 2002, p.180). ....	7
<b>Figure 1.5</b> : Effect of alignment. (Laursen, 1958; Sumer and Fredsoe, 2002, p.183). ....	8
<b>Figure 1.6</b> : Flow-altering countermeasures: (a) submerged vanes; (b) bed sill; (c) sacrificial piles; (d) collar; (e) threading; (f) pier slot (Tafarojnoruz et al., 2012). ....	9
<b>Figure 1.7</b> : Pier groups: (a) Full; (b) Partial; and (c) Full with Collar (Vittal et al, 1994).....	10
<b>Figure 1.8</b> : Approach Flows: (a) 0°; (b) 15°; (c) 30°, (d) 45°; and (e) 60° (Vittal et al, 1994).....	10
<b>Figure 1.9</b> : Pile-group configurations used in the study of Sumer et al. (2005). ....	11
<b>Figure 1.10</b> : Test conditions for scour experiments. Water depth=0.25 m. Circular group with same pile density as in 5 x 5 group. (Sumer et al., 2005) ....	11
<b>Figure 1.11</b> : Time development of scour, live bed, G/D=4 (Sumer et al., 2005). ...	12
<b>Figure 1.12</b> : Equilibrium scour profiles for 2-pile, side-by-side arrangement pile group, live bed, G/D=4 (Sumer et al., 2005). ....	12
<b>Figure 1.13</b> : Pile groups used in experiments (Ataie-Ashtiani and Beheshti, 2006).....	13
<b>Figure 1.14</b> : Equilibrium scour depth plotted against pile spacing: (a) 1x2 pile group; (b) 2x1 pile group (Ataie-Ashtiani and Beheshti, 2006).....	14
<b>Figure 1.15</b> : Definition of the colony model and measurement points of velocity. D:diameter of cylinder, L:spacing of the cylinders, $D_c$ : outer diameter of the colony model, G: spacing of each cylinder in cross-stream direction, the number inside the cylinder, e.g., A1, distinguishes each cylinder's position. (a) grid arrangement, (b) staggered arrangement. The velocity of the detour flow past the colony model and the velocity through the colony model are measured at points indicated by closed circles (Ataie-Ashtiani and Beheshti, 2006).....	15
<b>Figure 1.16</b> : Visualized flow pattern around the colony model with a grid arrangement for $U = 0.4\text{m/s}$ . (a) $L/D = 3$ , (b) $L/D = 0.5$ . The arrow shows the flow direction. $l_s$ is the width of the separation zone in front of the first cylinder at the upstream. (Takemura and Tanaka, 2007).....	15
<b>Figure 1.17</b> : Flow pattern in the wake of the colony model. (a) $L/D = 0.5$ , grid arrangement ( $Re = 400$ ; the zoom photograph is inserted at the upper left corner, (b) $L/D = 0.5$ , grid arrangement ( $Re = 4000$ ), (c) $L/D = 3$ , grid arrangement ( $Re = 400$ ), (d) $L/D = 3$ , grid arrangement ( $Re = 4000$ ), (e) $L/D = 0.5$ , staggered arrangement ( $Re = 400$ ) and (f) $L/D = 3$ , staggered arrangement ( $Re = 400$ ). The small arrows show the positions of LKV	

((a), (b) and (e)) or PKV ((c), (d) and (f)) behind the colony model (Takemura and Tanaka, 2007). .....	16
<b>Figure 1.18</b> : Top view of experiment setup. (a) Patch configuration and dye injection points; (b) longitudinal and lateral transects (dashed lines) of velocity measurements. $x = 0$ is at the upstream edge of the patch, $y = 0$ is at the centreline of the patch (Zong and Nepf, 2011). .....	16
<b>Figure 1.19</b> : Longitudinal profiles of velocity for patches with $D = 42$ cm: (a) solid body, $\phi = 1$ , (b) $\phi = 0.10$ , (c) $\phi = 0.03$ . Patch is from $0 < x = D < 1$ . The dashed line indicates the downstream end of the patch. Note that the longitudinal velocity (open circles) is given on the left-hand axis, and the lateral velocity (filled circles) is given on the right-hand axis. The longitudinal velocity ( $u$ ) is measured at centreline, $y = 0$ . The lateral velocity ( $v$ ) is measured at $y = D/2$ (Zong and Nepf, 2011). .....	17
<b>Figure 1.20</b> : Flow visualization. The patch is just out of sight at the bottom of each picture. Flow is from bottom to top. The dye was injected at the two outmost edges of the patch. The struts holding the dye injector are visible in some of the pictures. The white grid starts at $x = 50$ cm (from the leading edge of the patch) and marks the distance of 50 cm in the $x$ - direction and 20 cm in the $y$ -direction. The yellow crosses mark 1 m intervals. The horizontal White bar indicates the end of the steady wake. (Zong and Nepf, 2011). .....	18
<b>Figure 1.21</b> : Top view of a circular patch of emergent vegetation, shown by dark gray circle of diameter $D$ . Injections of dye at the outer edges of patch (thick gray lines) reveal the evolution of the wake. Velocity exiting the patch ( $U_e = u(x = D)$ ) is diminished relative to upstream velocity ( $U_\infty$ ). The velocity decreases further to the steady wake region ( $U_1$ ). The flow within the wake delays the onset of the von Karman vortex street to the end of the steady wake, $x = L_1 + D$ . The wake contains two scales of turbulence: stem-scale turbulence (shown with small thin semicircles), which peaks within the patch, and patch-scale turbulence (black circles with arrows), which peaks at $x = L_w + D$ (Chen et al., 2012). .....	19
<b>Figure 2.1</b> : Drawing of the flume where the experiments were conducted. ....	21
<b>Figure 2.2</b> : The flume where the experiments were conducted. ....	21
<b>Figure 2.3</b> : Details of the sand bottom and drainage pipes. ....	22
<b>Figure 2.4</b> : Grains size distribution for sand samples. ....	22
<b>Figure 2.5</b> : The laser scanner. ....	24
<b>Figure 2.6</b> : The perspective view of the HACCs which were used in the experiments. ....	24
<b>Figure 2.7</b> : The geometry of the obstacles. ....	25
<b>Figure 2.8</b> : The experimental configurations and orientations. ....	25
<b>Figure 2.9</b> : Preparation of the flume. ....	26
<b>Figure 2.10</b> : Vectrino II in front of the 16 cm staggered HACC. ....	26
<b>Figure 2.11</b> : Position of Vectrino II. ....	27
<b>Figure 3.1</b> : Scour hole and deposition zone for 20 cm regular HACC. ....	29
<b>Figure 3.2</b> : The final bed topographies for (a) 12 cm staggered HACC, (b) 16 cm staggered HACC, (c) 20 cm staggered HACC and (d) 24 cm staggered HACC. ....	29
<b>Figure 3.3</b> : Scour hole and deposition zone for 24 cm angled HACC. ....	30
<b>Figure 3.4</b> : The variation of scour depth with respect to time observed throughout the experiments for 12 cm HACC cases. ....	30

<b>Figure 3.5 :</b> The variation of scour depth with respect to time observed throughout the experiments for 16 cm HACC cases. ....	<b>31</b>
<b>Figure 3.6 :</b> The variation of scour depth with respect to time observed throughout the experiments for 20 cm HACC cases. ....	<b>32</b>
<b>Figure 3.7 :</b> The variation of scour depth with respect to time observed throughout the experiments for 24 cm HACC cases. ....	<b>32</b>
<b>Figure 3.8 :</b> The variation of scour depth with respect to time observed throughout the experiments for solid cylinder cases. ....	<b>33</b>
<b>Figure 3.9 :</b> The variation of scour depth with respect to time observed throughout the experiments for regular HACC cases. ....	<b>33</b>
<b>Figure 3.10 :</b> The variation of scour depth with respect to time observed throughout the experiments for staggered HACC cases. ....	<b>34</b>
<b>Figure 3.11 :</b> The variation of scour depth with respect to time observed throughout the experiments for angled HACC cases. ....	<b>34</b>
<b>Figure 3.12 :</b> Digital model of final bed topography for 9 cm solid cylinder (The dimensions on the figure are in mm and the dimensions on the legend are in cm). ....	<b>37</b>
<b>Figure 3.13 :</b> Digital model of final bed topography for 12 cm solid cylinder (The dimensions on the figure are in mm and the dimensions on the legend are in cm). ....	<b>37</b>
<b>Figure 3.14 :</b> Digital model of final bed topography for 16 cm solid cylinder (The dimensions on the figure are in mm and the dimensions on the legend are in cm). ....	<b>38</b>
<b>Figure 3.15 :</b> Digital model of final bed topography for 20 cm solid cylinder (The dimensions on the figure are in mm and the dimensions on the legend are in cm). ....	<b>38</b>
<b>Figure 3.16 :</b> Digital model of final bed topography for 12 cm regular HACC (The dimensions on the figure are in mm and the dimensions on the legend are in cm). ....	<b>39</b>
<b>Figure 3.17 :</b> Digital model of final bed topography for 12 cm staggered HACC (The dimensions on the figure are in mm and the dimensions on the legend are in cm). ....	<b>39</b>
<b>Figure 3.18 :</b> Digital model of final bed topography for 12 cm angled HACC (The dimensions on the figure are in mm and the dimensions on the legend are in cm). ....	<b>40</b>
<b>Figure 3.19 :</b> Longitudinal view of 12 cm HACC experiments for final bed topography (The dimensions are in mm). ....	<b>40</b>
<b>Figure 3.20 :</b> Cross-section view of 12 cm HACC experiments for final bed topography (The dimensions are in mm). ....	<b>40</b>
<b>Figure 3.21 :</b> Digital model of final bed topography for 16 cm regular HACC (The dimensions on the figure are in mm and the dimensions on the legend are in cm). ....	<b>41</b>
<b>Figure 3.22 :</b> Digital model of final bed topography for 16 cm staggered HACC (The dimensions on the figure are in mm and the dimensions on the legend are in cm). ....	<b>41</b>
<b>Figure 3.23 :</b> Digital model of final bed topography for 16 cm angled HACC (The dimensions on the figure are in mm and the dimensions on the legend are in cm). ....	<b>42</b>
<b>Figure 3.24 :</b> Longitudinal view of 16 cm HACC experiments for final bed topography (The dimensions are in mm). ....	<b>42</b>

<b>Figure 3.25 :</b> Cross-section view of 16 cm HACC experiments for final bed topography (The dimensions are in mm).....	<b>42</b>
<b>Figure 3.26 :</b> Digital model of final bed topography for 20 cm regular HACC (The dimensions on the figure are in mm and the dimensions on the legend are in cm). ....	<b>43</b>
<b>Figure 3.27 :</b> Digital model of final bed topography for 20 cm staggered HACC (The dimensions on the figure are in mm and the dimensions on the legend are in cm). ....	<b>43</b>
<b>Figure 3.28 :</b> Digital model of final bed topography for 20 cm angled HACC (The dimensions on the figure are in mm and the dimensions on the legend are in cm). ....	<b>44</b>
<b>Figure 3.29 :</b> Longitudinal view of 20 cm HACC experiments for final bed topography (The dimensions are in mm).....	<b>44</b>
<b>Figure 3.30 :</b> Cross-section view of 20 cm HACC experiments for final bed topography (The dimensions are in mm).....	<b>44</b>
<b>Figure 3.31 :</b> Digital model of final bed topography for 24 cm regular HACC (The dimensions on the figure are in mm and the dimensions on the legend are in cm). ....	<b>45</b>
<b>Figure 3.32 :</b> Digital model of final bed topography for 24 cm staggered HACC (The dimensions on the figure are in mm and the dimensions on the legend are in cm). ....	<b>45</b>
<b>Figure 3.33 :</b> Digital model of final bed topography for 24 cm angled HACC (The dimensions on the figure are in mm and the dimensions on the legend are in cm). ....	<b>46</b>
<b>Figure 3.34 :</b> Longitudinal view of 24 cm HACC experiments for final bed topography (The dimensions are in mm).....	<b>46</b>
<b>Figure 3.35 :</b> Cross-section view of 24 cm HACC experiments for final bed topography (The dimensions are in mm).....	<b>46</b>
<b>Figure 3.36 :</b> The variation of packing density with respect to scour depth for different HACC cases .....	<b>49</b>
<b>Figure 3.37 :</b> The variation of packing density with respect to scour volume for different HACC cases .....	<b>49</b>
<b>Figure 3.38 :</b> The variation of packing density with respect to deposition length for different HACC cases .....	<b>50</b>
<b>Figure 3.39 :</b> The variation of dimensionless scour depth in terms of volume with respect to stem Reynolds number. ....	<b>50</b>
<b>Figure 3.40 :</b> The variation of dimensionless scour depth in terms of area with respect to stem Reynolds number. ....	<b>51</b>
<b>Figure A.1 :</b> (a) The change in the velocities and the scour depth over time for 9 cm solid cylinder experiment for 8 hours.(b) The change in the velocities and the scour depth over time for 9 cm solid cylinder experiment for 30 minutes.....	<b>61</b>
<b>Figure A.2 :</b> (a) The change in the velocities and the scour depth over time for 12 cm solid cylinder experiment for 8 hours.(b) The change in the velocities and the scour depth over time for 12 cm solid cylinder experiment for 30 minutes.....	<b>61</b>
<b>Figure A.3 :</b> (a) The change in the velocities and the scour depth over time for 16 cm solid cylinder experiment for 8 hours.(b) The change in the velocities and the scour depth over time for 16 cm solid cylinder experiment for 30 minutes.....	<b>62</b>



<b>Figure A.4 :</b> (a) The change in the velocities and the scour depth over time for 20 cm solid cylinder experiment for 8 hours.(b) The change in the velocities and the scour depth over time for 20 cm solid cylinder experiment for 30 minutes.....	<b>62</b>
<b>Figure A.5 :</b> (a) The change in the velocities and the scour depth over time for 12 cm regular HACC experiment for 8 hours.(b) The change in the velocities and the scour depth over time for 12 cm regular HACC experiment for 30 minutes.....	<b>63</b>
<b>Figure A.6 :</b> (a) The change in the velocities and the scour depth over time for 12 cm staggered HACC experiment for 8 hours.(b) The change in the velocities and the scour depth over time for 12 cm staggered HACC experiment for 30 minutes.....	<b>63</b>
<b>Figure A.7 :</b> (a) The change in the velocities and the scour depth over time for 12 cm angled HACC experiment for 8 hours.(b) The change in the velocities and the scour depth over time for 12 cm angled HACC experiment for 30 minutes.....	<b>64</b>
<b>Figure A.8 :</b> (a) The change in the velocities and the scour depth over time for 16 cm regular HACC experiment for 8 hours.(b) The change in the velocities and the scour depth over time for 16 cm regular HACC experiment for 30 minutes.....	<b>64</b>
<b>Figure A.9 :</b> (a) The change in the velocities and the scour depth over time for 16 cm staggered HACC experiment for 8 hours.(b) The change in the velocities and the scour depth over time for 16 cm staggered HACC experiment for 30 minutes.....	<b>65</b>
<b>Figure A.10 :</b> (a) The change in the velocities and the scour depth over time for 16 cm angled HACC experiment for 8 hours.(b) The change in the velocities and the scour depth over time for 16 cm angled HACC experiment for 30 minutes.....	<b>65</b>
<b>Figure A.11 :</b> (a) The change in the velocities and the scour depth over time for 20 cm regular HACC experiment for 8 hours.(b) The change in the velocities and the scour depth over time for 20 cm regular HACC experiment for 30 minutes.....	<b>66</b>
<b>Figure A.12 :</b> (a) The change in the velocities and the scour depth over time for 20 cm staggered HACC experiment for 8 hours.(b) The change in the velocities and the scour depth over time for 20 cm staggered HACC experiment for 30 minutes.....	<b>66</b>
<b>Figure A.13 :</b> (a) The change in the velocities and the scour depth over time for 20 cm angled HACC experiment for 8 hours.(b) The change in the velocities and the scour depth over time for 20 cm angled HACC experiment for 30 minutes.....	<b>67</b>
<b>Figure A.14 :</b> (a) The change in the velocities and the scour depth over time for 24 cm regular HACC experiment for 8 hours.(b) The change in the velocities and the scour depth over time for 24 cm regular HACC experiment for 30 minutes.....	<b>67</b>
<b>Figure A.15 :</b> (a) The change in the velocities and the scour depth over time for 24 cm staggered HACC experiment for 8 hours.(b) The change in the velocities and the scour depth over time for 24 cm staggered HACC experiment for 30 minutes.....	<b>68</b>
<b>Figure A.16 :</b> (a) The change in the velocities and the scour depth over time for 24 cm angled HACC experiment for 8 hours.(b) The change in the	

velocities and the scour depth over time for 24 cm angled HACC experiment for 30 minutes. ....	68
<b>Figure B.1</b> : Contourlines for the final bed topography for 9 cm solid cylinder experiment. ....	69
<b>Figure B.2</b> : Contourlines for the final bed topography for 12 cm solid cylinder experiment. ....	69
<b>Figure B.3</b> : Contourlines for the final bed topography for 16 cm solid cylinder experiment. ....	70
<b>Figure B.4</b> : Contourlines for the final bed topography for 20 cm solid cylinder experiment. ....	70
<b>Figure B.5</b> : Contourlines for the final bed topography for 12 cm regular HACC experiment. ....	71
<b>Figure B.6</b> : Contourlines for the final bed topography for 12 cm staggered HACC experiment. ....	71
<b>Figure B.7</b> : Contourlines for the final bed topography for 12 cm angled HACC experiment. ....	72
<b>Figure B.8</b> : Contourlines for the final bed topography for 16 cm regular HACC experiment. ....	72
<b>Figure B.9</b> : Contourlines for the final bed topography for 16 cm staggered HACC experiment. ....	73
<b>Figure B.10</b> : Contourlines for the final bed topography for 16 cm angled HACC experiment. ....	73
<b>Figure B.11</b> : Contourlines for the final bed topography for 20 cm regular HACC experiment. ....	74
<b>Figure B.12</b> : Contourlines for the final bed topography for 20 cm staggered HACC experiment. ....	74
<b>Figure B.13</b> : Contourlines for the final bed topography for 20 cm angled HACC experiment. ....	75
<b>Figure B.14</b> : Contourlines for the final bed topography for 24 cm regular HACC experiment. ....	75
<b>Figure B.15</b> : Contourlines for the final bed topography for 24 cm staggered HACC experiment. ....	76
<b>Figure B.16</b> : Contourlines for the final bed topography for 24 cm angled HACC experiment. ....	76



# **EXPERIMENTAL INVESTIGATION OF LOCAL SCOUR PATTERNS AROUND HEXAGONALLY ARRAYED CYLINDER GROUPS**

## **SUMMARY**

Bridges are functional infrastructures, which play a useful role in the design of cost-effective transportation routes. Design of a typical bridge requires the consideration of not only the structural but also the hydraulic and fluvial perspectives.

When a structure, in the present case a bridge pier, is placed in water, significant changes occur in the flow domain in its vicinity. The changes in the flow characteristics may lead to local and global scour on the river bed due to increased local shear stress.

In the past, the studies that investigated scour around vegetation elements showed that the increasing porosity of an obstruction reduces the scour depth at a considerable extent. Inspired by that, it was thought that designing a porous bridge pier might be a potential solution in terms of diminishing the scour depth and volume. Moreover, this solution diminish the contaction effect in a cross-section. Hence it has a potential to reduce the flooding risk at upstream of the bridge which originates from the presencse of pile. It is a known fact that as long as the cross sectional area of the bridge pier is kept constant, the bearing capacity of the pile would remain same. In the axis of this thought, in this study, different groups of cylinders (hexagonally arrayed circular cylinders), which have identical cross-sectional areas; however, different placement densities were considered as potential bridge piers and the scour patterns around the examined obstacles were investigated.

The primary aim of this thesis is to see how porosity and the placement configuration of the group of cylinders affect the scour depth and the scour pattern. So as to attain this aim, a set of experimental study was undertaken and the results are analysed in this perspective.

The experiments were performed in an open flume in Istanbul Technical University Hydraulics Laboratory. The flume has a horizontal bed of smooth concrete and the sidewalls are made of Plexiglas. It is 26 m in length, 0.98 m in width and 0.85 m in depth. In order to place a sand pit within the flume, a false bottom was built by using metal sheets. The height of the false bottom is 20 cm and the length is 14.5 m. A 3.5 m long sand pit was placed in the false bottom.

In order to understand the scour mechanism in uniform flow conditions, 16 sets of experiments were conducted. These 16 sets comprise four solid cylinder experiments, with diameter of 9 cm, 12 cm, 16 cm and 20 cm, and twelve experiments with an array of circular cylinders. This array consists of seven small cylinders of 3.4 cm diameter, and was placed in different geometries to examine the effect of porosity and orientation to the flow.

For each experiment, first the pile model was placed and fixed in the middle of the flume, 11 m downstream of the flume inlet. Then, the sand bottom was smoothed out by using traditional trowel. In order not to disturb the sand bottom, the flume was

filled very slowly so it took 3 to 4 hours. The Vectrino II Profiler was placed 5,3 cm away from the obstacle surface and 8.5 cm above from the initial sand bed for each experiment. Right after Vectrino II Profiler was started, the pumps were started, as well. Each experiment took 8 hours. The flow discharge per unit width was set to  $q = 88 \text{ l/s/m}$  and the flow depth to  $h = 31 \text{ cm}$ .

After each experiment, when the flow entirely stopped, by using the discharge valve, the water in the flume was drained slowly. When the bed surface was completely dry, the laser scanner was used in order to obtain the three dimensional elevation of the final condition of the sand bed. For each experiment, the data from the Vectrino II Profiler and laser scanner were used in order to compare the results of the experiments. The aim was to see the differences between the porous configurations and the 9 cm solid cylinder, which has the same cross-sectional area with the HACCs (Hexagonally Arrayed Circular Cylinders). The experimental results showed the porosity causes a reduction of scour depth indeed and reveal the potential of the applicability of the HACCs as bridge pier.



## **ALTİGEN DİZİLİMLİ SİLİNDİR GRUPLARI ETRAFINDAKİ YERSEL OYULMA DESENLERİNİN DENEYSEL OLARAK ARAŞTIRILMASI**

### **ÖZET**

Köprüler, düşük maliyetli ve kullanışlı ulaşım ağları oluşturmaya yardımcı olan önemli üst yapı elemanlarıdır. Bu nedenle tarihin başlangıcından beri insan yaşamına ve uygarlıkların gelişimine önemli katkıları vardır. Köprü tasarımı yapılırken sadece yapısal özellikler değil, hidrolik etkiler de göz önünde bulundurulmalıdır. Köprü inşası da diğer mühendislik yapılarının inşası gibi doğada çeşitli değişikliklere sebep olur. Mühendisler bir yapı inşa ederken bu değişiklikleri ve bu değişikliklerin olası sonuçlarını göz önünde bulundurmak ve gerekli önlemleri almak zorundadırlar. Köprü ayakları akarsular içine yerleştirildiklerinde akım özelliklerinde çeşitli değişiklikler yaratırlar. Bu değişikliklerden bazıları köprü ayağı çevresinde türbülans ve buna bağlı olarak sediment taşınımı kapasitesinin artmasıdır. Böylece köprü ayağı çevresinde sediment oyulması meydana gelir. Bu oyulma köprü ayağının stabilitesini bozabilir ve akarsu tabanında köprünün yıkılmasıyla sonuçlanabilecek değişiklikler yaratabilir. Bu oyulmanın miktarının ve kapsamının belirlenmesi ve kabul edilebilir sınırlar içinde tutulması mühendisler için oldukça önemli bir konudur.

Daha önce bitkilerle yapılan deneysel çalışmalarda, engel porozitesinin oyulmayı önemli ölçüde düşürdüğü belirlenmiştir. Bu gözlemden yola çıkarak ve bitkilerden ilham alınarak köprü ayaklarının poroz şekilde inşasının mümkün olup olmadığının araştırılması bu çalışmanın temel konusunu oluşturmaktadır. Köprünün taşıyıcılığını belirleyen köprü ayağı kesit alanı sabit tutuldukça köprünün düşey yüke karşı dayanımının da sabit kalacağı bilinen bir gerçektir. Bu bilgiden yola çıkılarak kesit alanı aynı ancak boşluk yoğunluğu farklı potansiyel köprü ayağı modellerinin oluşturduğu yersel oyulmalar deneysel olarak incelenmiştir. Bu çalışmanın temel amacı boşlukluluğun ve modellerin akıma göre açısının oyulma derinliği ve oyulma desenine etkisini incelemektir. Çalışma kapsamında bu amaca uygun görülen bir dizi deney yapılmıştır. Deneyler, İstanbul Teknik Üniversitesi Hidrolik Laboratuvarında yer alan akım kanalında yapılmıştır. Akım kanalının tabanı beton, yan yüzeyleri pleksiglastan yapılmıştır. Uzunluğu 26 m ve genişliği 0.98 m olan kanalın yüksekliği ise 0.85 m'dir. Kanal içine bir kum havuzu yerleştirilebilmesi için metal saclar kullanılarak bir yapay taban oluşturulmuştur. Bu yapay tabanın yüksekliği 20 cm ve uzunluğu 14,5 m'dir. Yapay tabanın içine yerleştirilen kum havuzu ise 3,5 m uzunluğundadır.

Uniform akım koşullarında oyulma mekanizmasını anlamak üzere on altı set deney tasarlanmıştır. Bu on altı setin dördü tek silindir şeklindeyken diğerleri çevresel çapı 12, 16, 20 ve 24 cm olmak üzere altıgen dizilimli ve 3,4 cm çaplı yedi adet küçük silindirden oluşmaktadır. Küçük silindirlerden oluşan altıgen yapıları modellerde farklı çevresel çapın yanında farklı akım geliş açıları da denenmiştir.

Her deneyden önce, model kanalın ortasına, kanal başlangıcından 11 m uzağa yerleştirilip sabitlenmiştir. Sonrasında kum havuzunun yüzeyi düzeltilerek kanal deneye hazır hale getirilmiştir. Su doldurulurken oyulma oluşmaması için kanal

yavaşça doldurulmuştur. Hız ölçümlerini almak üzere modelden 5,3 cm uzağa ve tabandan 8,5 cm yukarı Vectrino II Profiler hızölçer yerleştirilmiştir. Vectrino II Profiler çalıştırıldıktan hemen sonra pompalar devreye sokularak kanalda akım başlatılmıştır. Kanalda akım oluşturmak için 25 kW gücünde bir ana pompa ve kanalın sonundan başına su sirkülasyonunu sağlayarak debiyi arttıran iki adet iç pompa kullanılmıştır. Debi kontrolünün sağlanması için kanalın bozulmamış akım kısmında Vectrino I akım hızölçer ile hız kontrolü ve aynı yerde su seviyesi kontrolü her deney için yapılmıştır. Tüm deneyler 8 saat sürmüştür. Birim genişlik debisi  $q = 88 \text{ l/s/m}$  olarak ayarlanmış ve akım derinliği  $h = 31 \text{ cm}$  tutulmuştur.

Her deneyin bitiminde, akım tamamen durdurulduktan sonra kanalın tahliye vanası açılmış ve fazladan oyulmaya sebep olmamak adına kanal yavaşça boşaltılmıştır. Kum yüzeyi tamamen kuruduktan sonra taban deseninin üç boyutlu modelinin çıkarılması için Leica Scanstation C10 Lazer Tarayıcı ile tarama yapılmıştır. Her deney için bu taramadan alınan sonuçlarla hızölçer Vectrino II Profiler'dan alınan sonuçlar incelenmiştir. Bu incelemede asıl amaç altıgen geometrideki poroz modellerin aynı kesit alanına sahip 9 cm'lik tekil silindirle oyulma açısından karşılaştırılmasıdır.

Her deneyden sonra model çevresinde bir oyulma konisi ve mansap bölgesinde bir oyulma bölgesi meydana gelmiştir. Vectrino II Profiler ile 8 saat boyunca modelin 5,4 cm önünde alınan taban uzaklığı ölçümleri, bu noktada tüm poroz silindir gruplarının 9 cm çaplı tekil silindirden daha az oyulmaya yol açtığını ortaya koymuştur. Aynı zamanda poroz silindir gruplarını çevreleyen çemberin çapıyla aynı çapa sahip tekil silindirlerin de her çap için poroz silindir gruplarından daha fazla oyulmaya yol açtığı görülmüştür.

Vectrino II Profiler ile yine model önünde alınan hız ölçümlerine göre akım yönündeki hızın oyulma derinliğinin artmasıyla arttığı, yanal hızın belirgin bir değişim göstermediği ve düşey hızın da zamanla arttığı gözlemlenmiştir. Hızlardaki değişimin çoğunlukla ilk 10 dakika içinde görüldüğü belirlenmiştir.

Poroz silindir grupları ile yapılan deneylerin 9 cm tekil silindir ile karşılaştırılması için lazer tarayıcıdan alınan sonuçlarla yapılan çalışmada en fazla verimliliğin %26 ile 20 cm düz dizilimli silindir grubuna ait olduğu belirlenmiştir. Aynı çalışma 9 cm tekil silindirden daha fazla oyulmaya yol açan tek poroz silindir grubunun %2 ile 16 cm açılı dizilim olduğunu ortaya koymuştur.

Deneylerden sonra lazer tarayıcı ile taranan ve üç boyutlu modelleri hazırlanan kum yüzeylerinin incelenmesi sonucunda tekil silindirlerin birikme bölgelerinde iyi gelişmiş ripple bölgelerinin olduğu ancak silindir arkasında birikmenin sırt şeklinde olmadığı gözlemlenmiştir. 12 cm çevreleyen çaplı poroz silindir gruplarının da tekil bir silindir gibi davrandığı ve benzer oyulma deseni oluşturduğu görülmüştür. 16 cm çevreleyen çaplı silindir gruplarında ise açı fark etmeksizin, birikme bölgesinde bir sırt oluşumu ve sırtın mansabında da ripple oluşumu gözlemlenmiştir. 16 cm çevreleyen çaplı silindir grubu ile aynı oluşumların 20 cm çaplı grupta da olduğu ancak farklı olarak burada sırt üzerinde de ripple oluşumu varlığı belirlenmiştir. 24 cm çevreleyen çaplı poroz silindir gruplarında ise yerel ve global oyulma ayrı ayrı görülebilmektedir. Sırt ve ripple oluşumu ise 20 cm çaplı grupla benzer olarak nitelendirilmiştir. Tüm deneylerde oyulma konisinin memba tarafındaki eğiminin mansap tarafındaki eğiminden daha dik olduğu gözlemlenmiştir.

Morfometrik analiz yapılabilmesi için poroz silindir gruplarında sızdırmazlık sıklığı parametresi tanımlanmış ve bu parametre ile oyulma derinliğinin ilişkisi



incelenmiştir. Çevreleyen çapı 24 cm, 20 cm ve 16 cm olan poroz silindir gruplarında sızdırmazlık sıklığı arttıkça, yani çevreleyen çap küçüldükçe oyulma derinliğinin arttığı gözlemlenmiştir. 12 cm ile 16 cm çevreleyen çap arasında, sızdırmazlık sıklığı parametresi 0,4 mertebesindeyken bu düzenin değiştiği gözlemlenmiştir.

Tüm poroz silindir grupları deneylerinde birikme bölgesinin en yüksek kotunun silindir merkezine uzaklığı artan sızdırmazlık sıklığıyla artış göstermiştir. Aynı çevreleyen çapta tüm çaplar için en kısa uzaklığı düz sızilimli grup vermiştir.

Tekil silindir deneylerinin sonuçlarına göre çap arttıkça oyulma derinliği oyulma hacmine ve oyulma alanına göre daha fazla artış göstermiştir.

Sonuçlar, porozitenin oyulmayı azalttığını doğrular nitelikte olup HACC'lerin (Altıgen Dizilimli Silindir Grubu) pratikte uygulanabilirlik potansiyelini ortaya çıkarmıştır.



## **1. INTRODUCTION**

Bridges are functional infrastructures, which play a useful role in the design of cost-effective transportation routes. Design of a typical bridge requires the consideration of not only the structural but also the hydraulic and fluvial perspectives. Bridges have been used to connect two sides of a water body since the beginning of history and in this way they provide vital benefit to human societies so far. However, it is not possible to build a bridge without influencing the surrounding fluvial and riparian environment. Engineers have to consider the potential changes that may occur during the lifetime of the structures and they should take some effective precautions against the potential problems.

When a structure, specifically a bridge pier, is placed in water, significant changes occur in the flow domain in its vicinity. The change in the flow characteristics may cause local and global scour on the river bed due to increased local shear stress.

Scour around bridge piers is an important topic of hydraulic engineering since one of the top reasons of bridge failures is the instability caused by scour. For instance, in the United States of America, in the last thirty years, 60% of the 1500 destroyed bridges, which were crossing rivers, have been destroyed due to local scour (Nohani et al., 2015). Therefore, estimation of the scour depth around bridge piers with an acceptable accuracy is a key issue for civil engineers. In order to estimate the expected scour depth and maintain it to an acceptable level with the utilization of some structural precautions, engineers have put a significant effort in the past. In this perspective the objective of the study is as described below.

### **1.1 Aim of the Study**

In the past, studies investigating scour around vegetation elements showed that when the porosity of an obstruction increases, then the scour depth could be decreased to a considerable extent. More specifically, with the increasing permeability, the magnitude of the bleed flow (flow penetrating through the obstacle) increases, the

horse-shoe vortex decreases and the separation distance at the upstream decreases, and consequently the frontal scour depth decreases. (Yagci et al., 2015) Inspired by that, it was thought that designing a porous bridge pier might be a potential solution in terms of diminishing the scour depth. It was thought that in this way scour volume and depth can be reduced to a certain extent. Moreover, porosity can help to reduce the risk of flooding due to blockage of flow from the bridge piers. It is a known fact that as long as the cross sectional area of the bridge pier is kept constant (this cross-section determines the loading capacity of the pile), the bearing capacity of the pier would remain same. In the axis of this thought, in this study, different groups of cylinders (hexagonally arrayed circular cylinders), which have same cross-sectional area but different placement densities were considered as a potential bridge pier and the scour patterns around the examined obstacles were investigated. Possible advantages of a porous bridge pier are explained below:

1. Due to the porous form of the model, local shear stress around the pier would be decreased and correspondingly the local scour would be decreased.
2. Porosity allows water to pass through the pier. Therefore a porous pier would block less the river flow and the back water at the upstream of the bridge would be diminished.
3. Different from the other countermeasures against bridge pier scour in the literature, a hexagonally arrayed seven cylinder group, which has the same cross sectional area with a solid cylinder, can be more practical in terms of application since seven small cylinders are easier to penetrate the river bed compared to single counterpart.
4. There would be no need to use another countermeasure to decrease the scour if a porous pier is used. This leads to decrease in costs.

The primary aim of this thesis is to see how porosity and the placement configuration of the group of cylinders affect the scour depth and the scour pattern. So as to attain this aim, a set of experimental studies was undertaken and the results are analysed in this perspective.

## 1.2 Fundamental Background

### 1.2.1 Flow around a cylinder body

The flow is expected to significantly change when a single circular pile is placed on a river bed. There will be a horse-shoe vortex formation in front of the pile. Secondly, a vortex flow pattern will be formed at the lee side of the cylinder (Figure 1.1). Then, the streamlines will change depending on the shape of the pile at the sides. Additionally, a down flow will occur in front of the pile as a result of flow deceleration. When all these effects get combined, the local sediment transport capacity around the pile increases (Sumer and Fredsøe, 2002).

The reason of the formation of horse-shoe vortex is the rotation in the incoming flow. The pile creates an adverse pressure gradient on the upstream of the structure and leads to a three dimensional separation of the flow boundary layer. After the separation, the boundary layer rolls up and creates a spiral formed vortex around the structure which is called a horse-shoe vortex (Sumer and Fredsøe, 2002).

According to Sumer and Fredsøe (2002), “Two ingredients necessary for the generation of horse-shoe vortex are: (1) An incoming boundary layer must exist, (2) The adverse pressure gradient induced by the pile must be sufficiently strong so that the boundary layer on the bed can separate to generate the horse-shoe vortex. (p.152)

The reason of the formation of lee-wake vortices is the rotation in the boundary layer over the surface of the structure. At the side edges of the pile, shear layers spread and they roll up and create the vortices on the lee-wake of the structure (Sumer and Fredsøe, 2002).

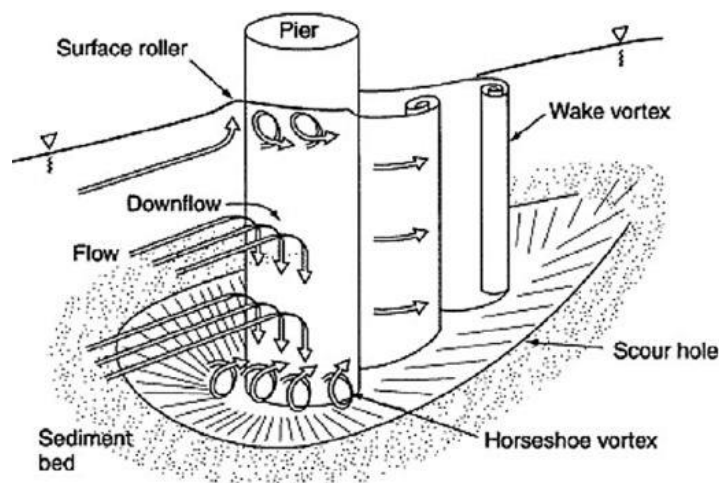


**Figure 1.1 :** Flow pattern around the bridge pier (Nohani et al., 2015).

### **1.2.2 Scour around a cylindrical body**

According to the definition, which is given by Hamill (1999), “Scour can be defined simply as the excavation and removal of material from the bed and banks of streams as a result of the erosive action of flowing water.” (p. 251) Around a bridge structure, there are three types of separate processes, which can change the bed elevation. These are general scour, localised scour and local scour. General scour can occur even without the presence of a bridge. It can be defined as aggradation or degradation of the bed level. It can be either temporary or a trend. Localised scour, in other words constriction scour, is caused by the increase of the erosive power of the flow due to the presence of the bridge. The bridge piers and abutments make the channel narrower. Therefore, the flow becomes faster and more erosive. Local scour is the type of scour directly affected by the bridge pier itself, which interferes with the flow of water (Chiew, 1984). The horse-shoe vortex process can erode a big amount of sediment around a pile when combined with the effect of the streamline contraction at the side edges (Sumer and Fredsøe, 2002).

### **1.2.3 Scour depth**

Scour depth is the main unknown variable, which needs to be estimated in order to prevent the bridges from destruction. If the depth of the scour hole is more than a certain level, the stability of the bridge pier can be in danger.

The factors, which affect the scour depth, are like the following (Sumer and Fredsøe, 2002):

- Shields parameter
- the sediment gradation,
- the boundary layer depth to pile size ratio,
- the sediment size to pile size ratio,
- the shape factor,
- the alignment factor

In the following subsections, the influences of these factors are discussed separately.

### 1.2.3.1 Shields parameter

Critical Shields parameter ( $\theta_c$ ) can be defined as:

$$\theta_c = \frac{U_{fc}^2}{(s-1)gd} \quad (1.1)$$

where  $U_{fc}$  is the critical friction velocity,  $s$  is the relative density of the sediment,  $d$  is the grain diameter, and  $g$  is the acceleration of gravity. If  $\theta$  is greater than the critical value, sediment is mobilized. The critical value is due to Shields' experiments and can be obtained related to Reynolds number for the grain. Grain Reynolds number can be defined as:

$$Re = \frac{U_f d}{\nu} \quad (1.2)$$

where  $U_f$  is the skin friction velocity,  $d$  is the grain diameter and  $\nu$  is the kinematic viscosity of the fluid (Fredsøe and Deigaard, 1992) (Figure 1.2).

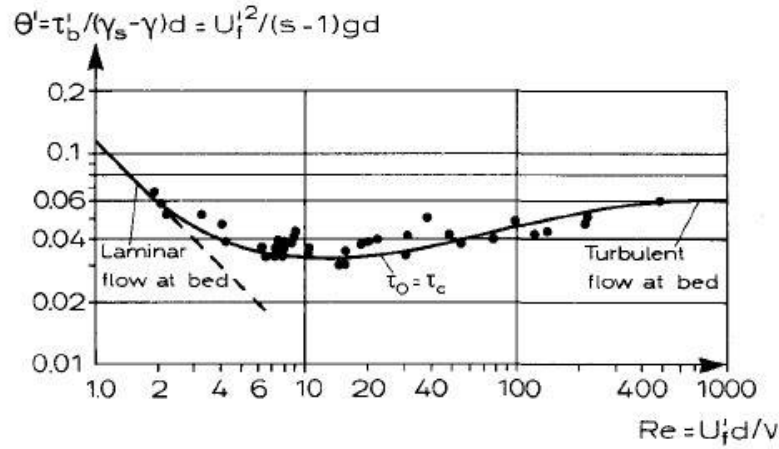


**Figure 1.2 :** The Shields diagram giving the threshold value  $\theta_c$  as a function of  $Re$  (Fredsøe and Deigaard, 1992; p.203).

If  $\theta$  is smaller than the critical value no sediment motion takes places at the bed, far from the structure. This is called clear-water condition. For the clear water scour, the scour depth increases with increasing  $\theta$ . Moreover, when  $\theta$  is very small, no scour will occur even near the structure. The reason for this is that even the amplified local bed shear stress may not be enough adequate to initiate sediment motion (Sumer and Fredsøe, 2002).

If  $\theta$  is greater than the critical value, sediment motion is seen even far from the structure and this situation is called live-bed. For the live-bed scour, the scour depth increases with increasing  $\theta$  and reaches a maximum, then, slightly decreases (Figure 1.3). The reason is the backfill by the sediment flow from the upstream (Sumer and Fredsøe, 2002).

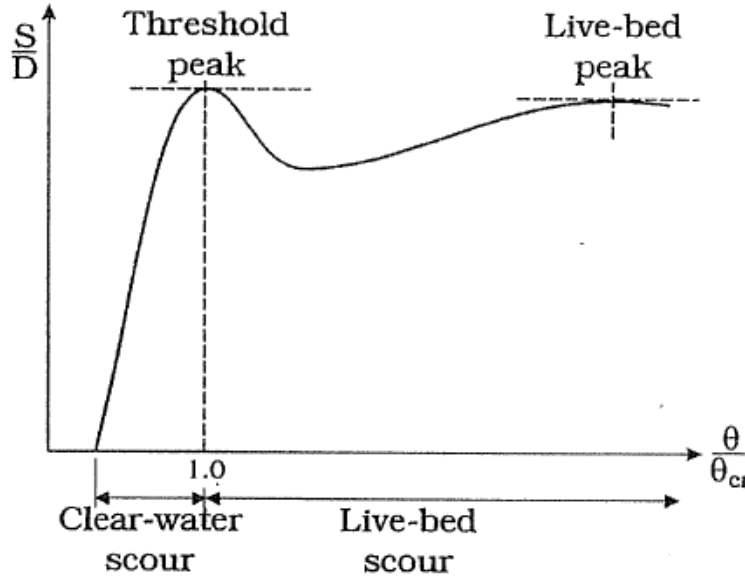


**Figure 1.3 :** Scour depth against Shields parameter for uniform sediment. (Melville and Coleman, 2000; Sumer and Fredsøe, 2002, p.178).

### 1.2.3.2 Sediment gradation

The geometric standard deviation of the sediment can be defined as below:

$$\sigma_g = \frac{d_{84}}{d_{16}} \quad (1.3)$$

where  $d_{84}$  represents the grain diameter which the 84% by weight of the sediment grains are finer than and  $d_{16}$  represents the grain diameter which the 16% by weight of the sediment grains are finer. Ettema (1976) showed that the scour depth is reduced tremendously as  $\sigma_g$  increases for clear water condition. In live-bed condition, Baker (1986) showed this change is not that significant.

### 1.2.3.3 Boundary layer depth to pile size ratio

If the boundary layer thickness ( $\delta$ ) to pile size ( $D$ ) ratio increases, the scour depth increases, as well. This is because of the effect of boundary layer to pile size ratio on



the horse-shoe vortex size which increases with the increasing  $\delta/D$  ratio (Sumer and Fredsøe, 2002).

#### 1.2.3.4 Sediment size to pile size ratio

Figure 1.4 shows the data compiled by Melville and Sutherland (1988). According to this, if the sediment size is large relatively to the pile diameter, the scour depth is limited. It is also seen from the figure that if  $D/d_{50}$  is greater than 50, the effect of the sediment size disappears (Sumer and Fredsøe, 2002).

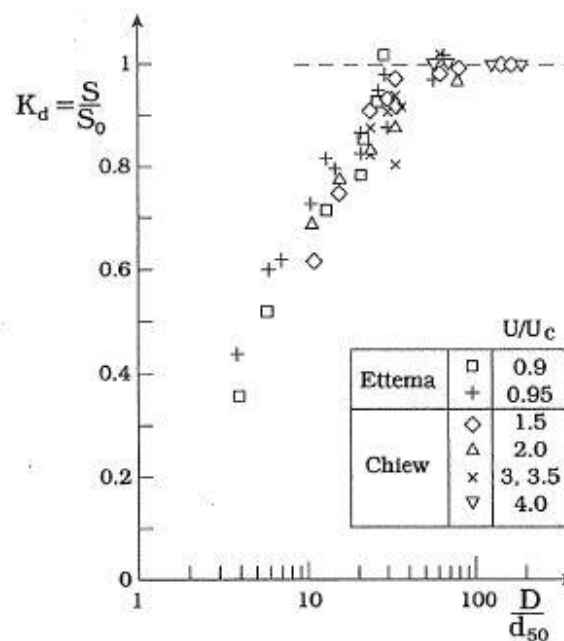


**Figure 1.4 :** Effect of sediment size. Data compiled by (Melville and Sutherland, 1988; Sumer and Fredsøe, 2002, p.180).

#### 1.2.3.5 The shape factor

Another important factor that affects scour depth is the cross-sectional shape of the pile. The shape affects the size of the horseshoe vortex and the size of horseshoe vortex affects the scour depth. The larger the horseshoe vortex, the larger the scour depth. The shape of the pile also affects the plan view extend of the separation zone. As a characteristic of the shape, pile height is also important. Smaller pile height causes weaker horseshoe vortex and therefore smaller scour depth.

#### 1.2.3.6 The alingment factor

As can be seen in Figure 1.5, the approach angle of the flow for cross-sectional shapes may be more significant than the circular one. It can be said that when the

angle of the attack gets larger, the scour depth gets deeper due to the increasing in adverse pressure gradient and larger horseshoe vortex.

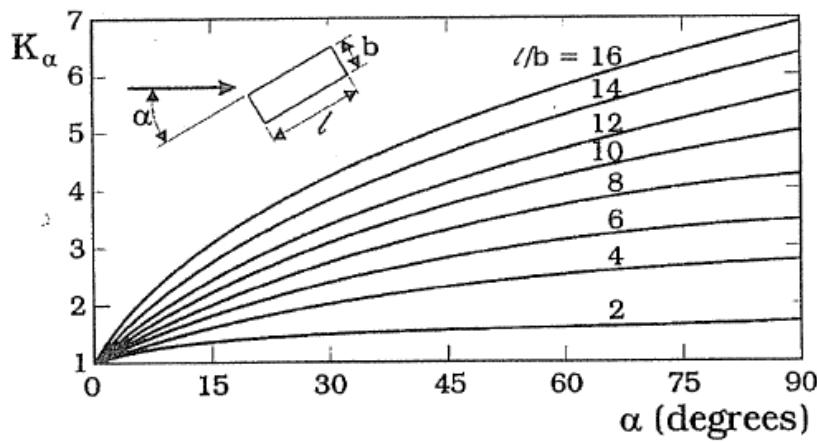


**Figure 1.5 :** Effect of alignment. (Laursen, 1958; Sumer and Fredsøe, 2002, p.183).

### 1.3 Literature Review

Being the top reason of bridge failures, scour around piers is an important topic of scientific researches. To understand the dynamics of the scour and the effects that determine the scour depth, several experimental studies were conducted over the years. Since scour is a complicated and a partly random process, it is hard to determine the full concept. Despite the fact that scour process is not completely solved yet, and countermeasures are necessary to protect the bridge piers.

If the countermeasures against bridge scour are categorised broadly, there are two categories of flow-altering and bed-armouring countermeasures. In flow-altering countermeasures, the idea is to decrease the strength of the effects that causes scour such as the down flow and the horseshoe vortex. In the bed-armouring countermeasures, the change is on the bed instead of the flow. By providing a physical barrier such as riprap, gibbons, cable-tied blocks, the bed around the pier is protected from scour (Tafarojnoruz et al., 2012).

#### 1.3.1 Flow-altering countermeasures against scour around bridge piers

As explained above, flow-altering countermeasures aim to mitigate the scouring effects of down flow and horseshoe vortex.

In the study carried by Tafarojnoruz et al. (2012) six different types of flow-altering countermeasures were investigated experimentally in order to see the differences on the scour depths. These six types of countermeasures were submerged vanes, bed sill,

transverse sacrificial piles, collar, threading, and pier slot, which can be seen in Figure 1.6.

In this study, using the data from pertinent literature, the best configurations for each countermeasure were tested. The tests showed that the scour reduction was not highly efficient for any of the countermeasures. According to this, it can be said that a single flow-altering countermeasure may not be adequate for scour protection. This study also showed that the high performance of some of the countermeasures from these tests depends on the experimental conditions.

The specific results of this study for each countermeasure are listed below:

- Since the reduction of scour depths for downstream bed sill, double submerged vanes, and threading are less than 20%, proper combinations of these countermeasures can be more efficient.
- Transverse sacrificial piles lead to deep scour in front of them and this may cause application problems for practical purposes.

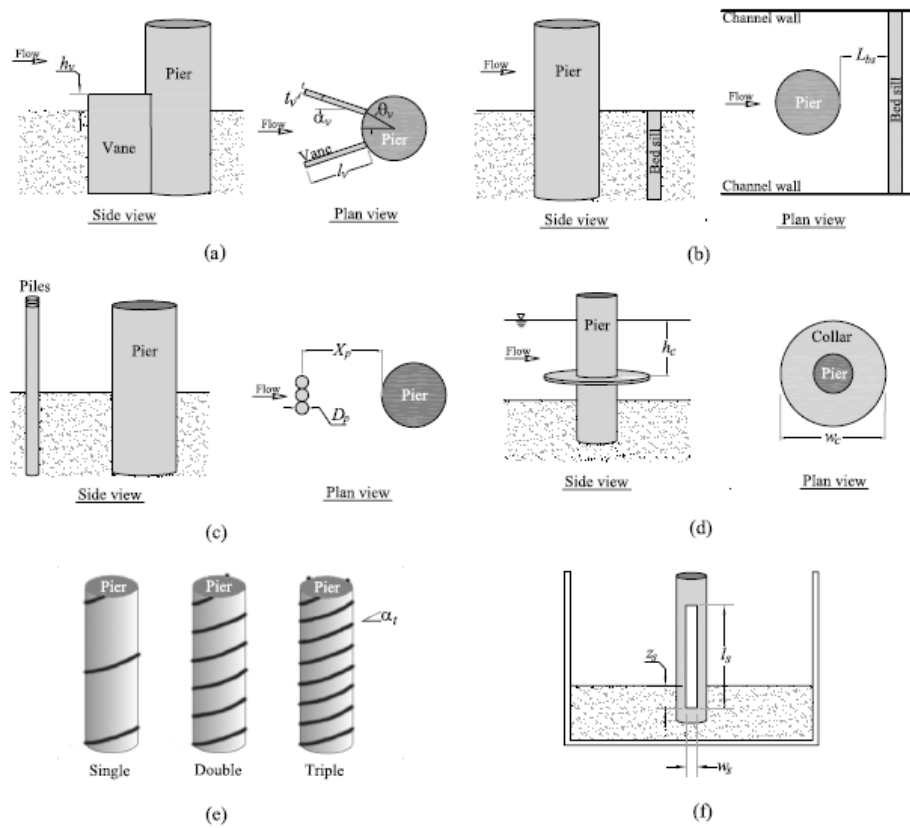


**Figure 1.6 :** Flow-altering countermeasures: (a) submerged vanes; (b) bed sill; (c) sacrificial piles; (d) collar; (e) threading; (f) pier slot (Tafarojnoruz et al., 2012).

### 1.3.2 Flow and scour around porous structures and pile groups

In the study by Vittal et al. (1994) three smaller piers, termed as a full pier group, were used instead of one solid pier in order to reduce scour depth. A partial pier group and a full pier group with a collar were also investigated (Figure 1.7). The angle between the piers in the configurations was  $120^\circ$ . The examined angles of attack of the approaching flow were  $0^\circ$ ,  $15^\circ$ ,  $30^\circ$ ,  $45^\circ$  and  $60^\circ$ , as can be seen in Figure 1.8. For each configuration, four different types of sediment with different geometric mean sizes were used. The geometric mean sizes were 0.775 mm, 1.183 mm, 1.543 mm and 1.844 mm. The diameter of the solid cylinders was 11.25 cm and the diameters of the smaller cylinders were 3.40 cm. Comparing pier group with a solid cylindrical pier whose diameter is equal to the circumscribing circle diameter of the circle group has a scour reduction of about 40% (Vittal et. al., 1994).

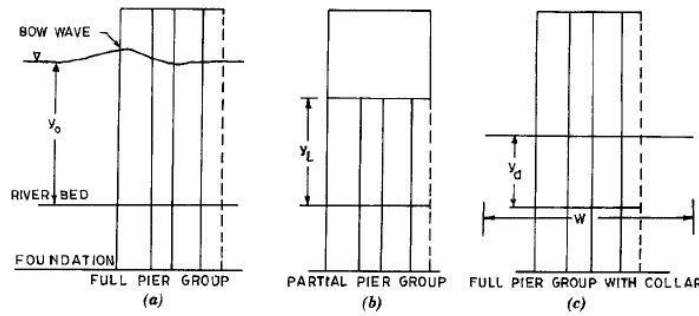


**Figure 1.7 :** Pier groups: (a) Full; (b) Partial; and (c) Full with Collar (Vittal et al, 1994)

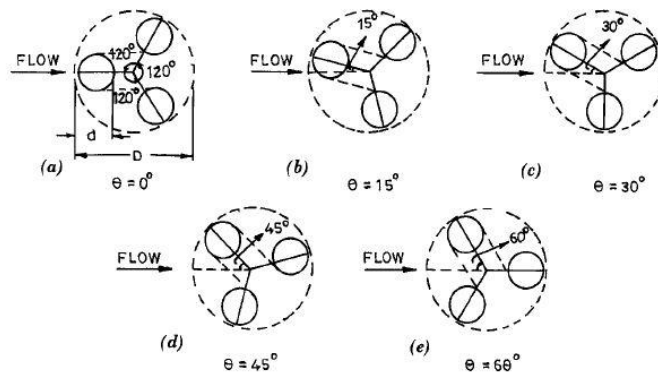


**Figure 1.8 :** Approach Flows: (a)  $0^\circ$ ; (b)  $15^\circ$ ; (c)  $30^\circ$ ; (d)  $45^\circ$ ; and (e)  $60^\circ$  (Vittal et al, 1994)

Sumer et al. (2005) present the results of a set of experiments that investigate scour around pile groups in steady current in order to distinguish global scour from local scour. The experiments included two types of configurations, one in rigid bed and the other in the sand bottom. The configurations and flow conditions can be seen in

Figure 1.9 and Figure 1.10, respectively. According to the study, when a group of piles is exposed to water flow, two kinds of scour pattern occur. One of them is local scour, which is the one around the individual piles. The other is global scour, which is around the pile group. If the piles in the pile group are adequately apart from each other, these two types of scour can be seen separately. If they are not, these two kinds of scour are merged into one big scour hole.

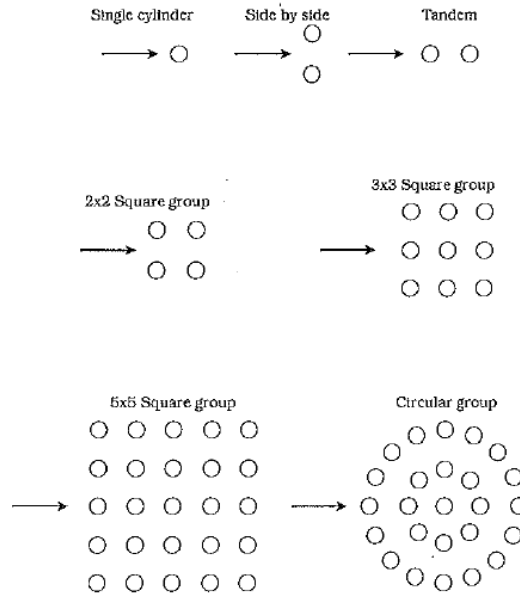


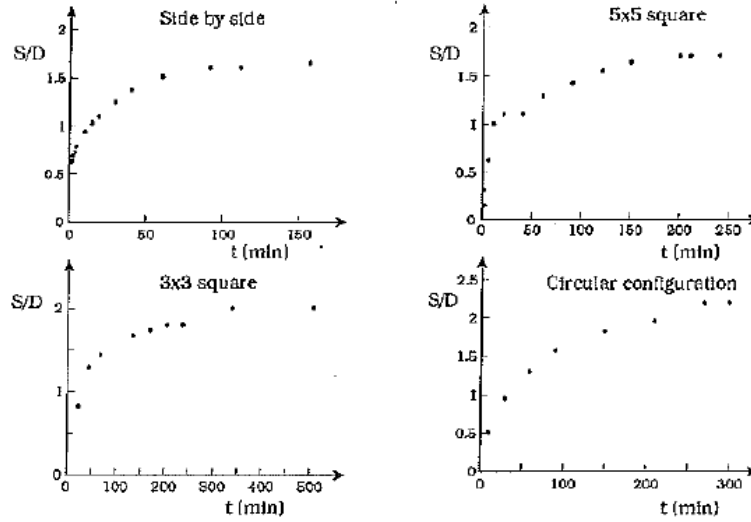
**Figure 1.9 :** Pile-group configurations used in the study of Sumer et al. (2005).

Pile Group	Gap ratio $G/D$	$U$ (m/s)	$U_f$ (cm/s)	$Re_f$	$Re$	$\theta$
side by side	4	0.33	1.5	67	$1 \times 10^4$	0.07
$2 \times 2$ square group	4	0.34	1.5	68	$1 \times 10^4$	0.07
$3 \times 3$ square group	4	0.31	1.4	62	$1 \times 10^4$	0.06
$5 \times 5$ square group	4	0.31	1.4	63	$1 \times 10^4$	0.06
circular group	4	0.30	1.3	59	$1 \times 10^4$	0.055

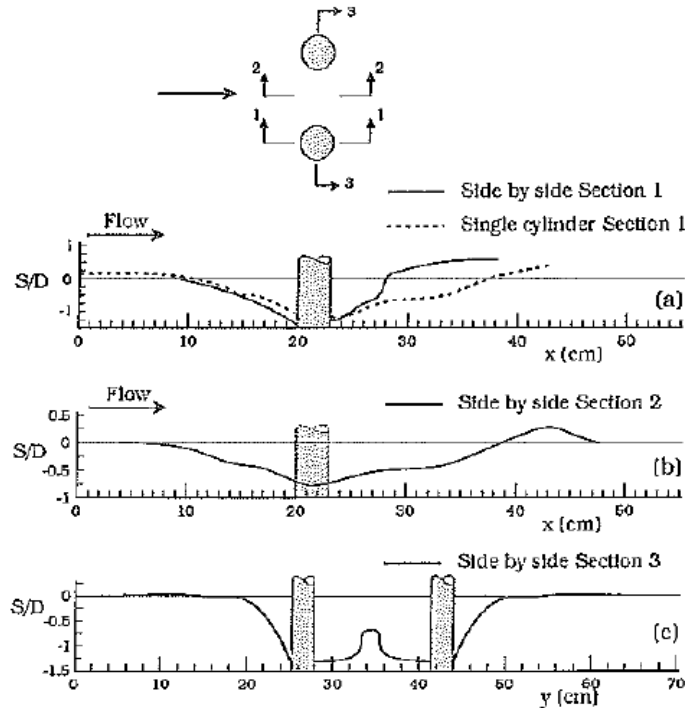
**Figure 1.10 :** Test conditions for scour experiments. Water depth=0.25 m. Circular group with same pile density as in  $5 \times 5$  group. (Sumer et al., 2005)

Figure 1.11 shows the time development of the scour depth for a four pile group. The profiles of the equilibrium scour depths are depicted in Figure 1.12, which also shows the longitudinal scour profile of a single cylinder as dashed line for comparison purposes. In the light of this study, it can be said that the horseshoe vortex, vortex shedding, contraction of streamlines and down flow are the ruling mechanisms for the local scour. Increase of the main velocity and the turbulence generated by the

upstream piles are the main mechanisms responsible for global scour. When the number of piles increases, the global scour depth increases to a certain level. After that, it remains the same.



**Figure 1.11 :** Time development of scour, live bed,  $G/D=4$  (Sumer et al., 2005).



**Figure 1.12 :** Equilibrium scour profiles for 2-pile, side-by-side arrangement pile group, live bed,  $G/D=4$  (Sumer et al., 2005).

In Ataie-Ashtiani and Beheshti (2006), local scour around pile groups exposed in steady flow and clear-water conditions was investigated experimentally. In the experiments, two different sizes of sand were used as the geometric standard

deviations are 1.54 and 1.13 and the mean grain sizes are 0.25 and 0.98 mm. In Figure 1.13 the configurations can be seen.

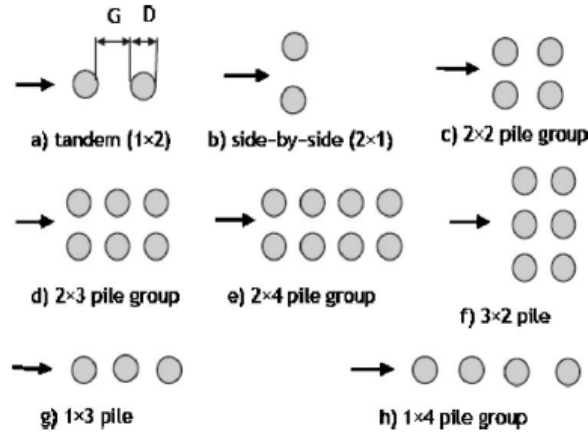


**Figure 1.13 :** Pile groups used in experiments (Ataie-Ashtiani and Beheshti, 2006)

The diameters of the piles in the models are 16, 22 and 28 mm. The pile spacing,  $G$ , varied from zero to six times of the pile diameter. In Figure 1.14(a), the equilibrium maximum scour depth at two pile groups normalized by the scour depth at a single pile,  $S/S_s$ , versus the normalized pile spacing,  $G/D$ , for the tandem arrangement can be seen. It shows that the maximum scour depth increases when the ratio  $G/D$  increases. Scour depth reaches its maximum value at  $G/D=2$ , then it decreases into its single-pile value. In Figure 1.14(b), data collected in this study and data from Hannah (1978) in the case of the side-by-side arrangement can be seen together. The maximum scour depth is nearly 50% more than the single-pile value at  $G/D=0.25$ . The reason for that is expressed as ‘‘the increased size of the horseshoe vortex for such small pile spacing, and partly to the very strong gap flow between the two neighbouring piles. When  $G/D=0.25$ , the two piles act as a single pile.’’ (Ataie-Ashtiani and Beheshti, 2006, p.1101).

This study shows that the difference between scour at a pile group and around a single pile depends on the pile spacing. For very small pile spacing such as  $G/D \leq 0.15$ , the pile group acts like a single pile. According to the pile-group arrangement, the interference effect diminishes for pile spacing of  $G/D > 2-4$ .

In Takemura and Tanaka (2007), the characteristics of flow structures around a colony-type emergent roughness model and the drag coefficient ( $C_{cd}$ ) for the model were investigated. The colony model was fixed on a plate and the flow was uniform. The investigation made by flow visualization, spectral analysis, velocity measurement and drag force measurement. In this study, seven cylinders were

mounted on a water flume with equal spacing in grid or staggered orientation. The mean flow velocity was 0.04, 0.1 and 0.4 m/s for  $L/D=0.25, 0.5, 1, 2, 3$  and 5. The colony model and the velocity measurement points can be seen in Figure 1.15. Visualized flow pattern around the colony model can be seen in Figure 1.16.

As it is seen in Figure 1.17, three types of vortices were generated behind the colony model depending on  $L/D$ . In grid arrangement (Figure 1.17(a-d)), small vortices (SV) are formed along the shear layer followed by large scale Karman vortex street (LKV) for  $L/D=0.5$ . For  $L/D=1$ , SV do not form. For  $L/D=3$ , LKV cannot be seen even though a primitive Karman street is generated. In the staggered arrangement (Figure 1.17e-f), for  $L/D=0.5$ , LKV can be seen clearly similarly to grid arrangement. Nonetheless, a primitive Karman street is not clear for  $L/D=3$ .

The experimental study of Zong and Nepf (2011) describes the turbulent structures behind a two dimensional porous obstruction. The experimental setup can be seen in Figure 1.18 with emergent circular cylinders with diameter  $d=0.6$  cm being set in a staggered arrangement. The longitudinal profiles of velocity patches can be seen in Figure 1.19.

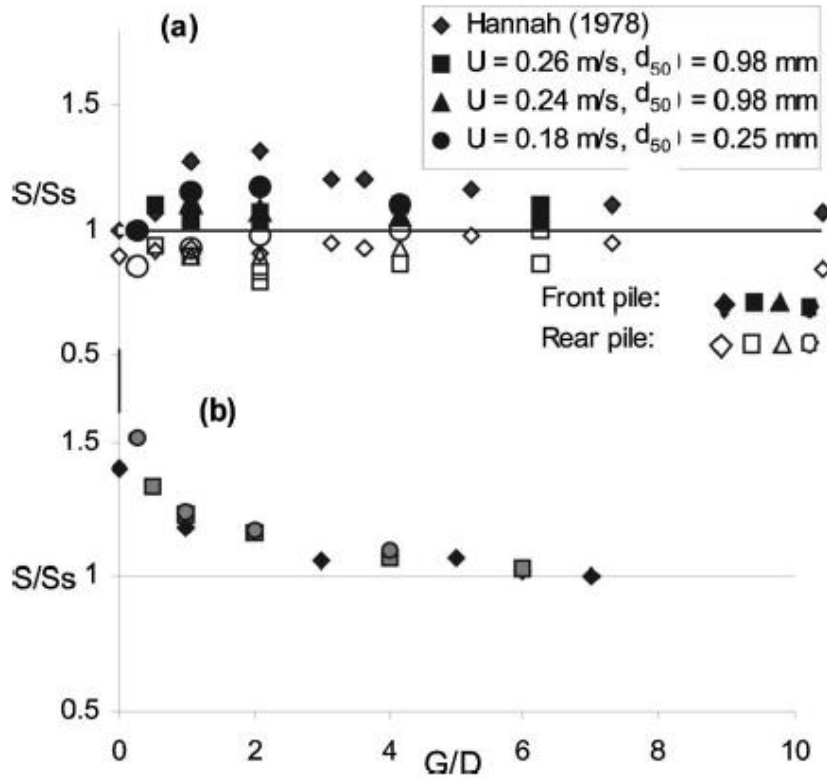


**Figure 1.14 :** Equilibrium scour depth plotted against pile spacing: (a) 1x2 pile group; (b) 2x1 pile group (Ataie-Ashtiani and Beheshti, 2006)



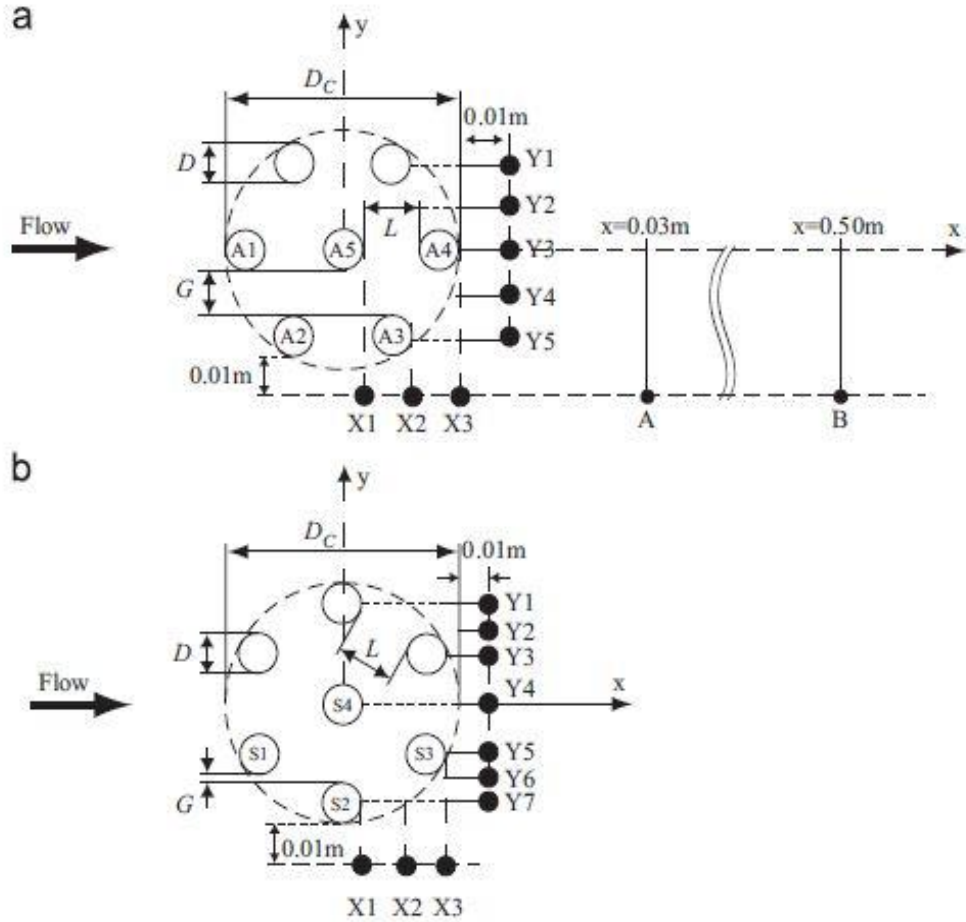


**Figure 1.15 :** Definition of the colony model and measurement points of velocity.  $D$ :diameter of cylinder,  $L$ :spacing of the cylinders,  $D_c$ : outer diameter of the colony model,  $G$ : spacing of each cylinder in cross-stream direction, the number inside the cylinder, e.g., A1, distinguishes each cylinder's position. (a) grid arrangement, (b) staggered arrangement. The velocity of the detour flow past the colony model and the velocity through the colony model are measured at points indicated by closed circles (Ataie-Ashtiani and Beheshti, 2006)

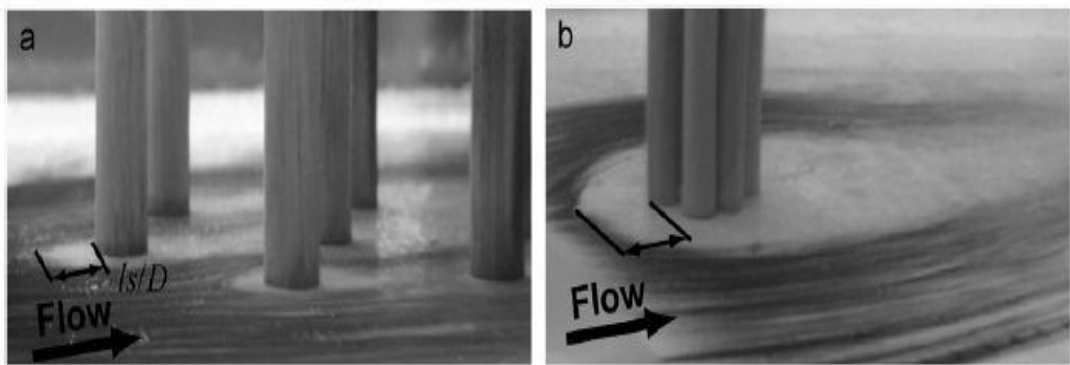


**Figure 1.16 :** Visualized flow pattern around the colony model with a grid arrangement for  $U = 0.4m/s$ . (a)  $L/D = 3$ , (b)  $L/D = 0.5$ . The arrow shows the flow direction.  $l_s$  is the width of the separation zone in front of the first cylinder at the upstream. (Takemura and Tanaka, 2007)

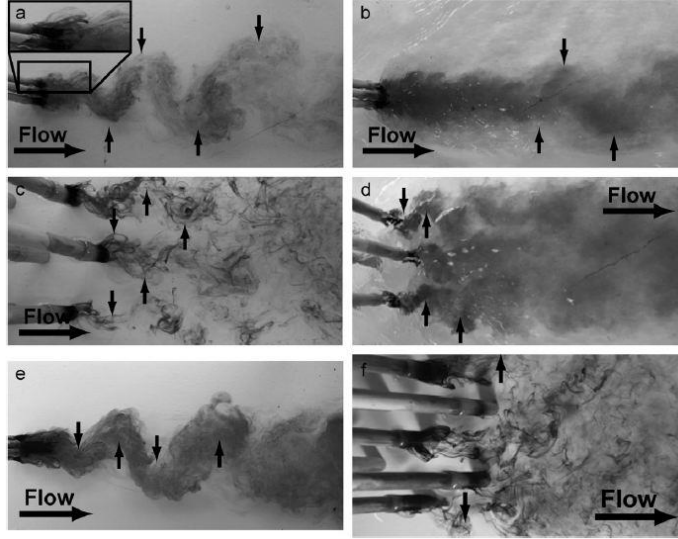


**Figure 1.17 :** Flow pattern in the wake of the colony model. (a)  $L/D = 0.5$ , grid arrangement ( $Re = 400$ ; the zoom photograph is inserted at the upper left corner, (b)  $L/D = 0.5$ , grid arrangement ( $Re = 4000$ ), (c)  $L/D = 3$ , grid arrangement ( $Re = 400$ ), (d)  $L/D = 3$ , grid arrangement ( $Re = 4000$ ), (e)  $L/D = 0.5$ , staggered arrangement ( $Re = 400$ ) and (f)  $L/D = 3$ , staggered arrangement ( $Re = 400$ ). The small arrows show the positions of LKV ((a), (b) and (e)) or PKV ((c), (d) and (f)) behind the colony model (Takemura and Tanaka, 2007).

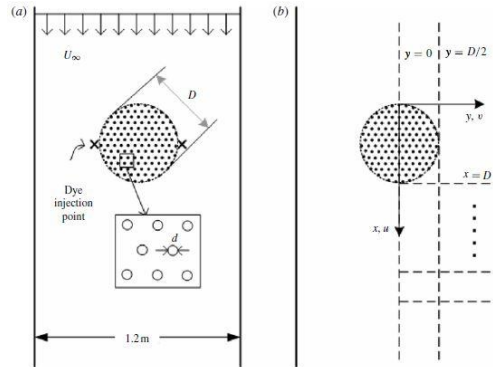


**Figure 1.18 :** Top view of experiment setup. (a) Patch configuration and dye injection points; (b) longitudinal and lateral transects (dashed lines) of velocity measurements.  $x = 0$  is at the upstream edge of the patch,  $y = 0$  is at the centreline of the patch (Zong and Nepf, 2011).

According to the results of the study, different from the wake behind a solid body, the wake behind a porous body has two unique features. One of these two is a steady wake region behind the body, which extends at a distance  $L_1$ .  $L_1$  increases when porosity increases. The other feature of the wake behind a porous body is the von-Karman vortex street, which forms beyond  $L_1$ . The flow behind the patch is slower than the flow passing around the patch. Until  $L_1$ , in the steady wake region, the stream wise velocity at the centreline remains nearly constant. Individual cylinders

create small-scale turbulence right behind them in their wakes and shear layers occur at both sides of the patch wake. These two shear layers grow independently until  $L_1$  which signifies the end of the steady wake.

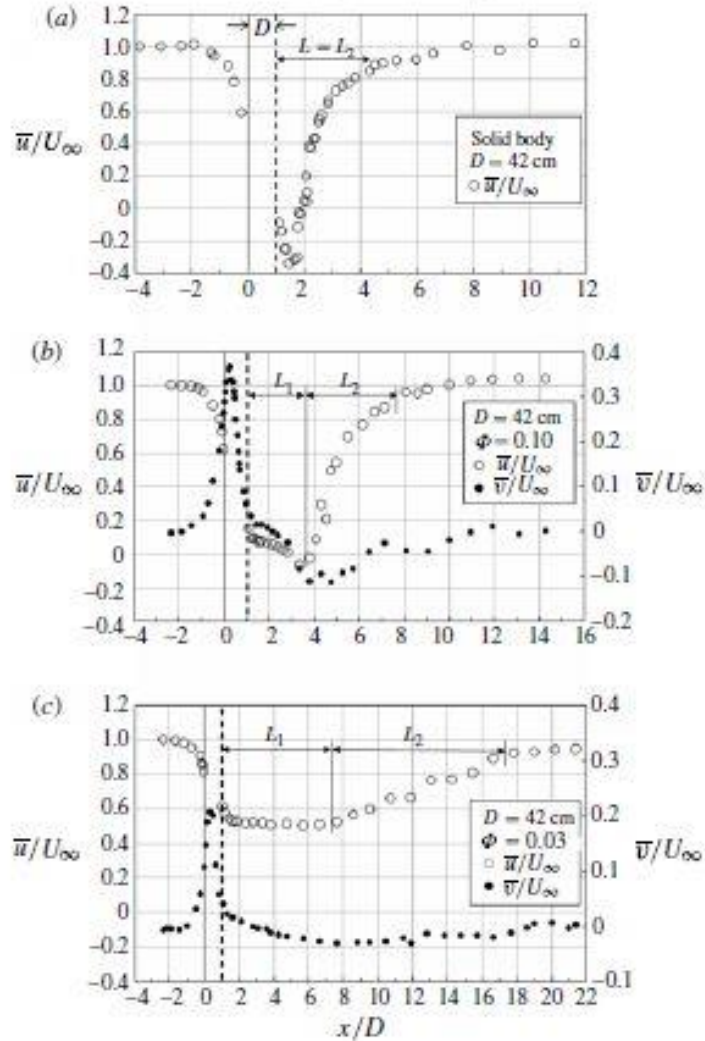


**Figure 1.19 :** Longitudinal profiles of velocity for patches with  $D = 42$  cm: (a) solid body,  $\phi = 1$ , (b)  $\phi = 0.10$ , (c)  $\phi = 0.03$ . Patch is from  $0 < x = D < 1$ . The dashed line indicates the downstream end of the patch. Note that the longitudinal velocity (open circles) is given on the left-hand axis, and the lateral velocity (filled circles) is given on the right-hand axis. The longitudinal velocity ( $u$ ) is measured at centreline,  $y = 0$ . The lateral velocity ( $v$ ) is measured at  $y = D/2$  (Zong and Nepf, 2011).

After  $L_1$ , when steady wake is over, a von-Karman vortex street starts by the interaction between the two shear layers. The turbulence scale is the scale of the patch in this region. When the maximum turbulence intensity behind the patch here is compared with the one behind a solid body, this one is smaller. Thus, the velocity deficit decays slower.

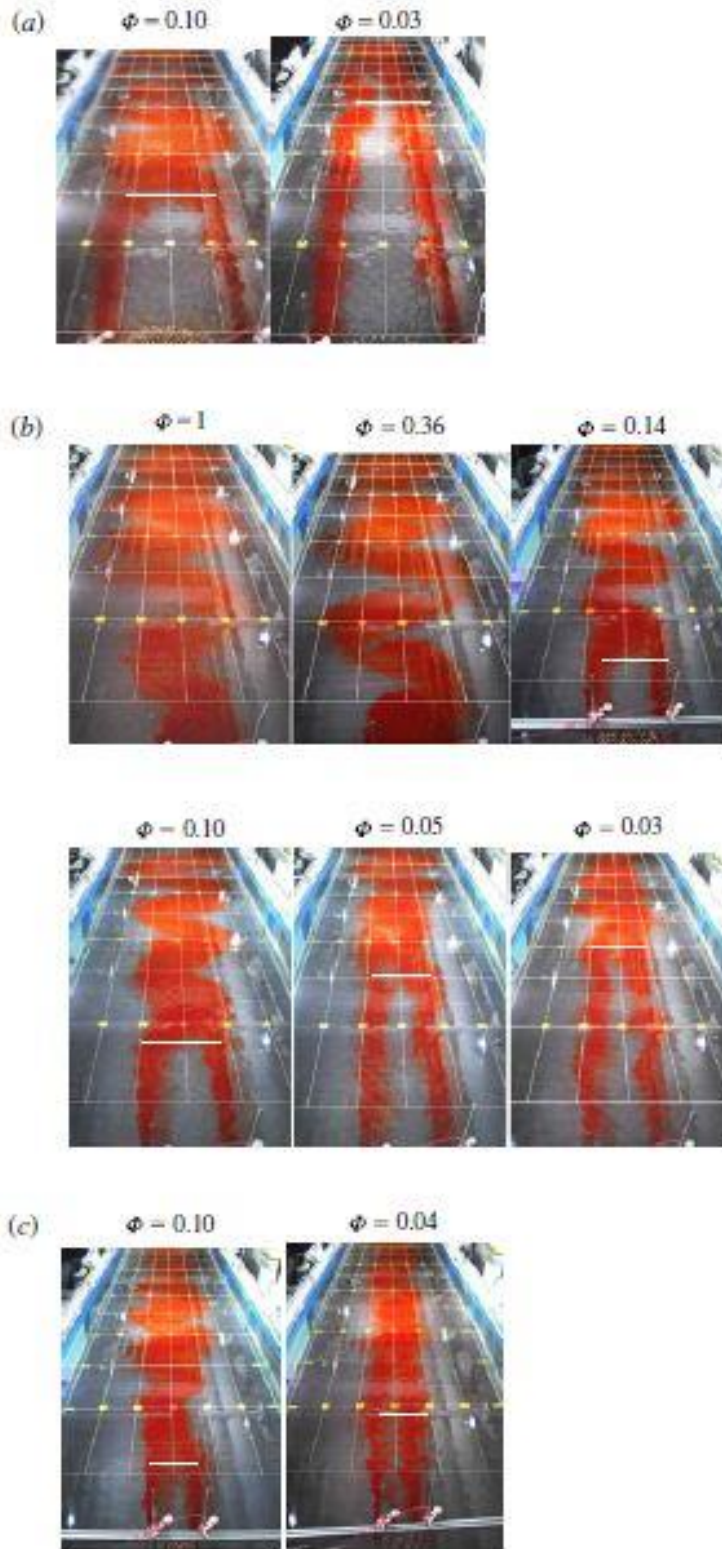


**Figure 1.20 :** Flow visualization. The patch is just out of sight at the bottom of each picture. Flow is from bottom to top. The dye was injected at the two outmost edges of the patch. The struts holding the dye injector are visible in some of the pictures. The white grid starts at  $x = 50$  cm (from the leading edge of the patch) and marks the distance of 50 cm in the  $x$ -direction and 20 cm in the  $y$ -direction. The yellow crosses mark 1 m intervals. The horizontal White bar indicates the end of the steady wake.  
(Zong and Nepf, 2011)

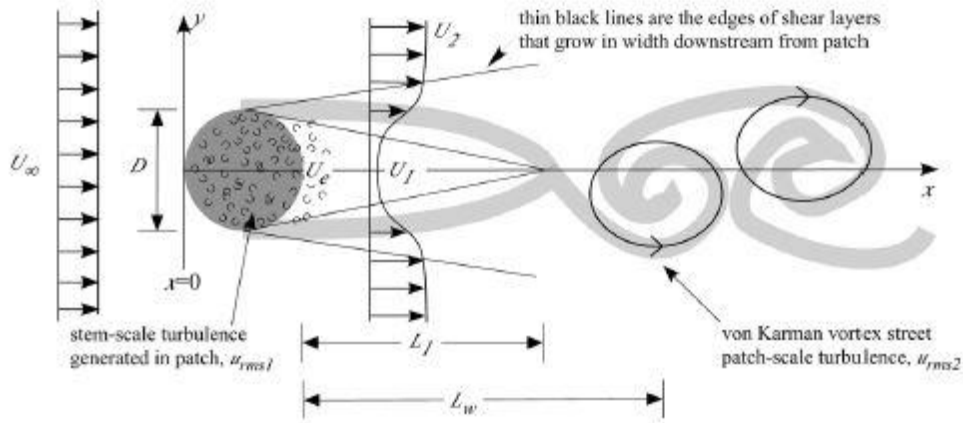


**Figure 1.21 :** Top view of a circular patch of emergent vegetation, shown by dark gray circle of diameter  $D$ . Injections of dye at the outer edges of patch (thick gray lines) reveal the evolution of the wake. Velocity exiting the patch ( $U_e = u(x = D)$ ) is diminished relative to upstream velocity ( $U_\infty$ ). The velocity decreases further to the steady wake region ( $U_1$ ). The flow within the wake delays the onset of the von Karman vortex street to the end of the steady wake,  $x = L_1 + D$ . The wake contains two scales of turbulence: stem-scale turbulence (shown with small thin semicircles), which peaks within the patch, and patch-scale turbulence (black circles with arrows), which peaks at  $x = L_w + D$  (Chen et al., 2012).

In Chen et al. (2012), the mean and turbulent flow structure in the wake of a circular array of cylinders, which is a model for a patch of emergent vegetation, are investigated experimentally (Figure 1.20). This study showed the existence of two peaks in the turbulence intensity in the wake behind the patch. The first peak is at the scale of the individual cylinders and it occurs directly behind the patch. The second peak is related to the wake-scale vortices of the von-Karman vortex street. It occurs at the distance  $L_w$ . With decreasing flow blockage,  $U_e$  increases and it delays the formation of the von-Karman vortex street. When  $U_e$  increases, both  $L_w$  and  $L_1$  increase. This affects the place of the deposition behind the obstruction (Figure 1.21).





## 2. EXPERIMENTAL SETUP

### 2.1 Experimental Facilities

#### 2.1.1 The flume

The experiments were performed in the flume in Istanbul Technical University Hydraulics Laboratory. The bottom of the flume is made of concrete and sided by Plexiglas. It is 26 m in length, 0.98 m in width and 0.85 m in depth. In order to place a sand pool in the flume, a false bottom was built by using metal sheets. The height of the false bottom is 20 cm and the length is 14.5 m. A 3.5 m long sandpit was placed in the false bottom. The profile view of the flume was drawn and can be seen in Figure 2.1. A photograph of the flume can also be seen in Figure 2.2.

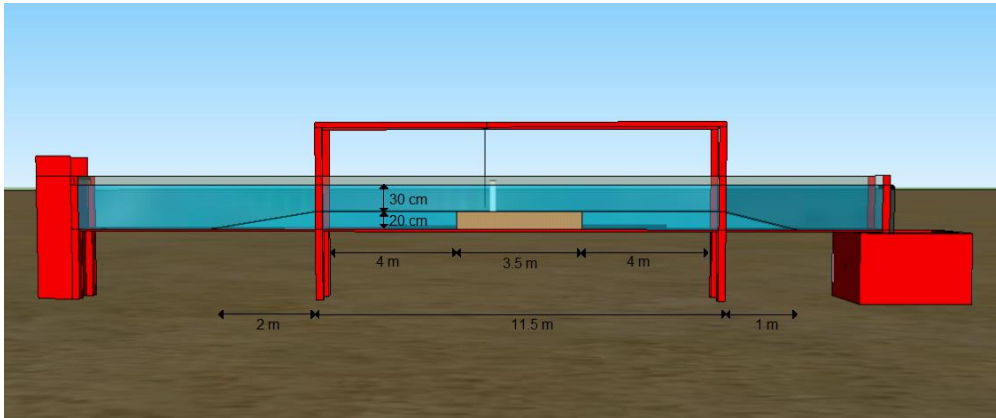


**Figure 2.1 :** Drawing of the flume where the experiments were conducted.



**Figure 2.2 :** The flume where the experiments were conducted.

At the upstream side of the false bottom, a metal sheet was placed with an angle of 1V/10H in order to keep the flow undisturbed. At the end of the false bed, the angle of the metal sheet is smaller and it is 1V/5H. To be able to drain the sandpit after every experiment, two drainage pipes were placed in the false bottom as can be seen in Figure 2.3.

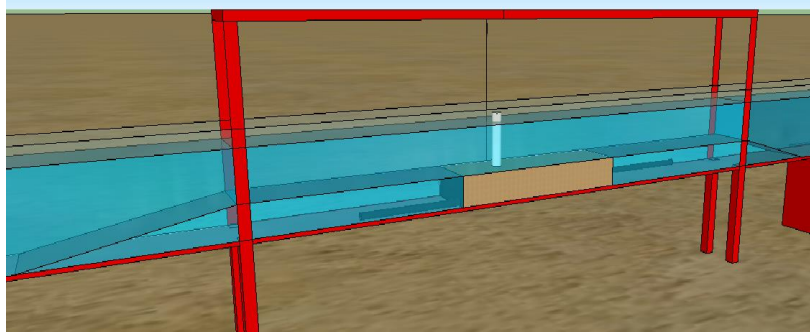


**Figure 2.3 :** Details of the sand bottom and drainage pipes.

### 2.1.2 The bed material

In the experiments, quartz sand was used as bed material. After the small grains were washed away during the preliminary experimental run, the geometric standard deviation of the sand sample (Sample 1) was  $\sigma_g = 1.86$ , while before the first experiment (Sample 2) it was  $\sigma_g = 1.84$ . Since the uniformity of the sediment is supposed to be constant, the geometric standard deviation was checked after the 9<sup>th</sup> experiment (Sample 3). It was  $\sigma_g = 1.85$ , which showed that the sediment uniformity was kept constant throughout the experiments. The grain size curves of the samples can be seen in Figure 2.4.

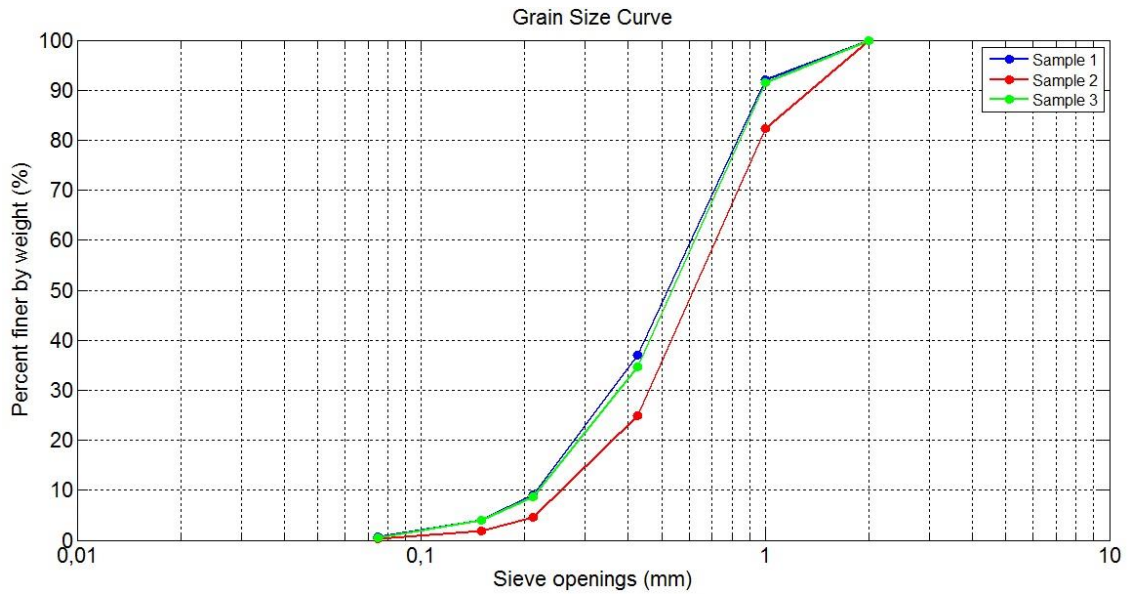


**Figure 2.4 :** Grains size distribution for sand samples.



### **2.1.3 The pumps**

The external pump that was used in the laboratory has a power of 25 kW. In the experiments, the external pump and two other internal recirculating pumps were used. The internal pumps were used in order to increase the discharge by taking the water from downstream of the flume and release it to the upstream again.

### **2.1.4 The measurement devices**

The Vectrino Velocimeter, which is developed by Nortek, measures water velocity by using the Doppler Effect. It sends a short pulse of sound listens to its echo and measures the change in pitch or frequency of the echo. The device was used with Vectrino Plus computer program and it has a maximum sampling rate of 200 Hz (Vectrino User Guide, 2011). The Vectrino I was placed at the upstream part of the flume where the flow was undisturbed in order to check the discharge and flow velocity.

The Vectrino II, also developed by Nortek, has the same working principle with Vectrino I. They both use the Doppler Effect to measure flow velocity. The main difference between them is the measuring points. While Vectrino I can measure the flow velocity at only one point, Vectrino II can measure the velocity in up to 36 points within the sampling volume. Vectrino II was used with Vectrino Profiler computer program and it has a maximum sampling rate of 100 Hz (Vectrino User Guide, 2011). It can also measure the bottom distance, which is the distance between the main probe and the bottom of the flume. It was placed in front of the cylinders in every experiment. The distance between the main probe and the cylinder surface was constant for every experiment and it was 5.3 cm.

Laser Scanners are the devices, which can do modelling study in three dimensions with high speed and high accuracy. The object or the area that is scanned with a laser scanner can be seen in different angles in computer environment and calculations can be made on it. In the experiments, in order to see the final scour condition and determine the scour parameters, a laser scanner, which is developed by LEICA, Scanstation C10, was utilized (Figure 2.5). This instrument is a pulse-based model that measures the coordinates of a point by sending a laser light and calculating its returning time. Scanstation C10 can scan 360° horizontally and 270° vertically. The measurement distance is maximum 300 m and minimum 0.1 m. The scanning rate is 50000 points per second. The device also has a 4-megapixel camera as an imaging tool.



**Figure 2.5 :** The laser scanner.

## **2.2 Model Pile Characteristics**

In order to understand the scour mechanism in uniform flow conditions, 16 sets of experiments were conducted. These 16 sets include four solid cylinder experiments with the diameters of 9 cm, 12 cm, 16 cm and 20 cm. For the other twelve experiments, a porous element, comprising seven small cylinders of 3.4 cm diameter, was placed in different geometries and orientations to see the effect of porosity and angle to the flow, respectively. The porous cylinder groups will be called HACC (Hexagonal Array of Circular Cylinders). (Figure 2.6) In HACCs, the angle between individual cylinders is  $60^\circ$ . The details and geometric characteristics of an HACC can be seen in Figure 2.7. During the transition from regular to angled cases and from angled to staggered cases, HACCs were rotated  $15^\circ$  in plan view in counter clockwise direction (Figure 2.8). The geometric characteristics of obstacle types that were used in the study can be seen in Table 2.1.

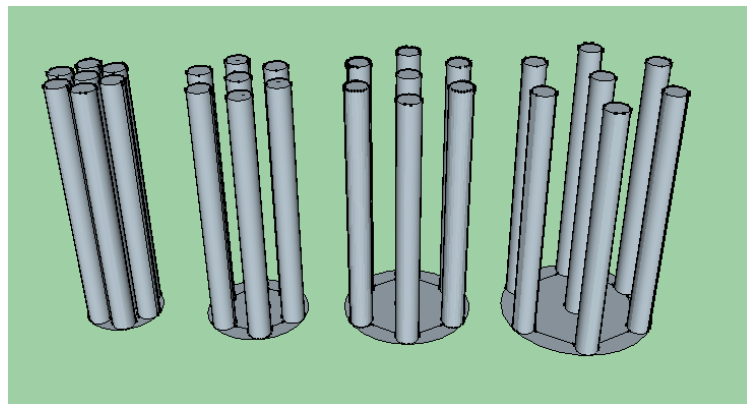


**Figure 2.6 :** The perspective view of the HACCs which were used in the experiments.

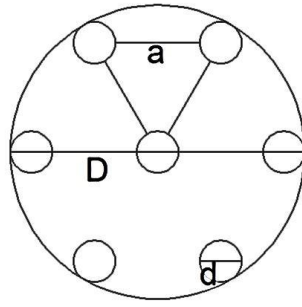


**Figure 2.7 :** The geometry of the obstacles.

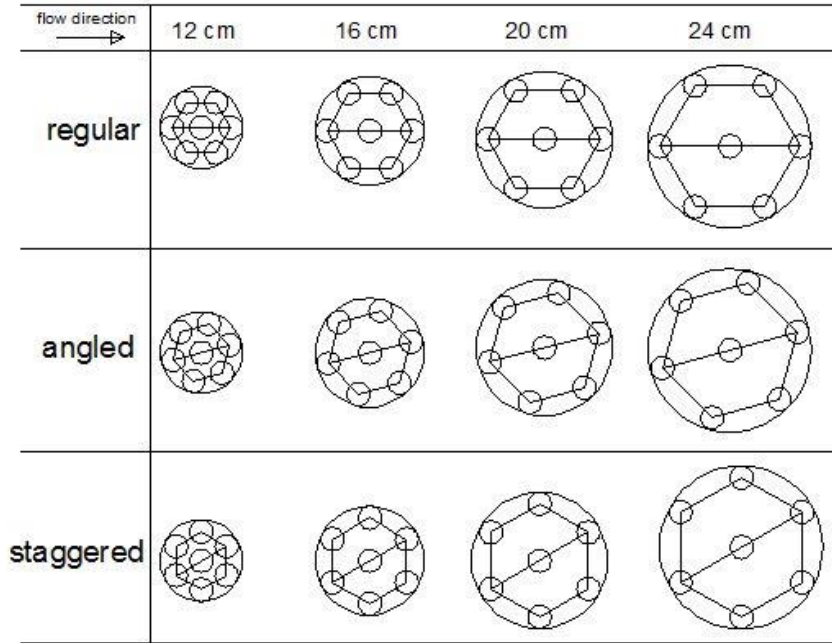


**Figure 2.8 :** The experimental configurations and orientations.

**Table 2.1 :** Geometric characteristics of obstacle types.

Obstacle type	D (cm)	d (cm)	a (mm)
12 cm HACC	12	3.4	9
16 cm HACC	16	3.4	29
20 cm HACC	20	3.4	49
24 cm HACC	24	3.4	69

### 2.3 Experimental Procedure

For each experiment, first the pile model was placed and fixed in the middle of the flume, 11 m downstream of the flume inlet. Then, the sand bottom was smoothed out by using traditional trowel (Figure 2.9). In order not to disturb the sand bottom, the flume was filled slowly, so it took 3 to 4 hours.



**Figure 2.9 :** Preparation of the flume.

The Vectrino II Profiler was placed 5,3 cm away from the obstacle surface and 8.5 cm above from the initial sand bed for each experiment as can be seen in Figure 2.10. The poition of Vectrino II in front of an obstacle can be seen in Figure 2.11.



**Figure 2.10 :** Vectrino II in front of the 16 cm staggered HACC.

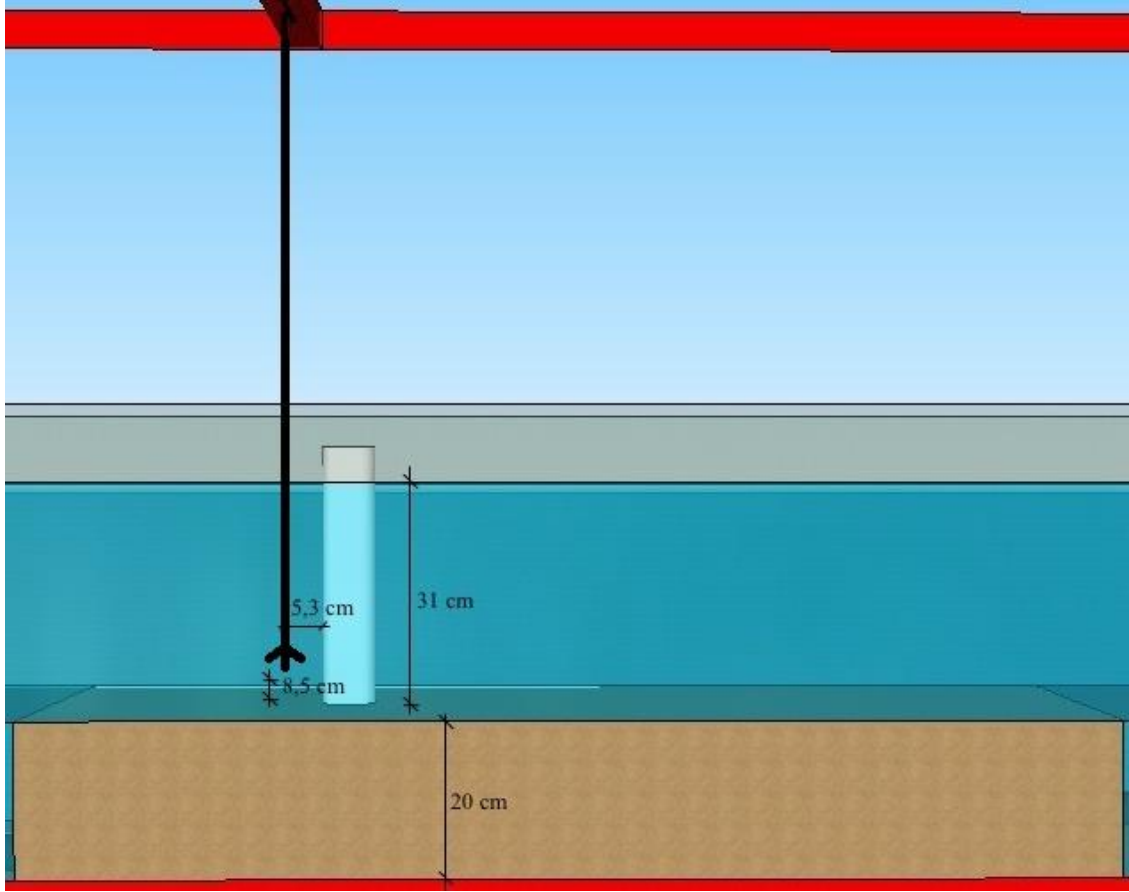


**Figure 2.11 : Position of Vectrino II.**

Right after Vectrino II Profiler was started, the pumps were started as well. Each experiment took 8 hours except the 20 cm solid cylinder experiment, which was stopped when the scour depth reached 20 cm.

The flow discharge per unit width was set to  $q = 88 \text{ l/s/m}$  and the flow depth  $h = 31 \text{ cm}$ . Hydraulic radius ( $R$ ), was calculated by using the formula (2.1) where  $A$  is cross sectional area of flow and  $U$  is wetted perimeter (Sumer et al., 1981).

$$R = \frac{A}{U} \quad (2.1)$$

The bed shear stress for undisturbed bed ( $\tau$ ) was calculated by using the formula (2.2), where  $\gamma$  is the specific weight of the water,  $R$  is hydraulic radius and  $J$  is the bed elevation (Sumer et al., 1981).

$$\tau = \gamma R J \quad (2.2)$$

$u_f$  is the skin friction velocity which was calculated by using the formula (2.3) where  $\tau$  is the bed shear stress and  $\rho$  is the density of water (Fredsoe and Deigaard, 1992).

$$u_f = \sqrt{\frac{\tau}{\rho}} \quad (2.3)$$

$d_{50}$  represents the grain diameter which the 50% by weight of the sediment grains are finer than.  $\theta$  is the Shields parameter and calculate by using the formula (Sumer et al., 1981):

$$\theta = \frac{u_f^2}{(s - 1)gd} \quad (2.4)$$

where  $u_f$  is the skin friction velocity,  $s$  is the relative density of the sediment,  $g$  is the acceleration of gravity and  $d$  is the gran diameter and  $\theta_c$  was determined by using the Shields diagram. These characteristics are shown in Table 2.2.

**Table 2.2 :** The experimental characteristics.

Q (m <sup>3</sup> /sec)	q (m <sup>3</sup> /sec/m)	R (m)	$\tau$ (kN/m <sup>2</sup> )	$u_f$ (m/s)	$d_{50}$ (mm)	$\theta$	$\theta_{cr}$	$\theta / \theta_{cr}$	Re	Fr
0.0865	0.0883	0.19	0.000186	0.0136	0.523	0.022	0.06	0.3657	7164	0.106

For each experiment, the flow discharge was estimated by measuring the undisturbed flow velocity and water depth throughout the experiments. A point gage was used to check the water level. Even though the water level sometimes showed minor differences (at mm magnitude), the discharge was considered constant.

After each experiment, when the flow was entirely stopped, by using the discharge valve, the water in the flume was drained slowly. When the bed surface was completely dry, the laser scanner was used in order to obtain the three dimensional geometry of the final sand bed geometry.

For each experiment, the data from the Vectrino II Profiler and laser scanner were used in order to compare the results of the experiments. The aim was to see the differences between the porous configurations and the 9 cm solid cylinder, which has the same cross sectional area with the HACCs.



### 3. RESULTS AND DISCUSSION

After each experiment, a conical scour hole around the pier model occurred, as expected, and at the downstream of the model, a deposition area was formed (Figure 3.1 and Figure 3.2). For each experiment, the durations and the final conditions are discussed in the following sections.



**Figure 3.1 :** Scour hole and deposition zone for 20 cm regular HACC.

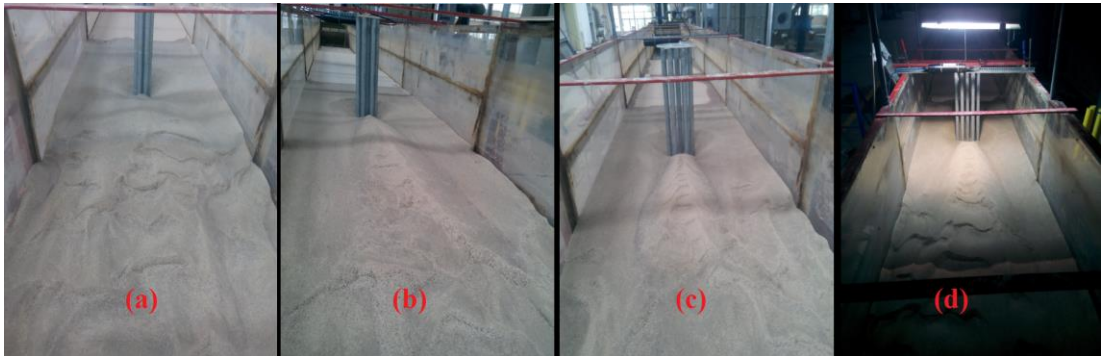


**Figure 3.2 :** The final bed topographies for (a) 12 cm staggered HACC, (b) 16 cm staggered HACC, (c) 20 cm staggered HACC and (d) 24 cm staggered HACC.



**Figure 3.3 :** Scour hole and deposition zone for 24 cm angled HACC.

### 3.1 The Change in the Bottom Distance Over Time

During the experiments, the distance between the probe of the Vectrino Profiler and the bottom of the flume was measured for 8 hours. The results of this measurement can be seen in Figures 3.3 - 3.6, in which the graphs were drawn in groups according to the cylinder diameters, while in Figures 3.7 - 3.10 they were drawn according to the orientations.

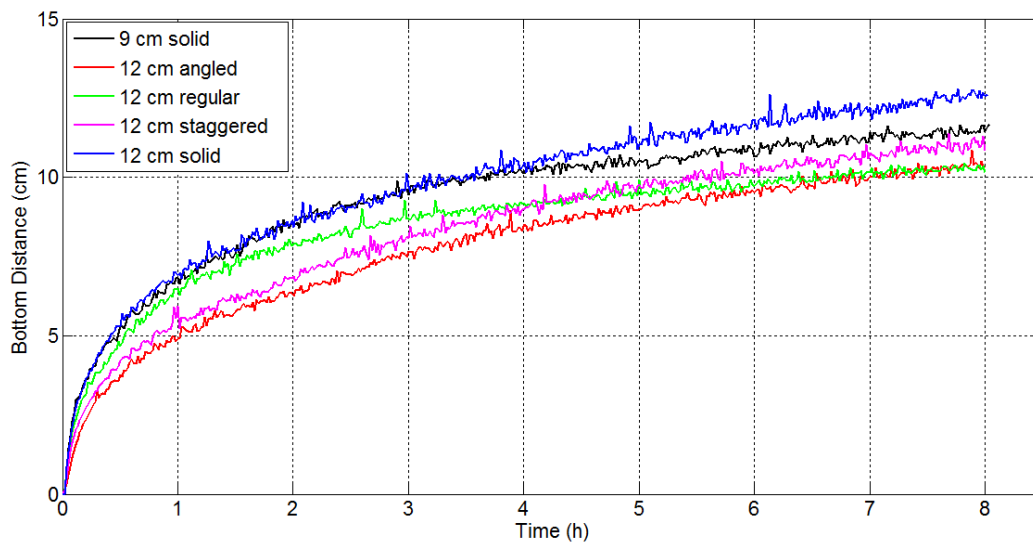


**Figure 3.4 :** The variation of scour depth with respect to time observed throughout the experiments for 12 cm HACC cases.



For the 12 cm HACC cases, all porous configurations (i.e. regular, staggered, and angled) caused less scour than the 9 cm solid cylinder at the point where Vectrino II was placed. However, the 12 cm solid cylinder experiment resulted in a deeper scour depth at the end of eight hours. It was also observed that the 12 cm regular porous cylinder caused more scour than the 12 cm staggered one at the end of the 4<sup>th</sup> hour of the experiment. But after that the evolution of scour slowed down and at the end of the experiment, the 12 cm staggered porous configuration caused more scour than the regular and angled ones, as it is seen in Figure 3.3. Regular and angled configurations had almost the same scour depth at the point where Vectrino II was placed at the end of eight hours. It is clear that for all the 12 cm HACC experiments and 9 cm solid case, scour evolved more rapidly at the beginning of each experiment.

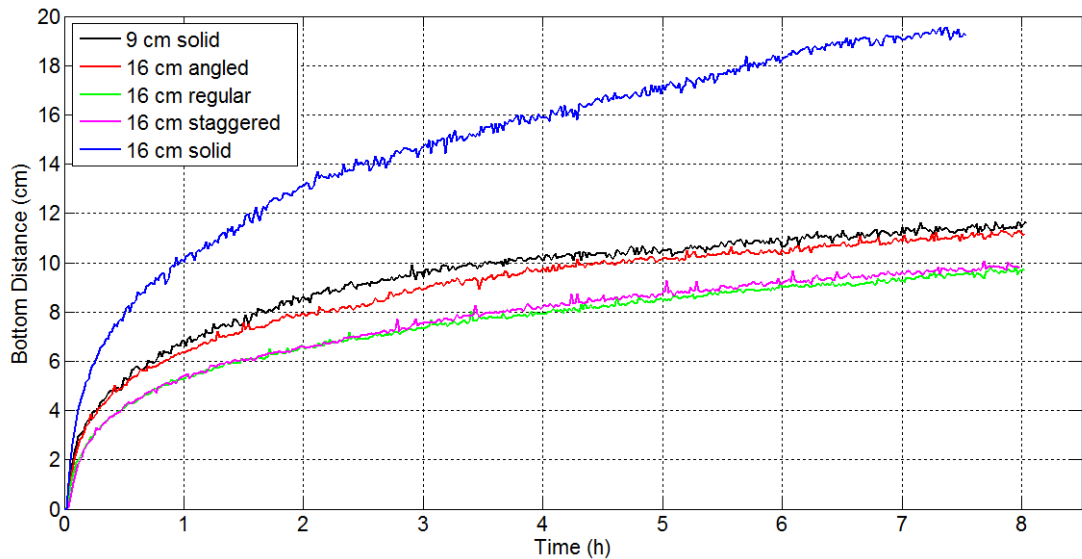


**Figure 3.5 :** The variation of scour depth with respect to time observed throughout the experiments for 16 cm HACC cases.

For the 16 cm HACC cases, similar to the 12 cm HACC cases, porous configurations resulted in less scour than the 9 cm solid cylinder. As can be seen in Figure 3.4, the 16 cm solid cylinder caused significantly more scour than the other 16 cm HACC configurations or the 9 cm solid cylinder even though the 16 cm solid cylinder experiment took 7.5 hours instead of 8. It was also observed that the regular and the staggered cylinders had almost the same scour development pattern until the middle of the 3<sup>rd</sup> hour. However, at the end of 8 hours the 16 cm staggered porous HACC deviated from the pattern of the regular one. Among the 16 cm HACC cases, the angled configuration caused the most scour, at the point where Vectrino II was placed, at the end of the 8<sup>th</sup> hour.

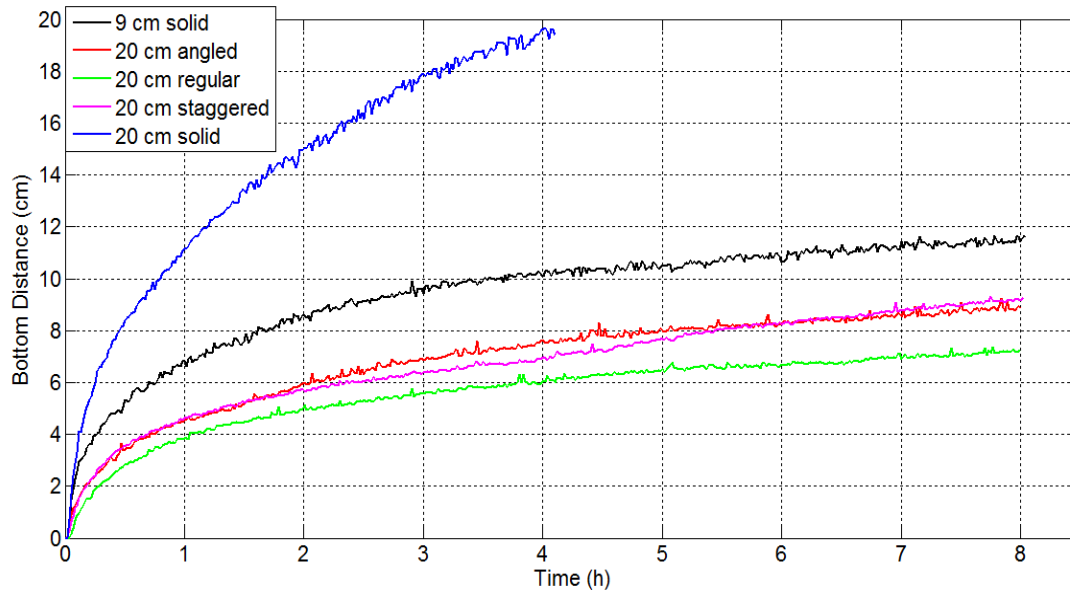


**Figure 3.6 :** The variation of scour depth with respect to time observed throughout the experiments for 20 cm HACC cases.

For the 20 cm HACC cases, like the previous two diameters, porous configurations caused less scour than the 9 cm solid cylinder. For this diameter, angled and staggered arrangements exhibited similar time series. For the regular arrangement significantly less scour was observed at the point where Vectrino II was placed. As seen in Figure 3.5, the 20 cm solid cylinder reached a scour depth of nearly 20 cm after 4 hours when the experiment was interrupted before the scour depth attained to the bottom of the false bed.

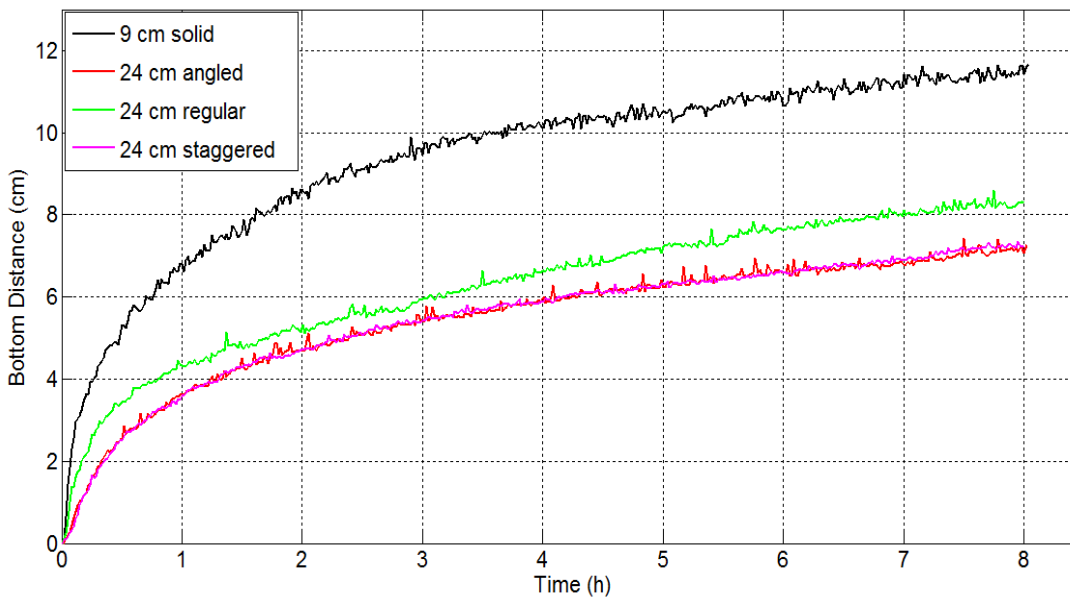


**Figure 3.7 :** The variation of scour depth with respect to time observed throughout the experiments for 24 cm HACC cases.

For the 24 cm HACC cases, all three arrangements caused distinctly less scour than the 9 cm solid cylinder as can be seen in Figure 3.6. In these experiments, angled and staggered arrangements exhibited almost the same evolution pattern for 8 hours. It was seen that regular arrangement caused slightly higher scour compared to other HACC cases.

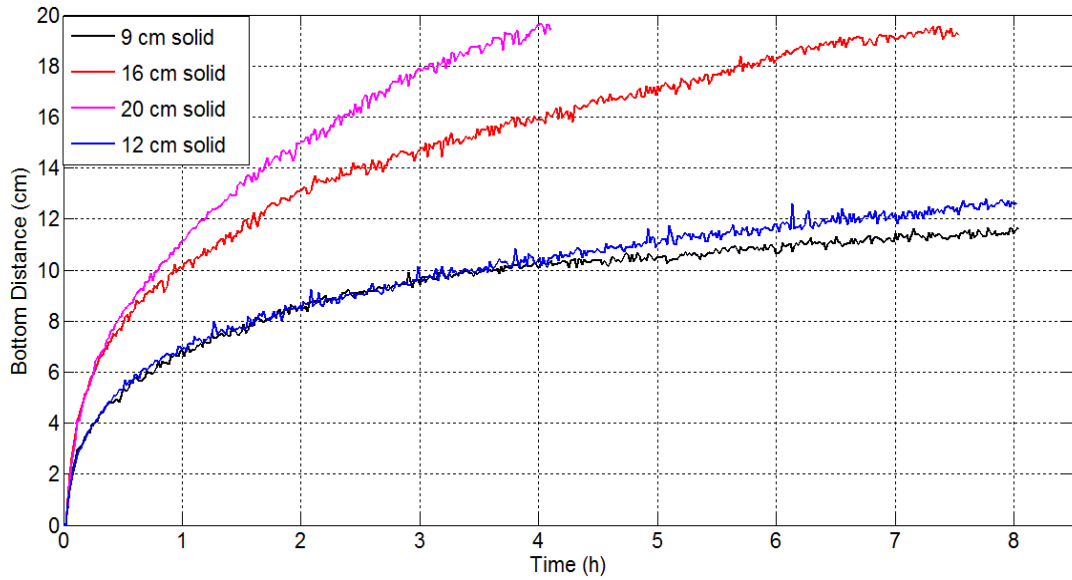


**Figure 3.8 :** The variation of scour depth with respect to time observed throughout the experiments for solid cylinder cases.

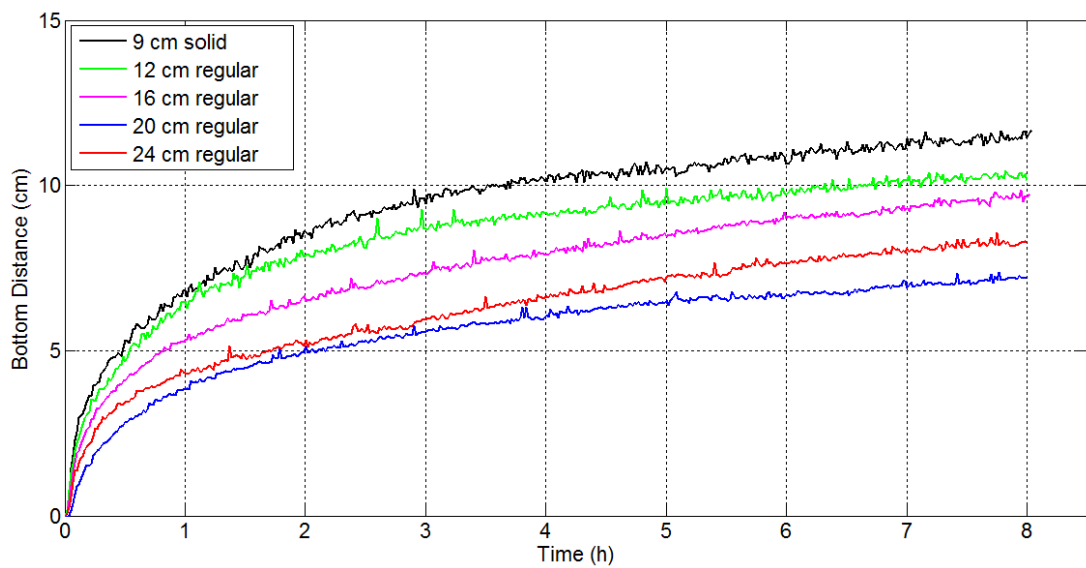


**Figure 3.9 :** The variation of scour depth with respect to time observed throughout the experiments for regular HACC cases.

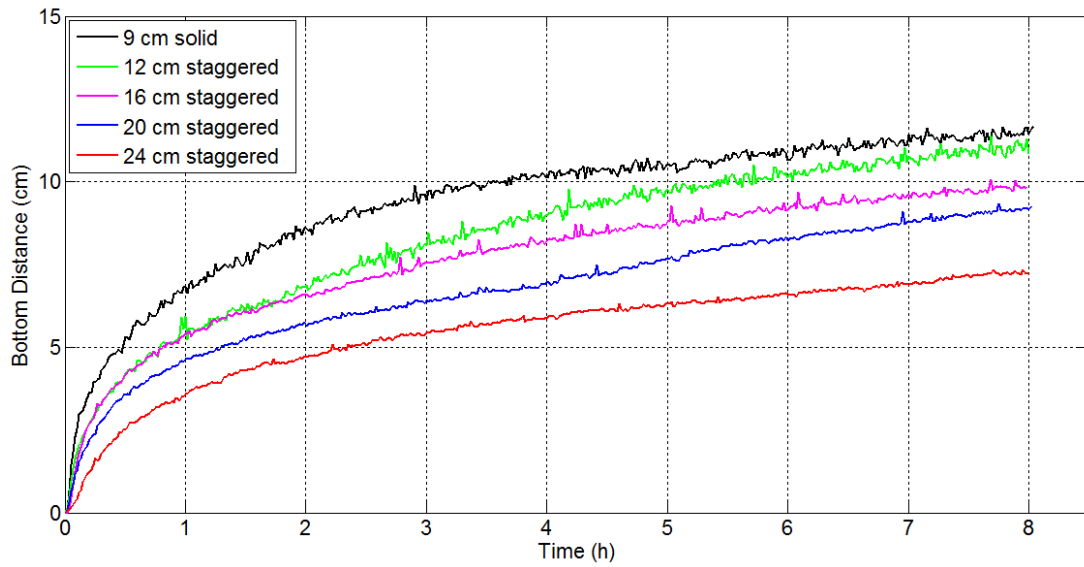


**Figure 3.10 :** The variation of scour depth with respect to time observed throughout the experiments for staggered HACC cases.

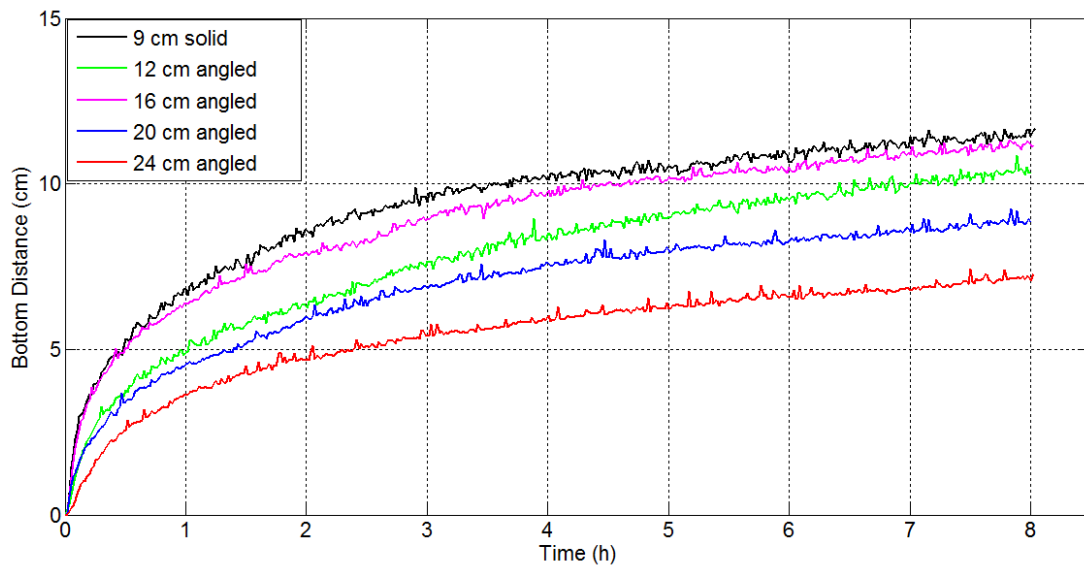


**Figure 3.11 :** The variation of scour depth with respect to time observed throughout the experiments for angled HACC cases.

In solid cylinder experiments, as diameter increases, the scour depth increases as well, as expected according to the pertinent literature. (Figure 3.7)

If the experiments are categorized according to the arrangements of the HACCs, the difference between the scour depths can be seen for the same orientation but different cylinder diameters.

As seen in Figure 3.8, for regular orientation, the highest scour depth value was seen for 12 cm regular HACC. Throughout the experiments, the order of the scour depth at the point where Vectrino II was placed remains the same. While the 24 cm regular HACC causes more scour than the 20 cm regular HACC, it causes less scour than the 12 and 16 cm regular HACCs.

For staggered orientations, scour depth is inversely proportional with the HACC diameter. As the diameter increases, the scour depth decreases. Therefore, the deepest scour at the point where Vectrino II was placed was caused by the 12 cm staggered HACC (Figure 3.9).

In angled cases of HACC, differing from the other orientations, the deepest scour was caused by 16 cm angled HACC which was followed by 12 cm, 20 cm and 24 cm, respectively. As seen in Figure 3.10, it was observed that the 16 cm angled HACC and the 9 cm solid cylinder showed nearly the same scour evolution during the first 30 minutes of the experiment. However, at the end of the 8<sup>th</sup> hour, the scour depth of the 9 cm solid cylinder was higher than one of the 16 cm HACC.

### 3.2 Comparison of HACCs with 9 cm Solid Cylinder

As it was mentioned before, the main purpose of this thesis is to compare 9 cm solid cylinder to the HACCs that have the same cross-sectional area. Scour depth, scour width and scour volume differences between 9 cm solid cylinder and the HACCs are shown in the Table 3.1.  $r_{ds}$  is the efficiency (scour depth reduction) at the end of the test which was presented by Tafarojnoruz et al. (2012). The formula is:

$$r_{ds} = \frac{d_{s0} - d_{sp}}{d_{s0}} \times 100(\%) \quad (3.1)$$

where  $d_{s0}$  and  $d_{sp}$  are the maximum scour depth in proximity to the unprotected and protected pier, respectively (Tafarojnoruz et al., 2012). In this study instead of  $d_{s0}$ , the scour depth of 9 cm solid cylinder, and instead of  $d_{sp}$  the scour depth of the HACCs were taken. The comparison can be seen in Table 3.1. By using the same approach, two other parameters were defined.  $r_{ws}$  is the efficiency of scour width reduction and  $r_{vs}$  is the scour volume reduction, also can be seen in Table 3.1. According to these results, the best efficiency belongs to the 20 cm staggered HACC in terms of scour depth reduction. It was followed by 24 cm regular HACC with 22% and 24 cm angled HACC with 20%. 24 cm regular HACC caused 22% of scour

reduction while the scour volume reduction for this orientation was 27%. The only HACC that caused more scour than 9 cm solid cylinder was the 16 cm angled HACC with -2%.

**Table 3.1 :** The efficiencies of HACCs according to 9 cm solid cylinder.

D (cm)	Orientation	$r_{ds}$ (%)	$r_{ws}$ (%)	$r_{vs}$ (%)
12	regular	9%	9%	15%
12	staggered	6%	6%	3%
12	angled	5%	3%	8%
16	regular	6%	-5%	5%
16	staggered	3%	0%	-3%
16	angled	-2%	-12%	-9%
20	regular	26%	10%	23%
20	staggered	14%	-7%	10%
20	angled	13%	1%	-4%
24	regular	22%	-1%	27%
24	staggered	16%	-3%	21%
24	angled	20%	0%	14%

### 3.3 The Change in Velocities in Three Dimensions

Throughout the experiments, by using Vectrino II Profiler, the velocities in three dimensions were recorded. Figures A1-A16 in Appendix A show the changes in velocities  $u$ ,  $v$  and  $w$  for 8 hours. Since the dramatic changes in the velocities were seen during the first 30 minutes of the experiments, these sections were shown separately in sub-figures “b”. In order to see the relationship between the velocities and scour depth over time, the time series of the scour depths were added to the velocity graphs.

In all the experiments, the change in the velocities was observed and they were quite similar in terms of increasing and decreasing parts. The velocity which is in the flow direction,  $u$ , increases with increasing scour depth. The most dramatic change in  $u$  is in the first approximately 10 minutes of the experiments. The velocity which is in the channel width direction,  $v$ , has the minimum change when compared to the other two velocities. No significant changes were observed. The velocity  $w$ , which represents the down flow in front of the pier model, increases with time. The dramatic change is in the first 10 minutes, similarly to  $u$ .

### 3.4 Pattern Based Assesments

For the solid cylinder cases, no distinguished ridge section was observed, as seen in Figure 3.11- Figure 3.14. However, well-developed ripples, which cover the whole cross-section, were observed for all cylinder diameters tested.

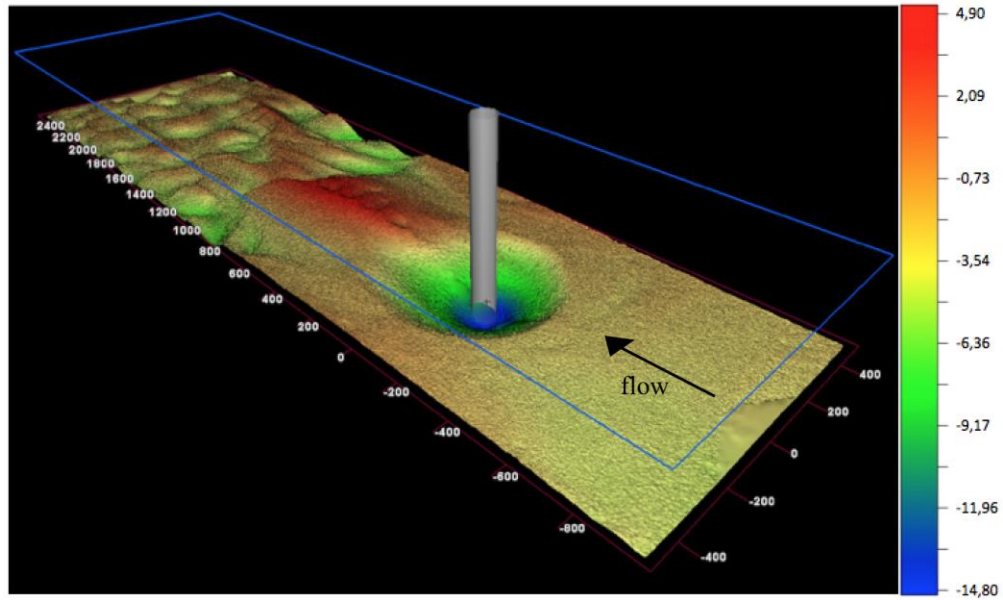


**Figure 3.12 :** Digital model of final bed topography for 9 cm solid cylinder (The dimensions on the figure are in mm and the dimensions on the legend are in cm).

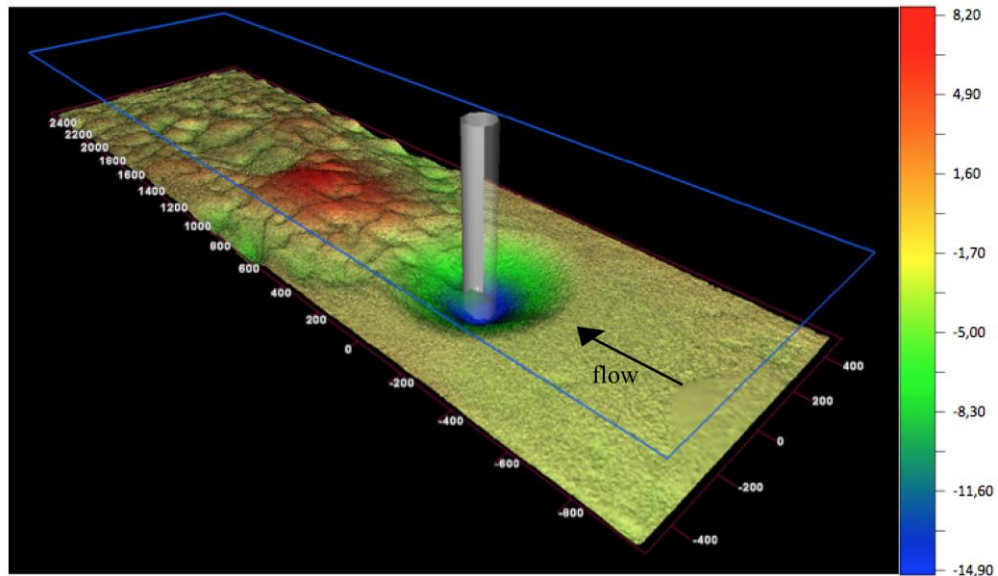


**Figure 3.13 :** Digital model of final bed topography for 12 cm solid cylinder (The dimensions on the figure are in mm and the dimensions on the legend are in cm).

According to the criteria proposed by Takemura and Tanaka (2007), the 12 cm HACC behaves like a solid cylinder. More specifically, it does not generate distinguishable ridge at the downstream of the obstacle. Moreover, its ripple



developments, which cover the entire cross-section, were observed for all cases of 12 cm HACC (i.e. staggered, regular, angled cases) (Figure 3.15- Figure 3.19).

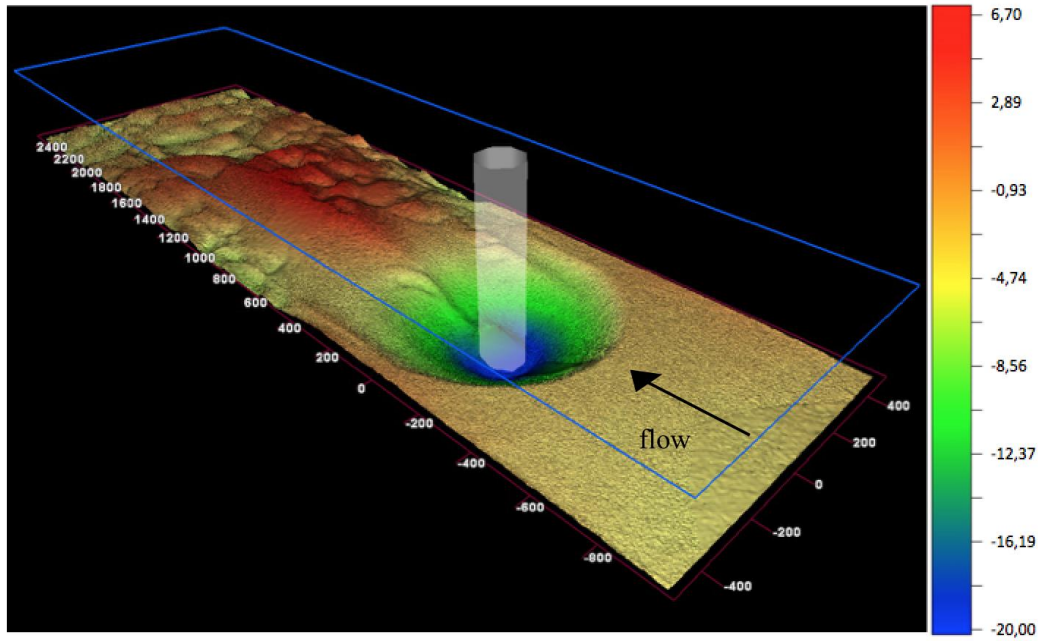


**Figure 3.14 :** Digital model of final bed topography for 16 cm solid cylinder (The dimensions on the figure are in mm and the dimensions on the legend are in cm).

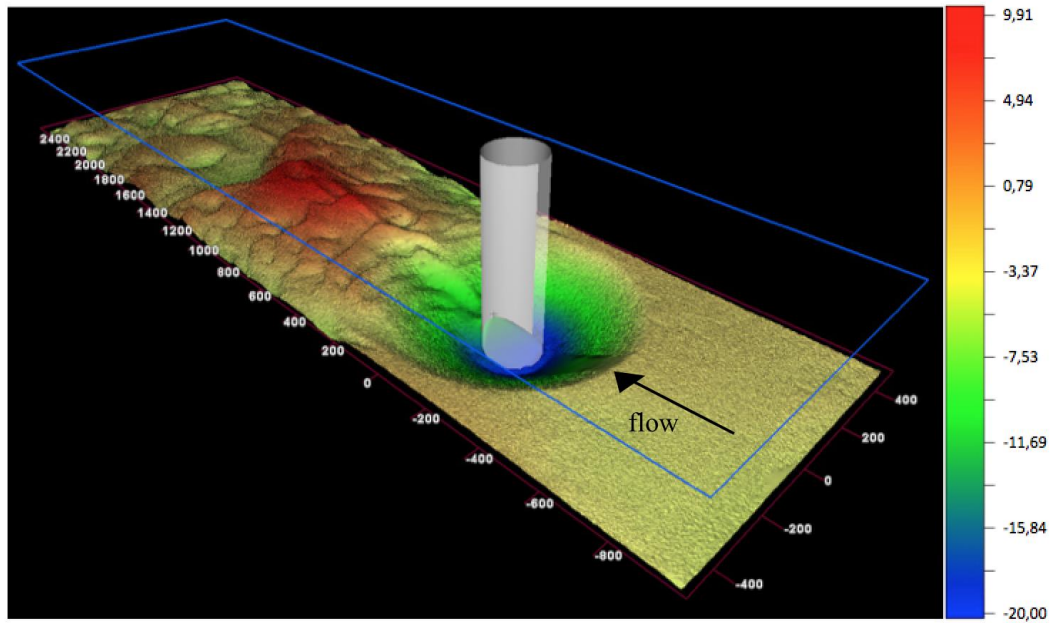


**Figure 3.15 :** Digital model of final bed topography for 20 cm solid cylinder (The dimensions on the figure are in mm and the dimensions on the legend are in cm).

For the 16 cm HACC cases, it was observed that no matter what the arrangement of the HACC was, a distinguishable ridge was observed for all cases. Different from 12 cm HACC, 16 cm HACC generated two elongated scour holes at the downstream. According to Takemura and Tanaka (2007), the staggered arrangement generates



higher drag force. This implies that staggered arrangement has less hydrodynamic form. The contourplot figures for 16 cm for staggered arrangement show that the scour holes are less elongated, which corroborates the findings of Takemura and Tanaka (2007). It was also observed that for all 16 cm HACC cases, the development of the ripples take place downstream of the ridge (Figure 3.20- Figure 3.24).

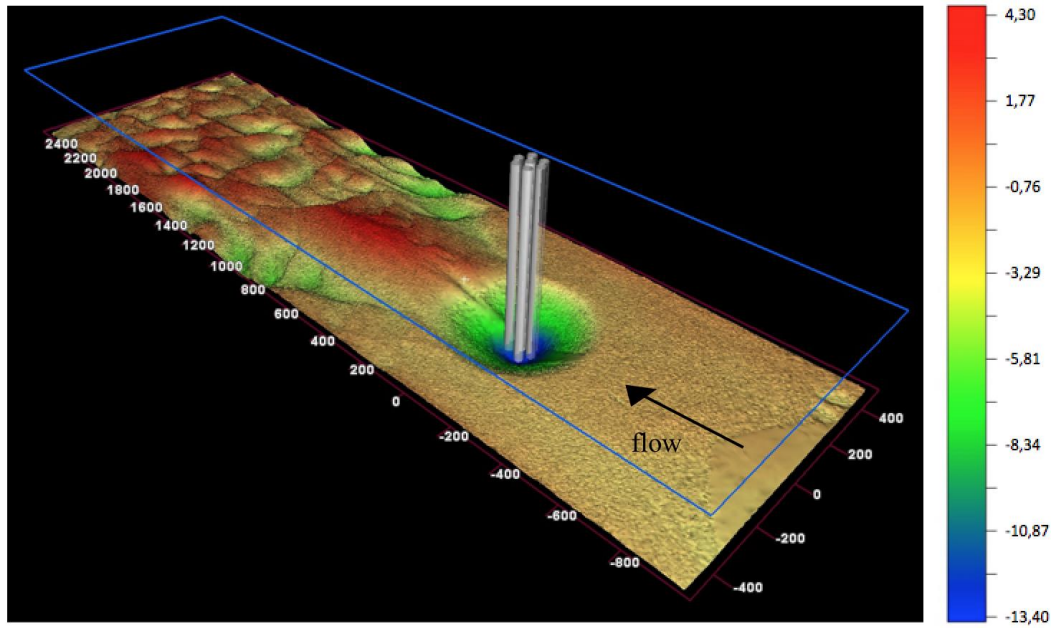


**Figure 3.16 :** Digital model of final bed topography for 12 cm regular HACC (The dimensions on the figure are in mm and the dimensions on the legend are in cm).

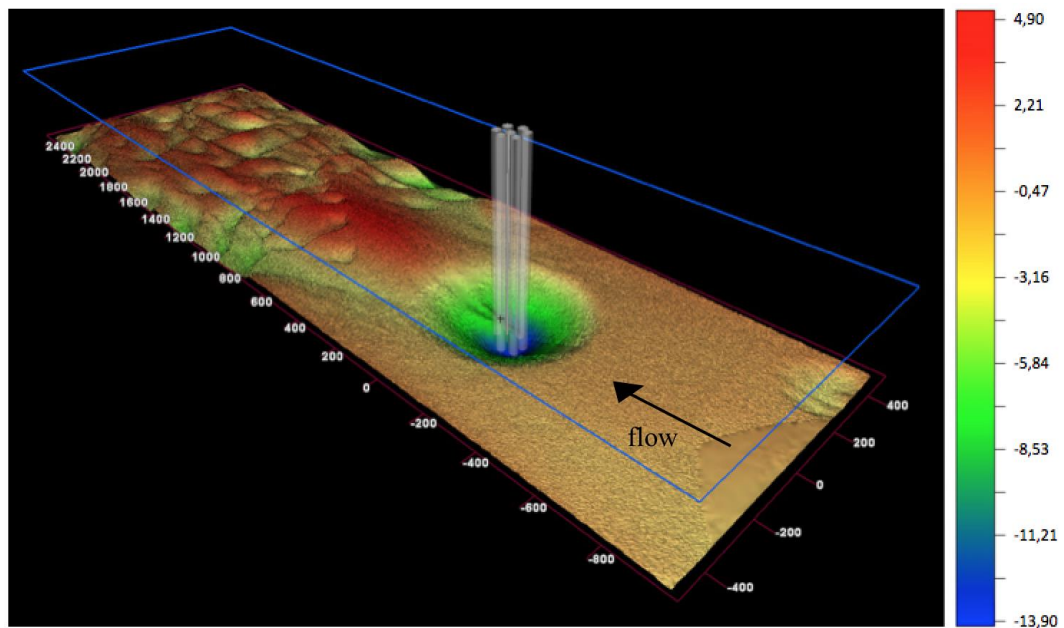


**Figure 3.17 :** Digital model of final bed topography for 12 cm staggered HACC (The dimensions on the figure are in mm and the dimensions on the legend are in cm).

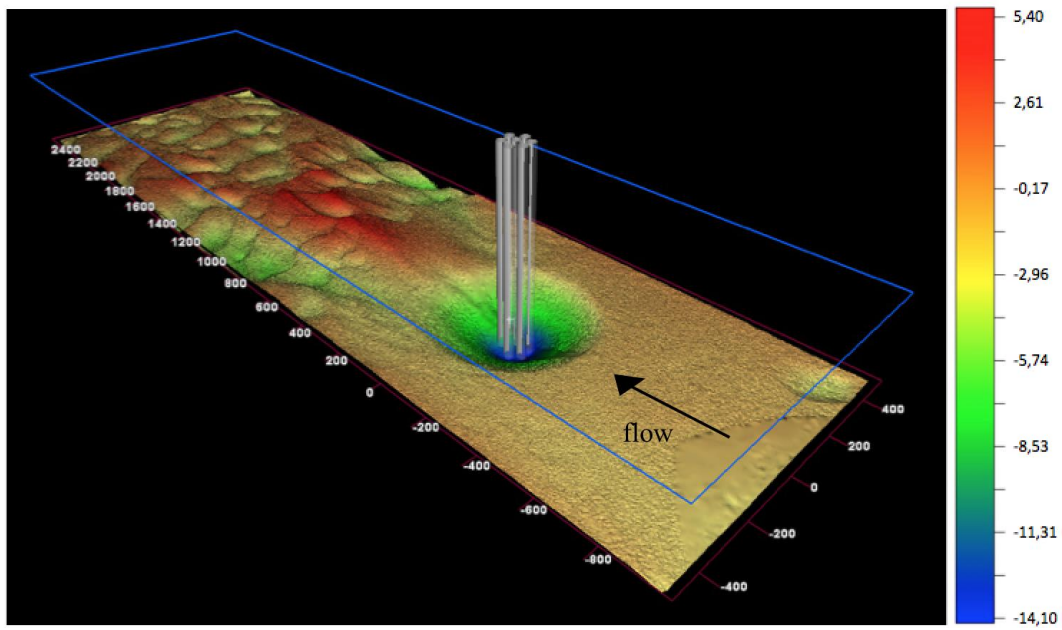


**Figure 3.18 :** Digital model of final bed topography for 12 cm angled HACC (The dimensions on the figure are in mm and the dimensions on the legend are in cm).

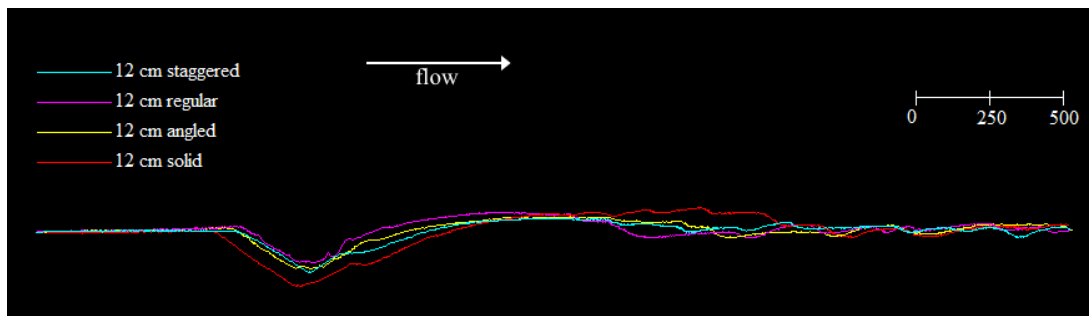


**Figure 3.19 :** Longitudinal view of 12 cm HACC experiments for final bed topography (The dimensions are in mm).

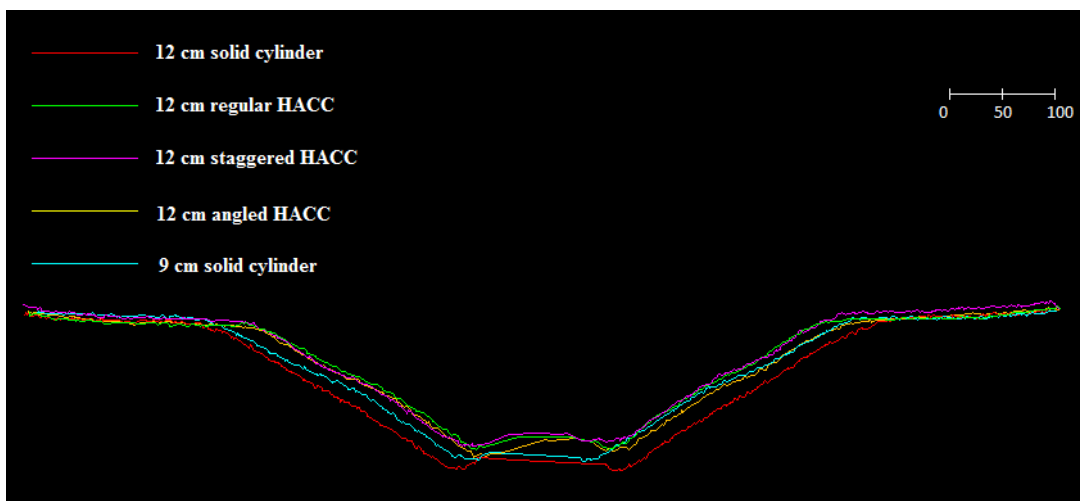


**Figure 3.20 :** Cross-section view of 12 cm HACC experiments for final bed topography (The dimensions are in mm).

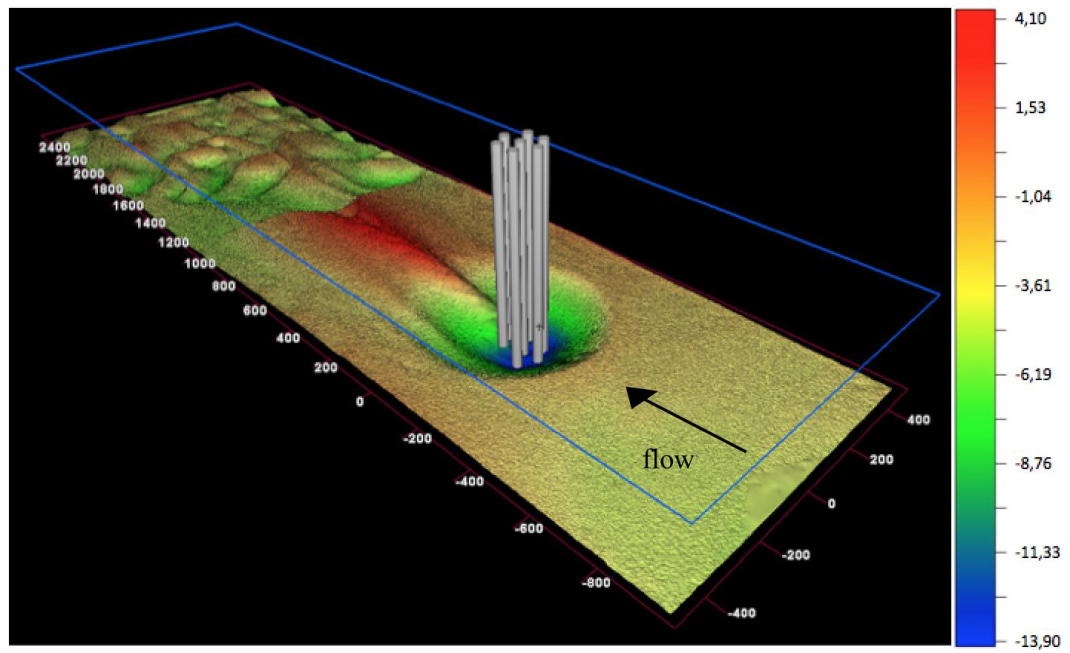


**Figure 3.21 :** Digital model of final bed topography for 16 cm regular HACC (The dimensions on the figure are in mm and the dimensions on the legend are in cm).

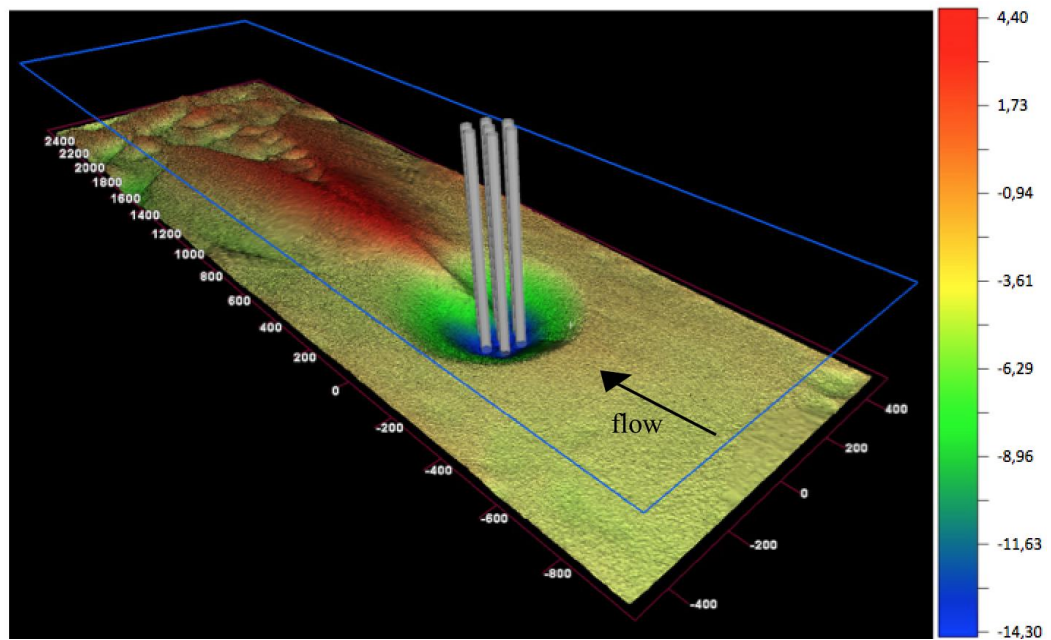


**Figure 3.22 :** Digital model of final bed topography for 16 cm staggered HACC (The dimensions on the figure are in mm and the dimensions on the legend are in cm).

For all the cases of 20 cm HACC, it was observed that ridges are developed at the downstream of the obstacle similar to 16 cm HACC. However, it was noted that for the regular case of 20 cm HACC the ridge was less pronounced. One of the primary differences between 16 cm HACC and 20 cm HACC is that for the case of 20 cm

HACC, ripples were developed on the ridge which was not detected in the case of 16 cm HACC (Figure 3.25- Figure 3.29).

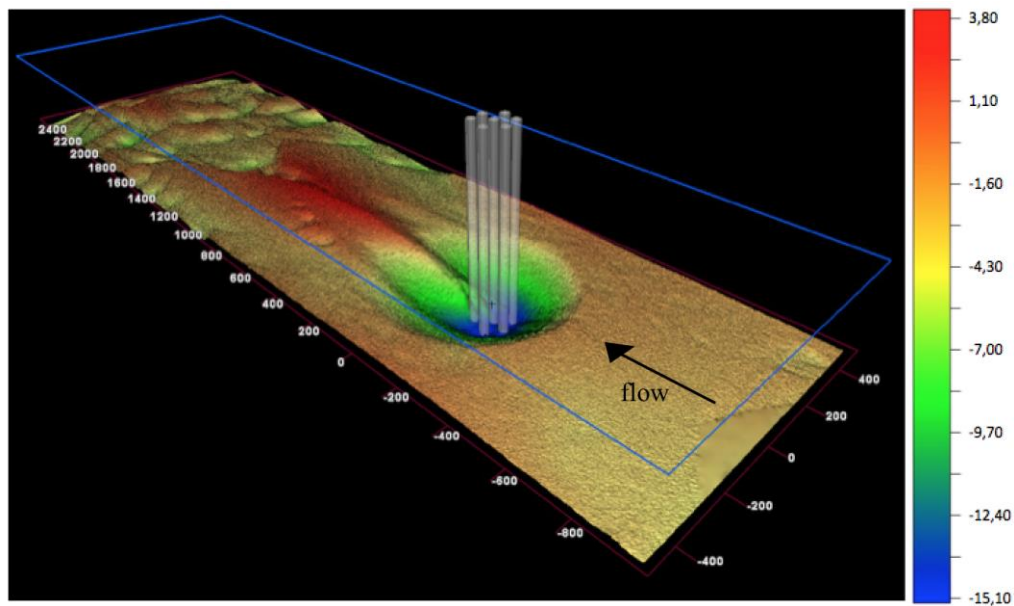


**Figure 3.23 :** Digital model of final bed topography for 16 cm angled HACC (The dimensions on the figure are in mm and the dimensions on the legend are in cm).

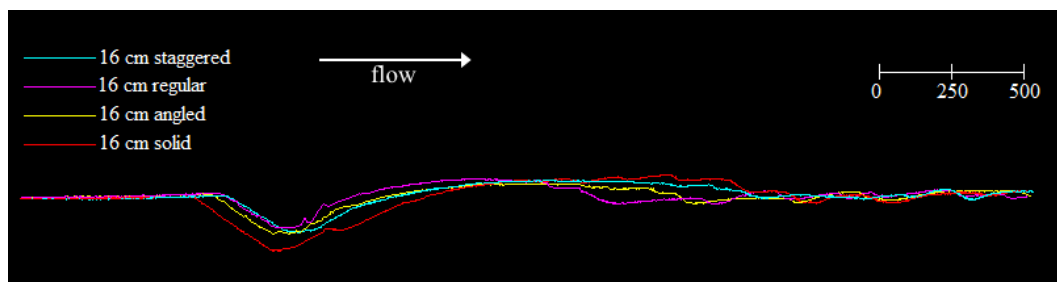


**Figure 3.24 :** Longitudinal view of 16 cm HACC experiments for final bed topography (The dimensions are in mm).

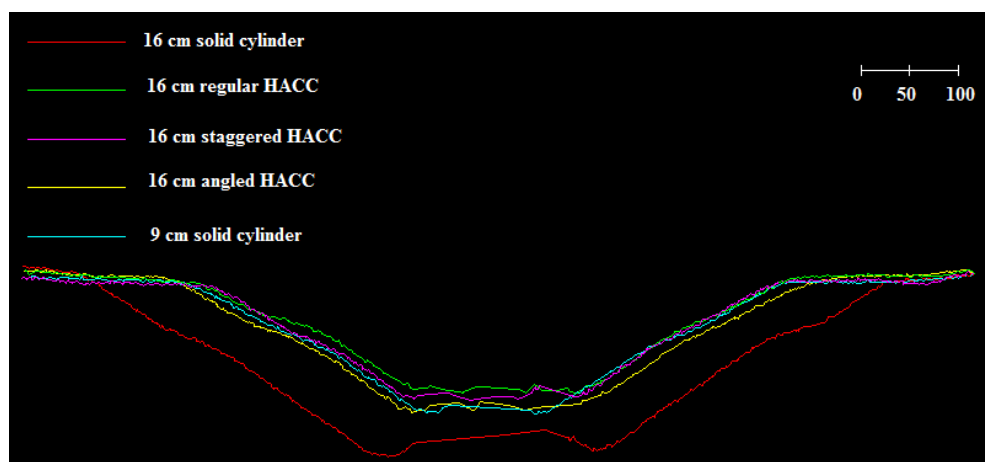


**Figure 3.25 :** Cross-section view of 16 cm HACC experiments for final bed topography (The dimensions are in mm).



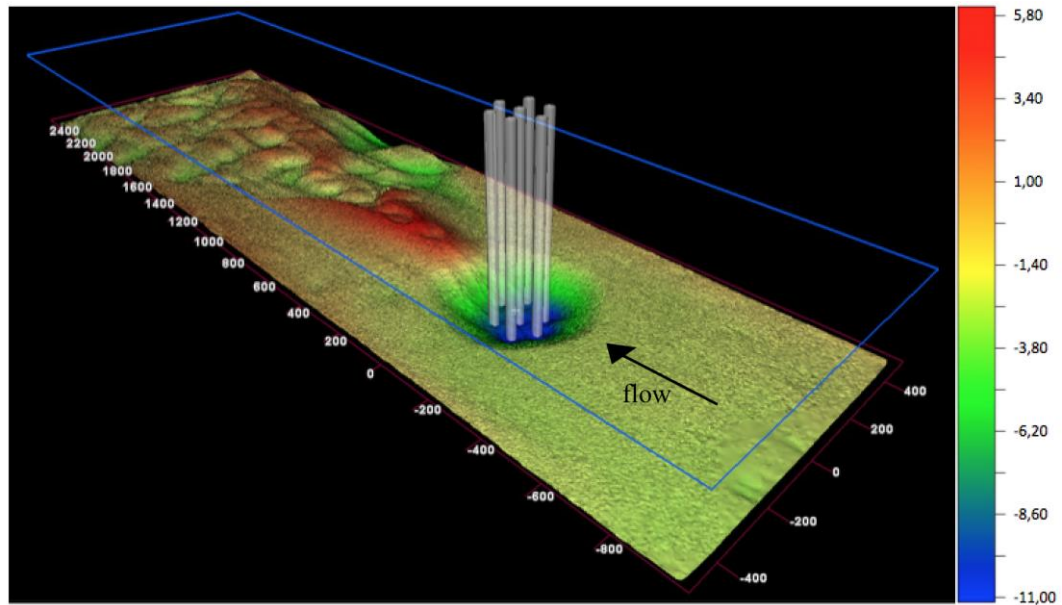


**Figure 3.26 :** Digital model of final bed topography for 20 cm regular HACC (The dimensions on the figure are in mm and the dimensions on the legend are in cm).

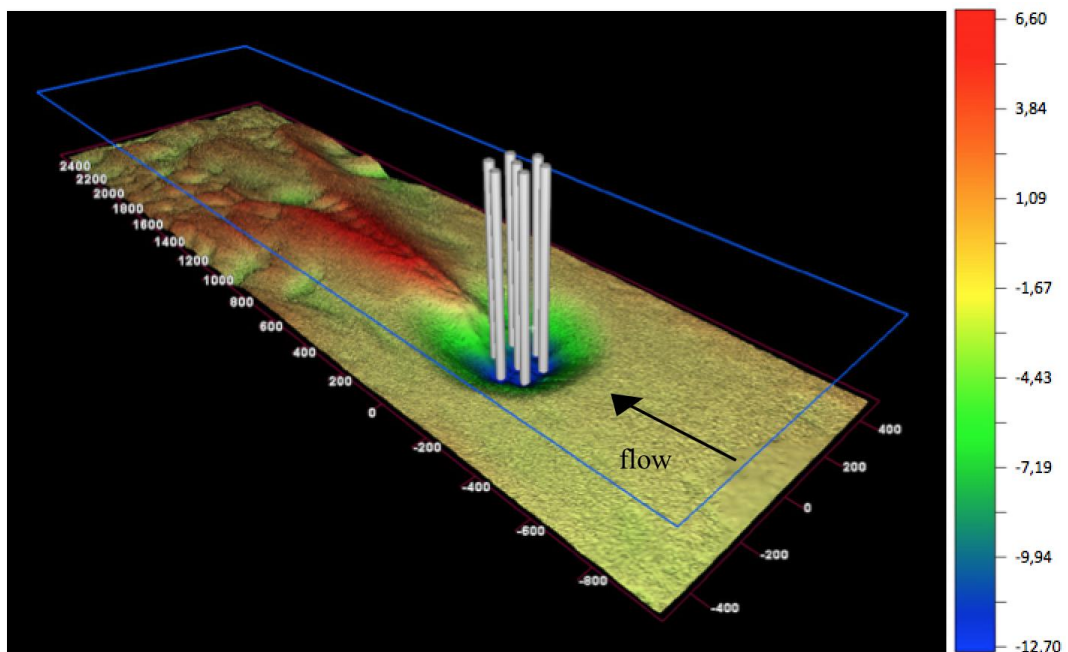


**Figure 3.27 :** Digital model of final bed topography for 20 cm staggered HACC (The dimensions on the figure are in mm and the dimensions on the legend are in cm).

For the cases of 24 cm HACC, both stem scale scour (local scour) and patch scale scour (global scour) were observed (Figure 3.30- Figure 3.34). As observed for 20 cm HACC, development of the ripples on the ridge was detected for 24 cm cases of staggered and angled. During the 24 cm HACC experiments, gradation of the sediments around the individual stems was observed.

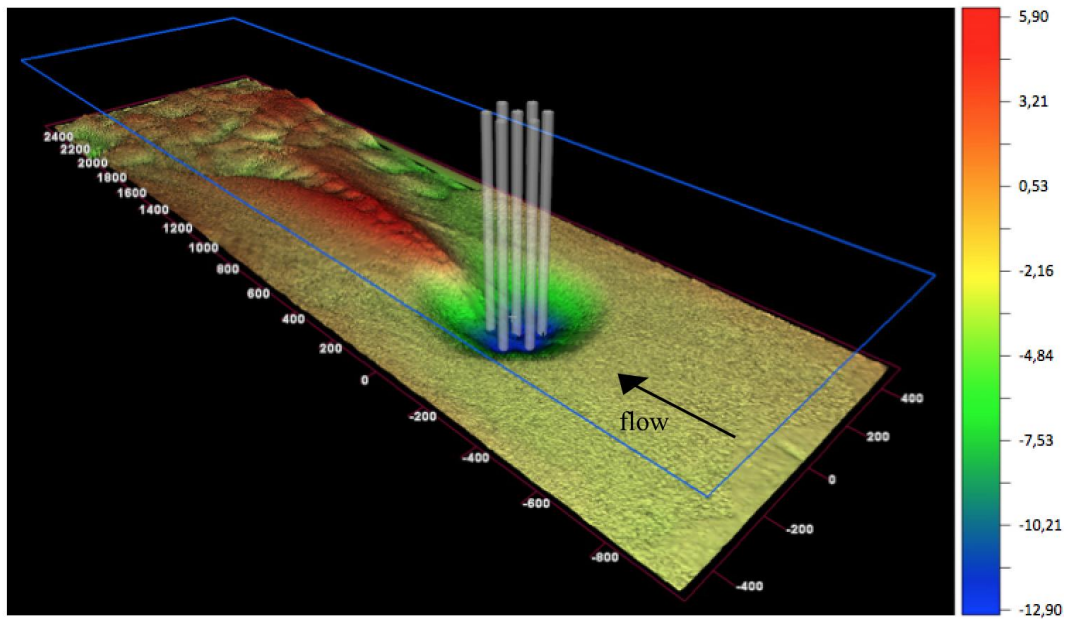


**Figure 3.28 :** Digital model of final bed topography for 20 cm angled HACC (The dimensions on the figure are in mm and the dimensions on the legend are in cm).

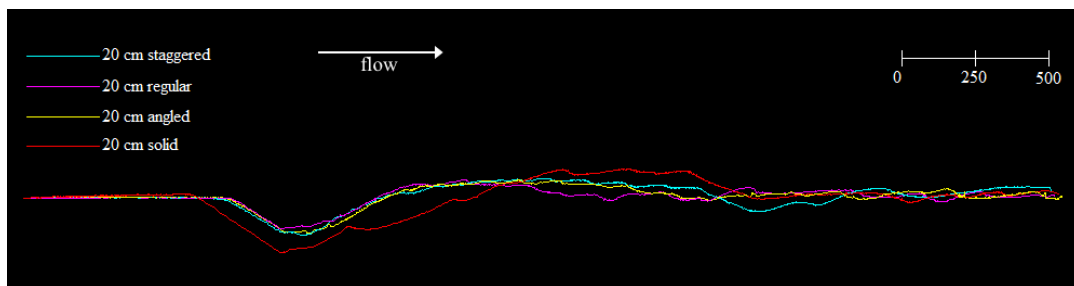


**Figure 3.29 :** Longitudinal view of 20 cm HACC experiments for final bed topography (The dimensions are in mm).

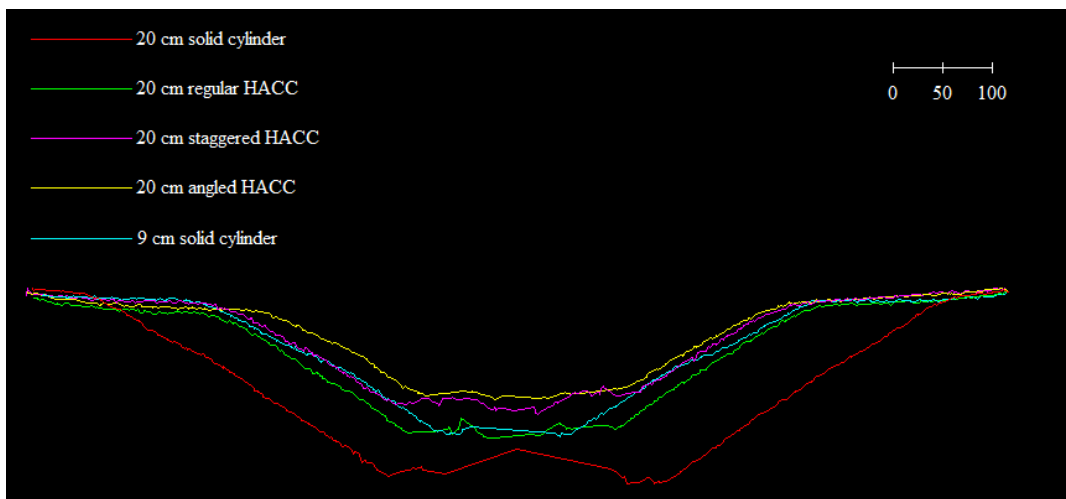


**Figure 3.30 :** Cross-section view of 20 cm HACC experiments for final bed topography (The dimensions are in mm).

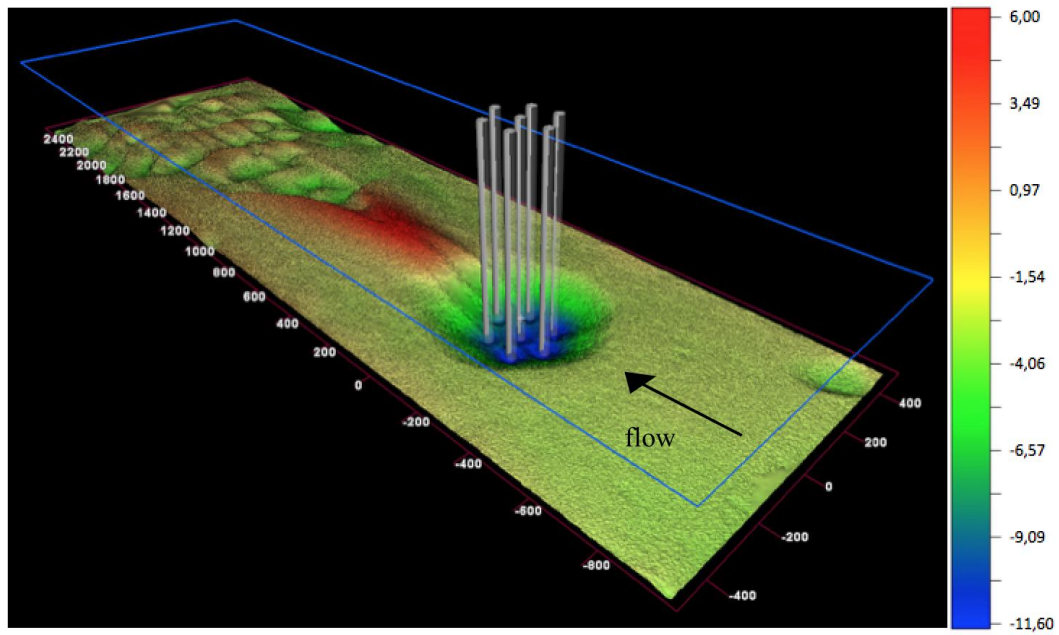


**Figure 3.31 :** Digital model of final bed topography for 24 cm regular HACC (The dimensions on the figure are in mm and the dimensions on the legend are in cm).

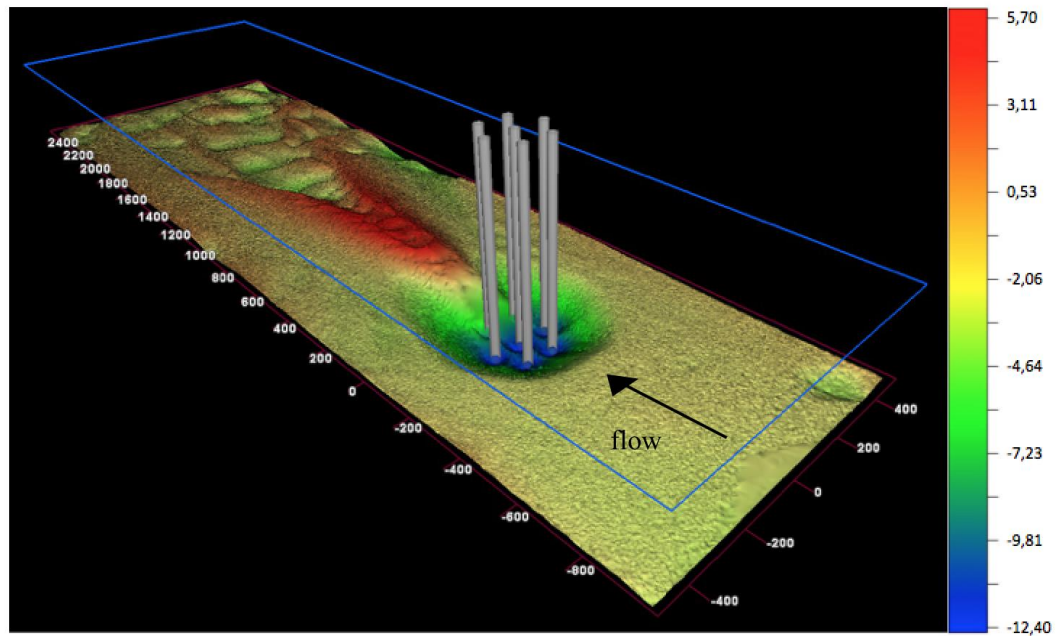


**Figure 3.32 :** Digital model of final bed topography for 24 cm staggered HACC (The dimensions on the figure are in mm and the dimensions on the legend are in cm).

Without any exceptions, as seen in figures above, the upstream slope of the scour hole was always steeper than that of downstream slope. All contour plots are given in Appendix B.

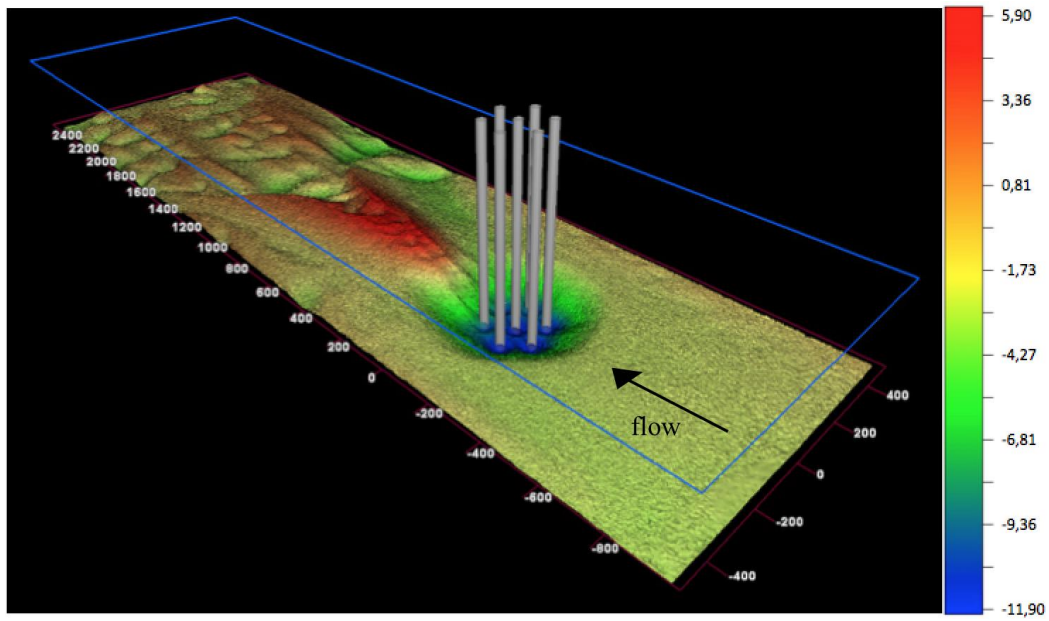


**Figure 3.33 :** Digital model of final bed topography for 24 cm angled HACC (The dimensions on the figure are in mm and the dimensions on the legend are in cm).

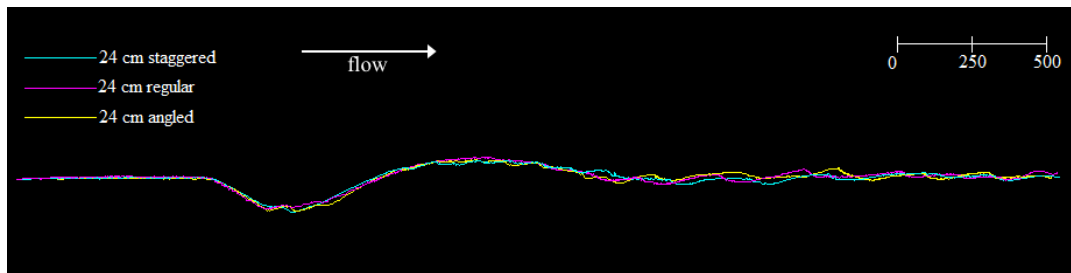


**Figure 3.34 :** Longitudinal view of 24 cm HACC experiments for final bed topography (The dimensions are in mm).

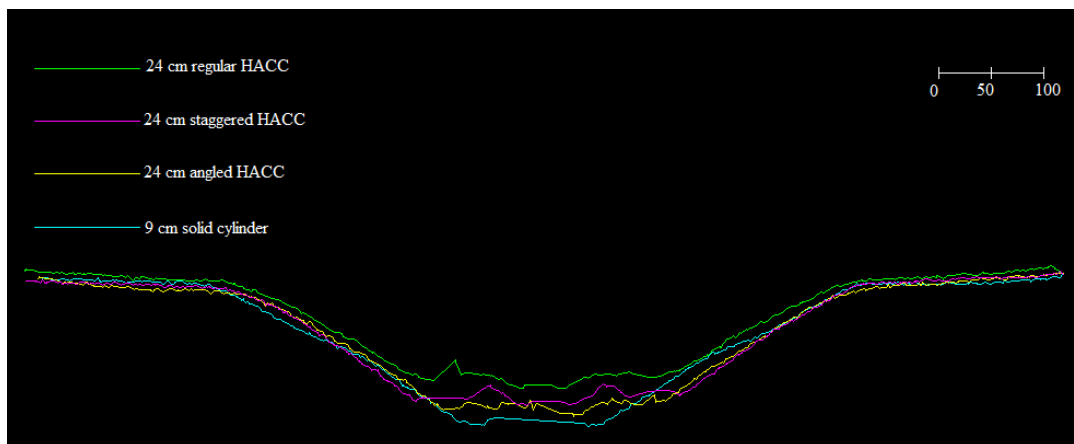


**Figure 3.35 :** Cross-section view of 24 cm HACC experiments for final bed topography (The dimensions are in mm).



### 3.5 The Morphometric Analysis

Based on the data retrieved by laser scanning, some morphological analysis was made. For each experiment the scour width ( $S_w$ ), slope of the scour hole for two directions (upstream slope ( $I_u$ ) and downstream slope ( $I_d$ ), scour depth ( $S_d$ ), maximum elevation of the deposition ( $D_h$ ), scour volume ( $S_v$ ), deposition volume ( $D_v$ ), the distance between the crest of the deposition zone and the edge of the obstacle ( $L_d$ ), scour area ( $S_a$ ) and deposition area ( $D_a$ ), which were deduced from laser scanning, were tabulated in Table 3.2.

**Table 3.2 :** The morphometric parameters for each experiment.

Experiment	$S_w$ (cm)	$I_u$ (%)	$I_d$ (%)	$S_d$ (cm)	$D_h$ (cm)	$S_v$ (m <sup>3</sup> )	$D_v$ (m <sup>3</sup> )	$S_a$ (m <sup>2</sup> )	$D_a$ (m <sup>2</sup> )	$L_d$ (m)
9 cm solid	58.0	-60	35	14.8	4.9	0.0282	0.0167	1.89	1.49	0.69
12 cm solid	64.8	-56	30	14.9	8.2	0.0275	0.0195	1.60	1.82	0.91
16 cm solid	81.2	-62	33	20.0	6.7	0.0497	0.0348	1.80	1.59	1.28
20 cm solid	83.8	-61	25	20.2	9.1	0.0538	0.0372	1.53	1.87	1.03
12 cm regular	52.8	-59	32	13.4	4.3	0.0239	0.0162	1.59	1.83	0.74
12 cm stag.	54.5	-57	27	13.9	4.9	0.0273	0.0174	1.59	1.81	0.92
12 cm angled	56.4	-59	26	14.1	5.4	0.0258	0.0187	1.57	1.85	1.07
16 cm regular	60.7	-63	31	13.9	4.1	0.0268	0.0153	2.21	1.17	0.62
16 cm stag.	58.1	-58	39	14.3	4.4	0.0291	0.0181	1.89	1.51	0.85
16 cm angled	64.7	-63	34	15.1	3.8	0.0306	0.0180	1.88	1.50	0.89
20 cm regular	52.2	-60	49	11.0	5.8	0.0218	0.0141	1.91	1.51	0.53
20 cm stag.	61.9	-49	51	12.7	6.6	0.0255	0.0179	1.65	1.73	0.82
20 cm angled	57.6	-58	52	12.9	5.9	0.0293	0.0166	1.93	1.49	0.76
24 cm regular	58.5	-56	40	11.6	6.0	0.0205	0.0181	1.44	2.00	0.63
24 cm stag.	59.6	-48	35	12.4	5.7	0.0222	0.0180	1.59	1.87	0.72
24 cm angled	57.8	-57	52	11.9	5.9	0.0242	0.0163	1.77	1.64	0.68

In order to express the porosity of a HACC, the packing density parameter ( $\Psi$ ) was utilized. Since there are seven small cylinders in every HACC, the packing density was calculated by using the formula:

$$\Psi = 7d^2/D^2 \quad (3.2)$$

where  $d$  represents the diameter of the small cylinders and  $D$  represents the diameter of the circumambient circle. The packing density is constant for each circumambient diameter and it decreases when the diameter increases. Projected area is the summation of the area bounded by the outer edges of the small cylinders, which is perpendicular to the flow direction. Blockage ratio is the ratio of projected area to the area of the circumambient cylinder, which is perpendicular to the flow direction.

Both projected area and blockage ratio change with the circumambient diameter and angle of the flow. In Table 3.3 the packing densities, the projected areas and the blockage ratios for all the experiments are shown. The packing density parameter was compared to scour depth for all the HACC cases and shown in Figure 3.35. Since the packing density is inversely proportional with circumambient diameter, the diameter decreases along the x-axis of the graph. This comparison shows that from 24 cm to 16 cm, scour depth increases while packing density increases and the circumambient diameter decreases. Somewhere between 12 cm and 16 cm, when packing density is around 0.4, this pattern changes. The same pattern can be seen in Figure 3.36, which gives the relationship between packing density and scour volume. The reason behind these patterns may be the behavior of HACCs with smaller circumambient diameter is more like solid cylinders. Bleed flow can be strong enough to decrease the scour in 20 cm and 24 cm cases, but may not be strong enough for the 12 and 16 cm cases. In future, in order to interpret the full mechanism behind the occurrence of this pattern, in depth velocity measurements are recommended.

**Table 3.3 :** Packing densities belonging to the different configurations of HACCs.

D (cm)	Orientation	$\Psi$	Blockage Ratio	Projected Area (cm <sup>2</sup> )
<b>12</b>	<b>regular</b>	<b>0.5619</b>	<b>0.940</b>	<b>316.20</b>
<b>12</b>	<b>staggered</b>	<b>0.5619</b>	<b>1.000</b>	<b>372.00</b>
<b>12</b>	<b>angled</b>	<b>0.5619</b>	<b>1.000</b>	<b>362.92</b>
16	regular	0.3161	0.712	316.20
16	staggered	0.3161	1.000	496.00
16	angled	0.3161	1.000	482.70
<b>20</b>	<b>regular</b>	<b>0.2023</b>	<b>0.574</b>	<b>316.20</b>
<b>20</b>	<b>staggered</b>	<b>0.2023</b>	<b>0.850</b>	<b>527.00</b>
<b>20</b>	<b>angled</b>	<b>0.2023</b>	<b>0.967</b>	<b>582.55</b>
24	regular	0.1405	0.480	316.20
24	staggered	0.1405	0.708	527.00
24	angled	0.1405	0.895	643.19

For all HACC cases, the distance between the crest of the deposition zone and the edge of the obstacle ( $L_d$ ), which was represented as deposition length in Figure 3.37, increases with increasing packing density. For the same circumambient circle diameter, for all diameters, the regular orientations give the shortest deposition length as can be seen in Figure 3.37.

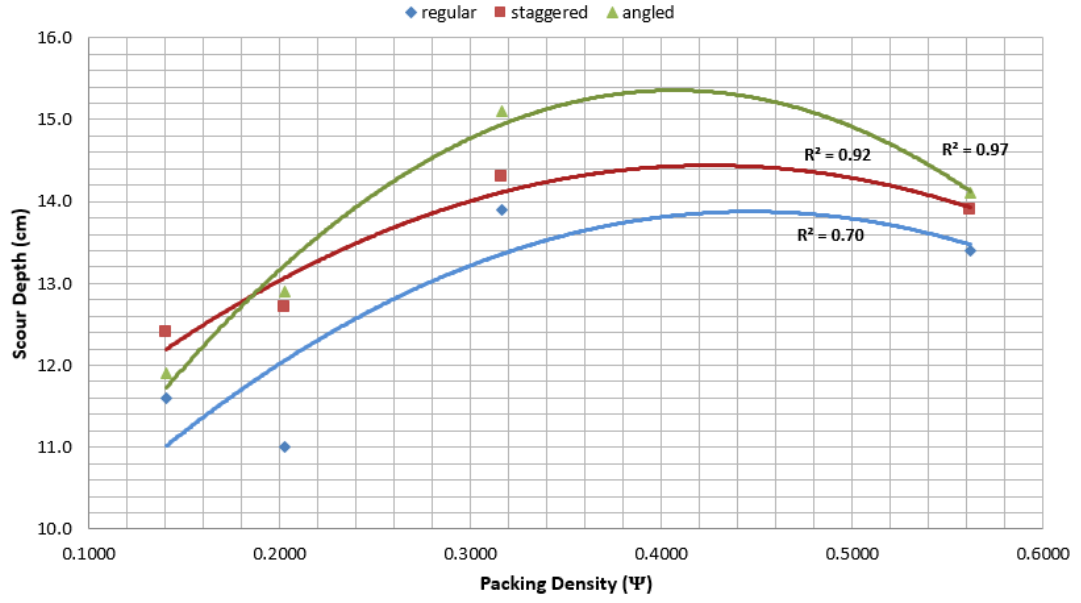


**Figure 3.36 :** The variation of packing density with respect to scour depth for different HACC cases

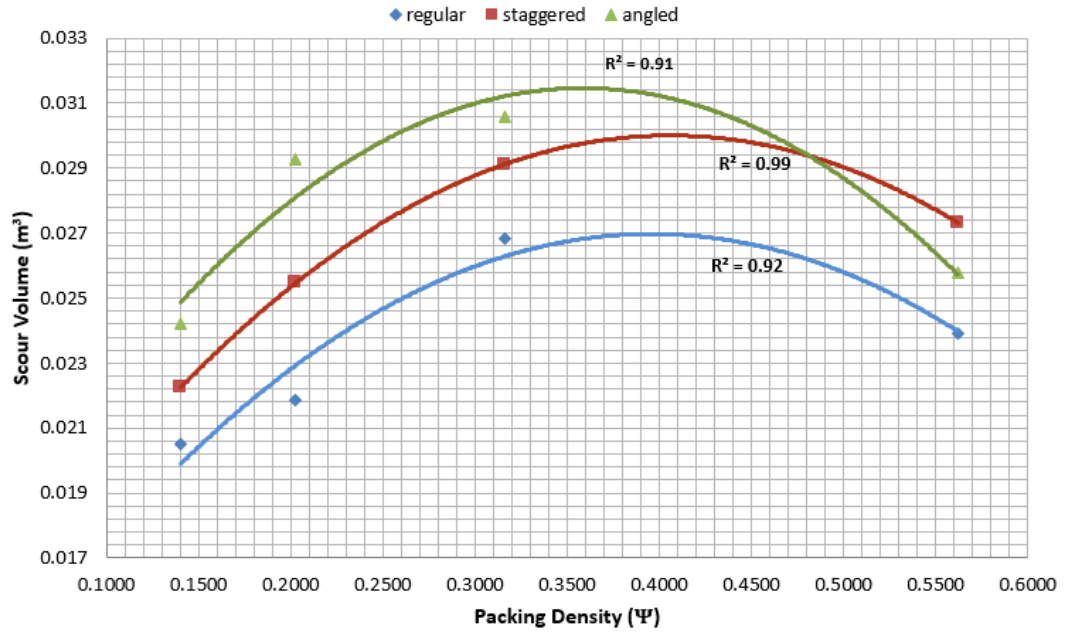


**Figure 3.37 :** The variation of packing density with respect to scour volume for different HACC cases

For solid cylinder cases, in order to see the relationship between the cylinder diameter and the scour characteristics two graphs were drawn (Figure 3.38 and Figure 3.39).  $\Omega_v$  is dimensionless scour depth in terms of volume and can be formulated as:

$$\Omega_v = S_d / \sqrt[3]{S_v} \quad (3.3)$$

$\Omega_a$  is dimensionless scour depth in terms of area and can be formulated as:

$$\Omega_a = S_a / \sqrt[2]{S_a} \quad (3.4)$$

According to Figure 3.38, as the diameter of solid cylinder increases, scour depth increases more than the scour volume. The same relationship between scour depth and scour area was seen from Figure 3.39.

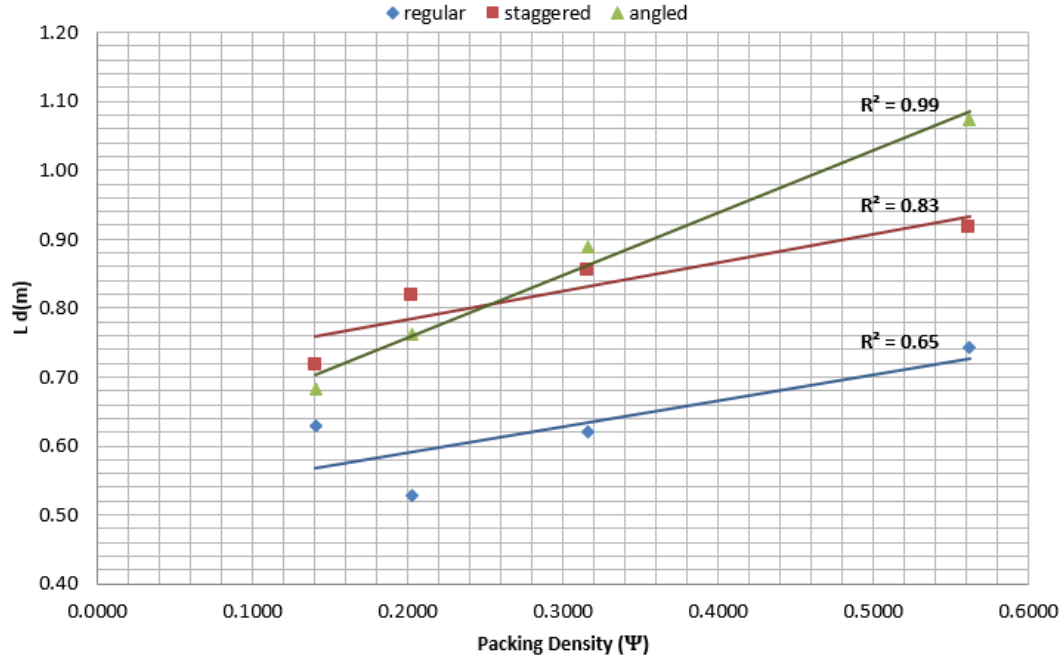


**Figure 3.38 :** The variation of packing density with respect to deposition length for different HACC cases

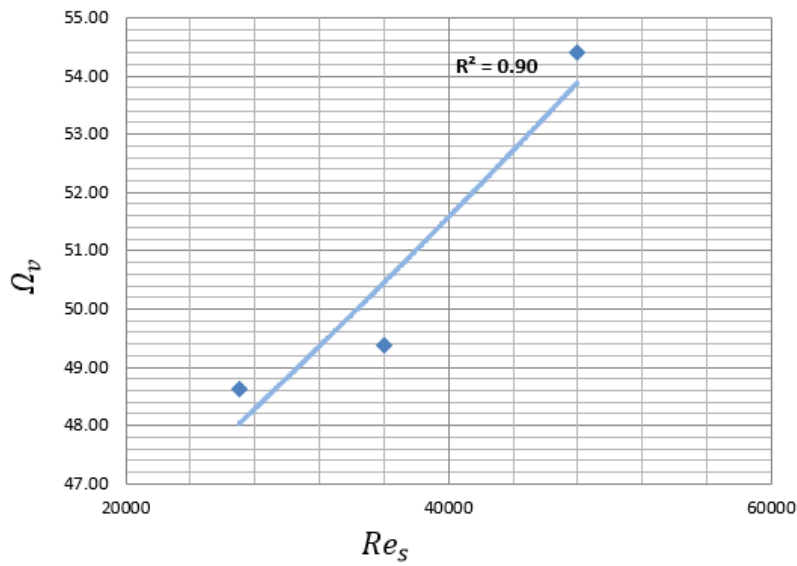


**Figure 3.39 :** The variation of dimensionless scour depth in terms of volume with respect to stem Reynolds number.

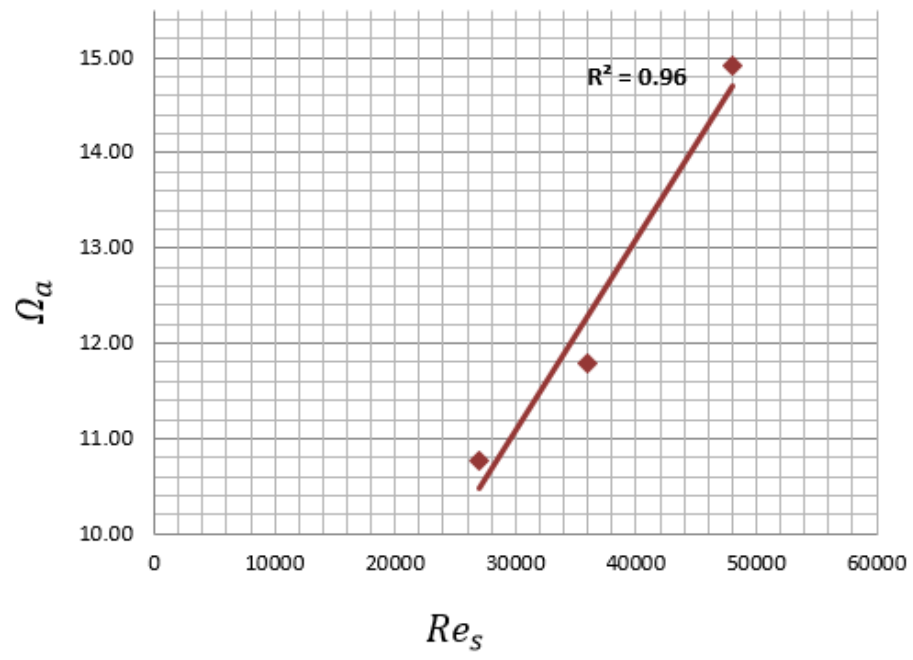


**Figure 3.40 :** The variation of dimensionless scour depth in terms of area with respect to stem Reynolds number.



#### 4. CONCLUSIONS AND RECOMMENDATIONS

As essential parts of transportation, bridges must be designed by considering both the structural and the hydraulic and fluvial perspectives because they cause significant changes in the flow around the piers. When a bridge pier is placed in a river, the changes in the flow cause scour around the bridge pier and lead to instability of the structure. In order to reduce the scour, the idea of designing a porous bridge pier was investigated in this study.

A porous bridge pier may have these possible advantages:

1. Due to the porous form of the model, local shear stress around the pier would decrease and correspondingly the local scour would decrease.
2. Porosity allows water to pass through the pier. Therefore a porous pier would block less the river flow, and the back water at the upstream of the bridge would be diminished.
3. Different from the other countermeasures against bridge pier scour in the literature, a hexagonally arrayed seven cylinder group, which has the same cross sectional area with a solid cylinder, can be more practical in terms of application since seven small cylinders are easier to penetrate the river bed compared to single counterpart.
4. There would be no need to use another countermeasure to decrease the scour if a porous pier is used. This leads to decrease in costs.

The results showed that a porous bridge pier model causes a reduction on scour depth, indeed. The findings of the present study are summarized in the following:

- In all the HACC cases, the scour depth was less than 9 cm solid cylinder at the point where Vectrino II was placed.
- For regular orientation, the highest scour depth value was seen for 12 cm regular HACC. While 24 cm regular HACC causes more scour than 20 cm regular HACC, it causes less scour than 12 and 16 cm regular HACCs. For staggered orientations, as the diameter increases, the scour depth decreases. Therefore, the deepest scour at the point where Vectrino II was placed was caused by the 12 cm staggered HACC. In angled cases of HACC, differing from the other orientations, the deepest scour was caused by 16 cm angled HACC which was followed by 12 cm, 20 cm and 24 cm, respectively.

- The best efficiency in terms of scour reduction belongs to the 20 cm staggered HACC. It was followed by 24 cm regular HACC with 22% and 24 cm angled HACC with 20%. 24 cm regular HACC caused 22% of scour reduction while the scour volume reduction for this orientation was 27%. The only HACC that caused more scour than 9 cm solid cylinder was the 16 cm angled HACC with -2%.
- In all the experiments, the changes in the velocities were quite similar. Streamwise velocity increases with increasing scour depth. For lateral velocity, no significant change was observed. Vertical velocity increases with time. The changes in streamwise velocity and vertical velocity were mostly in the first 10 minutes of the experiments.
- 12 cm HACC does not generate distinguishable ridge at the downstream of the obstacle as it behaves like a solid cylinder. Ripple developments which cover the entire cross-section were observed for all cases of 12 cm HACC.
- For 16 cm HACC cases, it was observed that no matter what the arrangement of the HACC is, a distinguishable ridge was observed for all cases.
- For all cases of 20 cm HACC, it was observed that ridges are developed at the downstream of the obstacle similar to 16 cm HACC.
- One of the primary differences between 16 cm HACC and 20 cm HACC is that for the case of 20 cm HACC, ripple developments observed on the ridge which was not detected in the case of 16 cm HACC.
- For the cases of 24 cm HACC, both stem scale scours (local scour) and patch scale scours (global scour) were observed. During the 24 cm HACC experiments, gradation of the sediments around the individual stems was observed.
- Without any exceptions, the upstream slope of the scour hole was always steeper than that of downstream slope.
- For 24 cm, 20 cm and 16 cm HACC cases, scour depth increases while packing density increases and the circumambient diameter decreases. Somewhere between 12 cm and 16 cm, when packing density is around 0.4,



this pattern changes. In order to interpret the full mechanism behind the occurrence of this pattern, in depth velocity measurements are recommended.

- For all HACC cases, the distance between the crest of the deposition zone and the edge of the obstacle, increases with increasing packing density. For the same circumambient circle diameter, for all diameters, the regular orientations give the shortest deposition length.
- For solid cylinder cases, as the diameter of solid cylinder increases, scour depth increases more than the scour volume. The relationship is the same between scour depth and scour area.



## REFERENCES

- Ataie-Ashtiani B. Beheshti, A. (2006).** Experimental Investigation of Clear-Water Local Scour at Pile Groups. *J. Hydraul. Eng.*, 132(10), 1100-1104, doi:10.1061/ASCE0733-94292006
- Chen, Z., Ortiz, A., Zong, L., Nepf, H. (2012).** The wake structure behind a porous obstruction and its implications for deposition near a finite patch of emergent vegetation. *Water Resources Research*, 48, 1-12, doi:10.1029/2012WR012224.
- Chiew, Y. M. (1984).** *Local Scour at Bridge Piers* ( doctoral thesis), Auckland Universty, Departmant of Civil Engineering, Auckland.
- Fredsoe, J., Deingard, R. (1994).** Advanced Series on Ocean Engineering. In L. Philip, F. Lu, (Eds.), *Mechanics of Coastal Sediment Transport*, (2nd. ed., Vol.3, Singapore: World Scientific.
- Hamilton, L. (1994)** Bridge Hydraulics, How to evaluate and combat scour, New York: E & FN Spon.
- Nohani, E., Bahadoribirgani, B., Hajishara, R. (2015).** Evaluation and Comparision of Collar and Collar with Slot Methods In Reducing Local Scour of Cylindrical Bridge Piers. *Applied Resrach Journal*, 1(5), 348-353.
- Nortek AS. (2004).** **Vectrino User Guide. Norway.**  
Nortek Scientific Acoustic Development Group Inc. (no date). Vectrino II User Guide. Canada.
- Sumer, B., Bundgaard, K., Fredsoe, J. (2005),** Global and Local Scour at Pile Groups, *International Journal of Offshore and Polar Engineering*, 15(3), 204-209.
- Sumer, B. M. and Fredsoe, J. (1994).** Advanced Series on Ocean Engineering. In L. Philip, F. Lu, (Eds.), *The Mechanics of Scour in the Marine Environment*, (2nd. ed., Vol.3, Singapore: World Scientific.
- Sumer, B. M. and Fredsoe, J. (2002).** The Mechanics of Scour In The Marine Environment. World Scientific.
- Sumer, B. M., Unsal, I., Bayazit, M. (1982).** Hidrolik. Birsen Yayınevi.
- Tafarojnoruz, A., Gaudio, R., Calomino, F. (2012).** Evaluation of Flow-Altering Countermeasures against Bridge Pier Scour. *J. Hydraul. Eng.*, 138, 297-305. DOI: 10.1061/(ASCE)HY.1943-7900.0000512.

**Takemura, T., , Tanaka, N. (2007).** Flow structures and drag characteristics of a colony-type emergent roughness model mounted on a flat plate in uniform flow. *Fluid Dynamics Research*, 39, 694–710. doi:10.1016/j.fluidyn.2007.06.001.

**Yagci, O., Kitsikoudis, V., Celik M.F., Hodoglu, C., Kirca, V.Ş.Ö., Valyrakis, M., Duran, Z., Kaya, S. (2015).** The variation of local scour pattern around representative natural vegetation elements. The 36th *IAHR World Congress*, 28 June – 3 July, 2015, The Hague, The Netherlands.

**Zong, L., Nepf, H. (2010).** Flow and deposition in and around a finite patch of vegetation. *Geomorphology*, 116, 363–372, doi:10.1016/j.geomorph.2009.11.020.

**Zong, L., Nepf, H. (2010).** Flow and deposition in and around a finite patch of vegetation. *Geomorphology*, 116, 363–372.

**Zong, L., Nepf, H. (2011).** Vortex development behind a finite porous obstruction in a channel. *J. Fluid Mech.* 1-24, doi:10.1017/jfm.2011.479.

## **APPENDICES**

**APPENDIX A:** Velocity graphs for each experiment for 8 hours and 30 minutes

**APPENDIX B:** Counterlines for the final bed topography for each experiment



## APPENDIX A

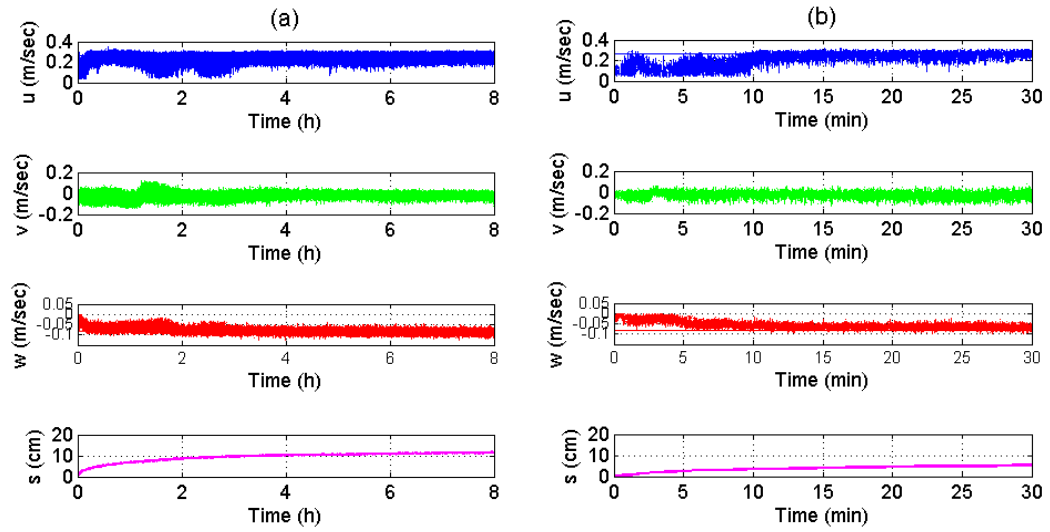


**Figure A.1 :** (a) The change in the velocities and the scour depth over time for 9 cm solid cylinder experiment for 8 hours.(b) The change in the velocities and the scour depth over time for 9 cm solid cylinder experiment for 30 minutes.

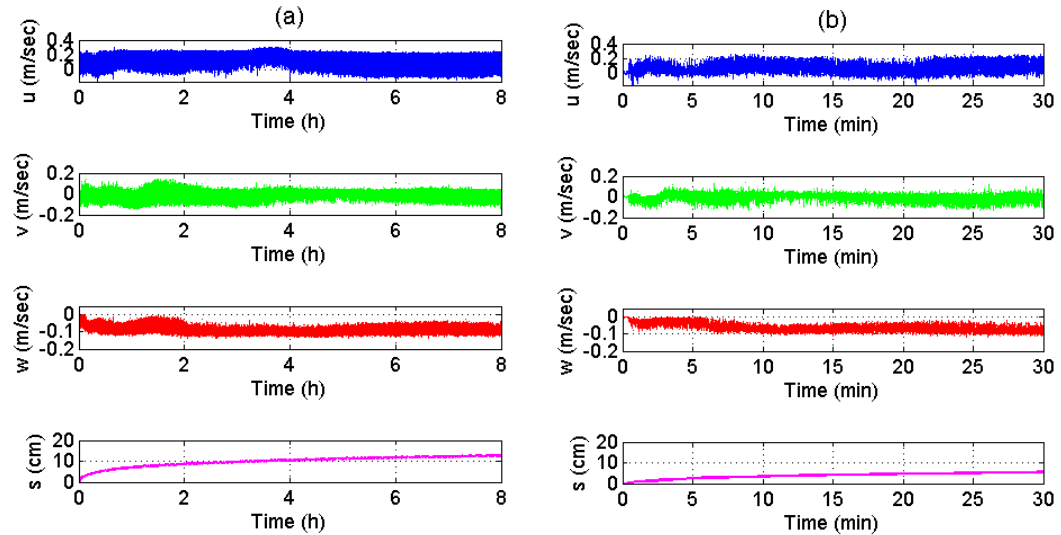


**Figure A.2 :** (a) The change in the velocities and the scour depth over time for 12 cm solid cylinder experiment for 8 hours.(b) The change in the velocities and the scour depth over time for 12 cm solid cylinder experiment for 30 minutes.

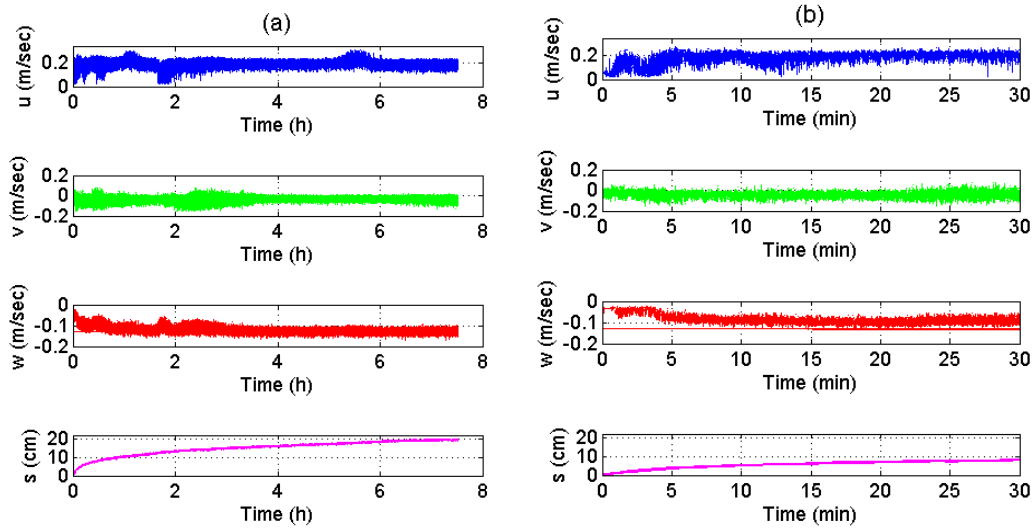


**Figure A.3 :** (a) The change in the velocities and the scour depth over time for 16 cm solid cylinder experiment for 8 hours.(b) The change in the velocities and the scour depth over time for 16 cm solid cylinder experiment for 30 minutes.

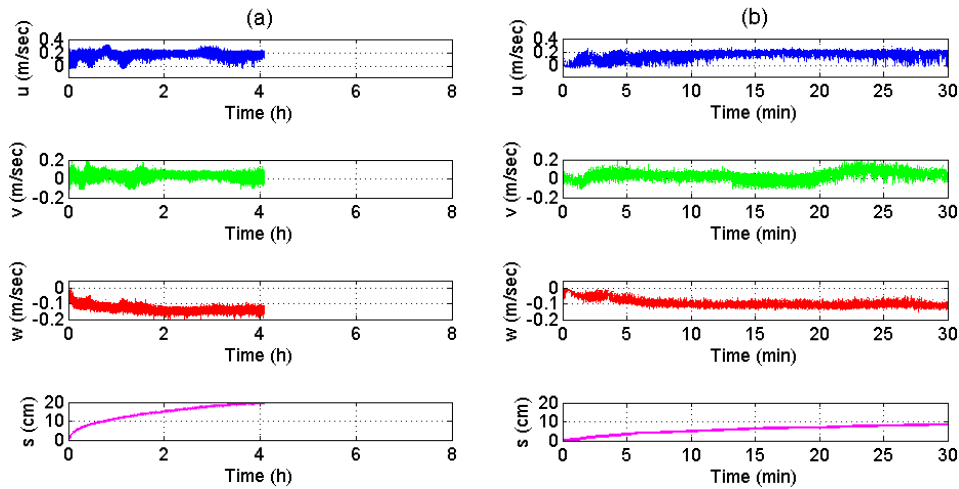


**Figure A.4 :** (a) The change in the velocities and the scour depth over time for 20 cm solid cylinder experiment for 8 hours.(b) The change in the velocities and the scour depth over time for 20 cm solid cylinder experiment for 30 minutes.



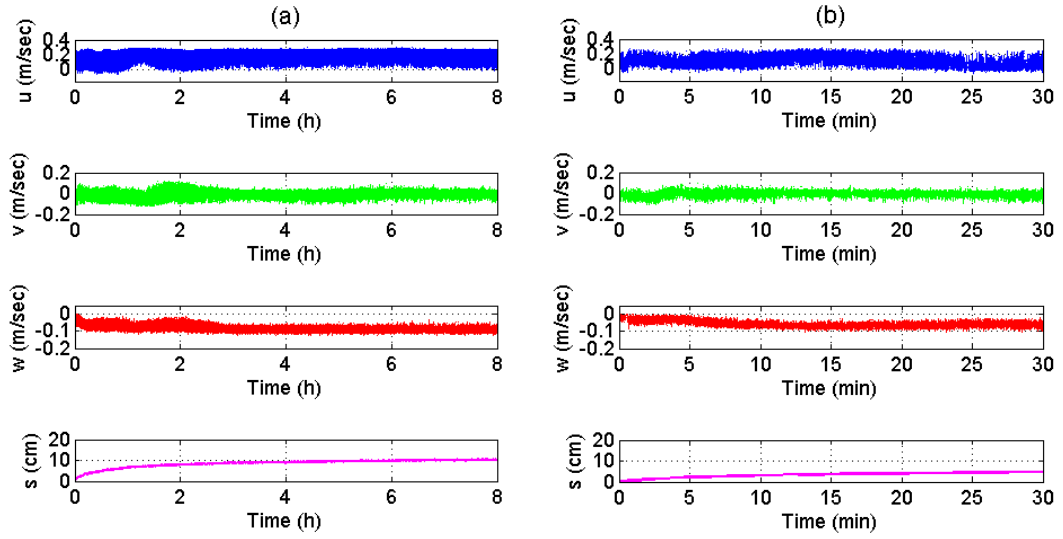


**Figure A.5 :** (a) The change in the velocities and the scour depth over time for 12 cm regular HACC experiment for 8 hours.(b) The change in the velocities and the scour depth over time for 12 cm regular HACC experiment for 30 minutes.

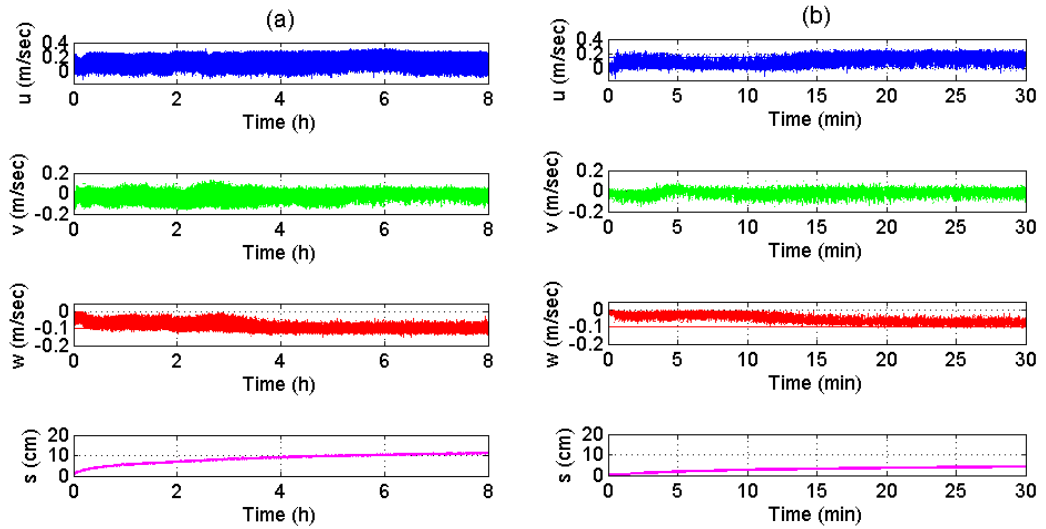


**Figure A.6 :** (a) The change in the velocities and the scour depth over time for 12 cm staggered HACC experiment for 8 hours.(b) The change in the velocities and the scour depth over time for 12 cm staggered HACC experiment for 30 minutes.

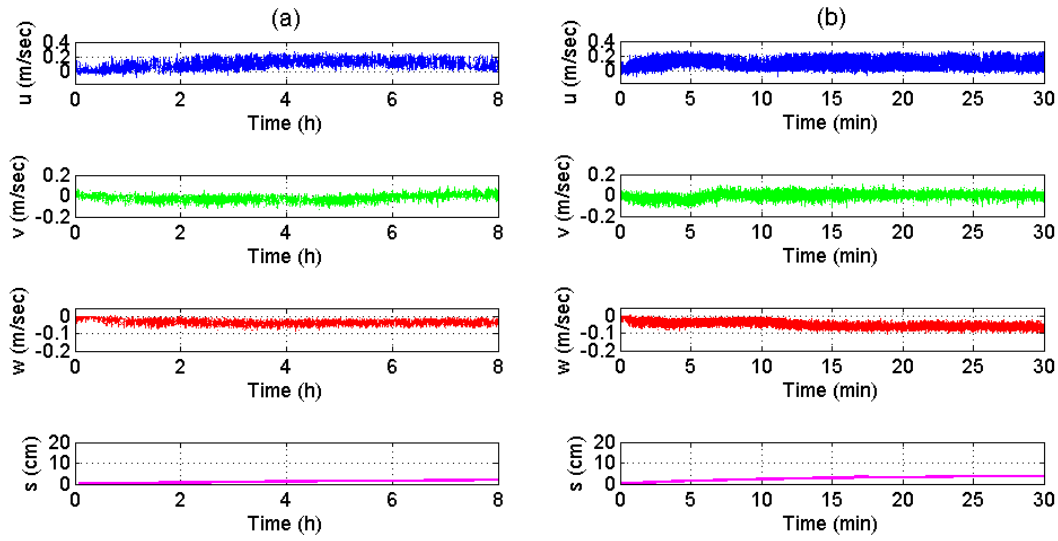


**Figure A.7 :** (a) The change in the velocities and the scour depth over time for 12 cm angled HACC experiment for 8 hours.(b) The change in the velocities and the scour depth over time for 12 cm angled HACC experiment for 30 minutes.

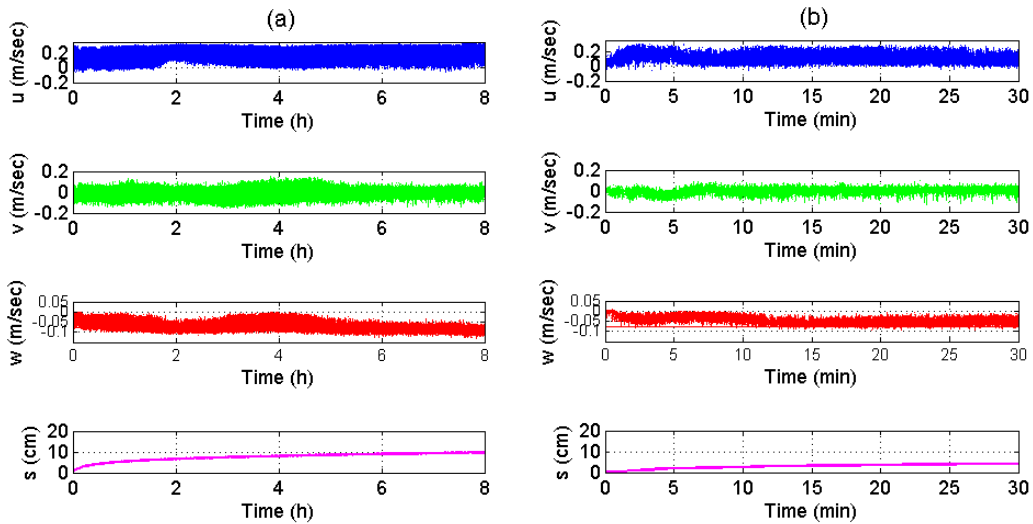


**Figure A.8 :** (a) The change in the velocities and the scour depth over time for 16 cm regular HACC experiment for 8 hours.(b) The change in the velocities and the scour depth over time for 16 cm regular HACC experiment for 30 minutes.

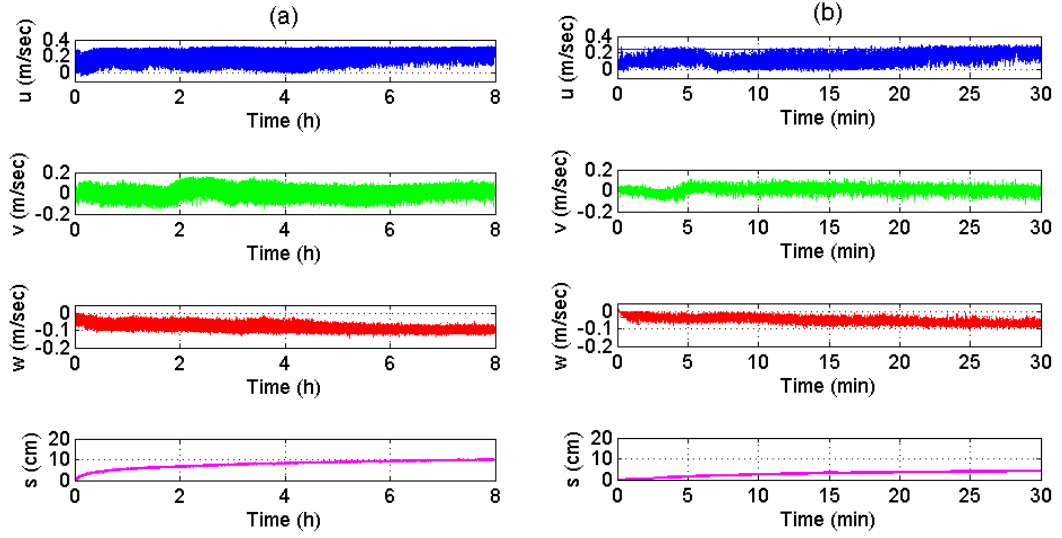


**Figure A.9 :** (a) The change in the velocities and the scour depth over time for 16 cm staggered HACC experiment for 8 hours.(b) The change in the velocities and the scour depth over time for 16 cm staggered HACC experiment for 30 minutes.

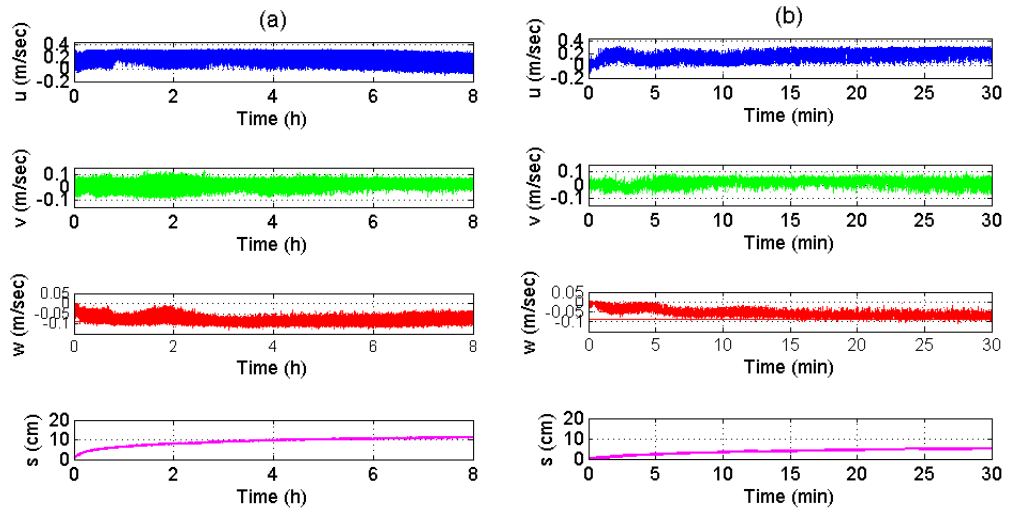


**Figure A.10 :** (a) The change in the velocities and the scour depth over time for 16 cm angled HACC experiment for 8 hours.(b) The change in the velocities and the scour depth over time for 16 cm angled HACC experiment for 30 minutes.

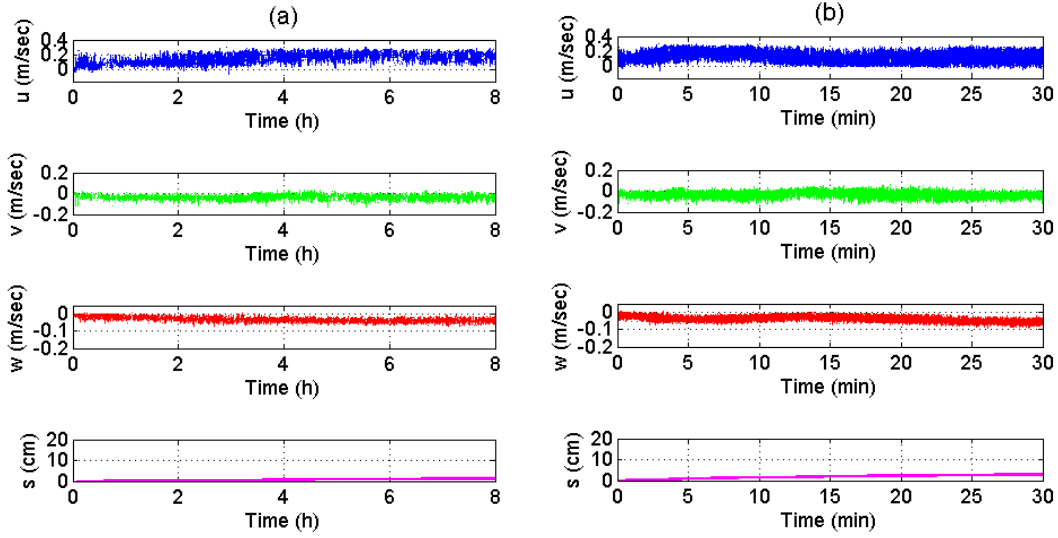


**Figure A.11 :** (a) The change in the velocities and the scour depth over time for 20 cm regular HACC experiment for 8 hours.(b) The change in the velocities and the scour depth over time for 20 cm regular HACC experiment for 30 minutes.

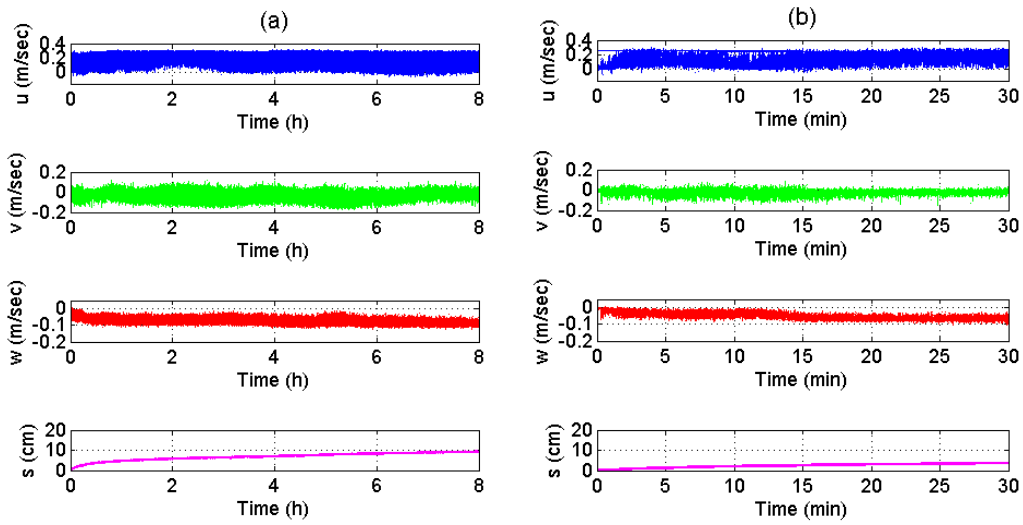


**Figure A.12 :** (a) The change in the velocities and the scour depth over time for 20 cm staggered HACC experiment for 8 hours.(b) The change in the velocities and the scour depth over time for 20 cm staggered HACC experiment for 30 minutes.

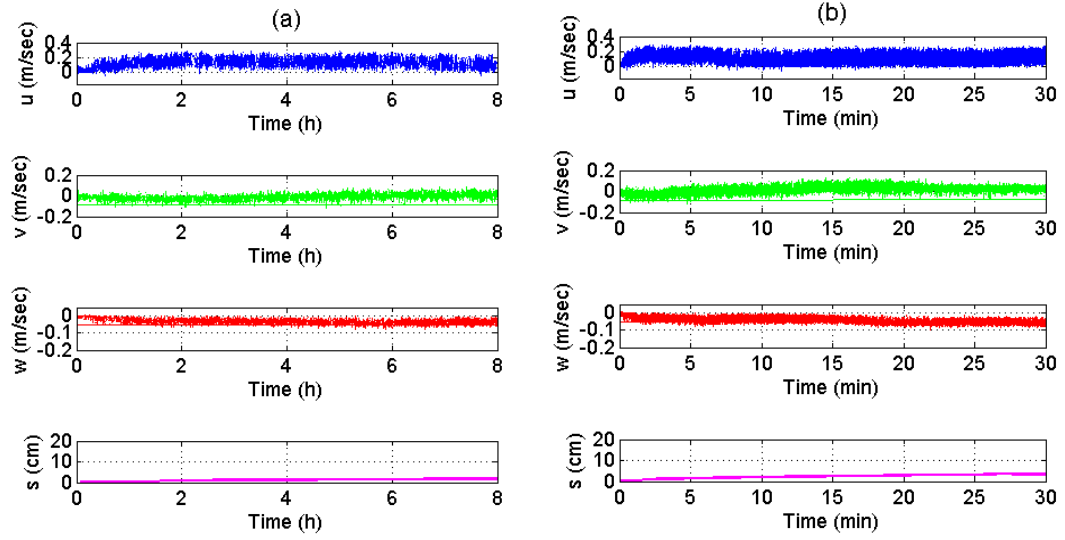


**Figure A.13 :** (a) The change in the velocities and the scour depth over time for 20 cm angled HACC experiment for 8 hours.(b) The change in the velocities and the scour depth over time for 20 cm angled HACC experiment for 30 minutes.

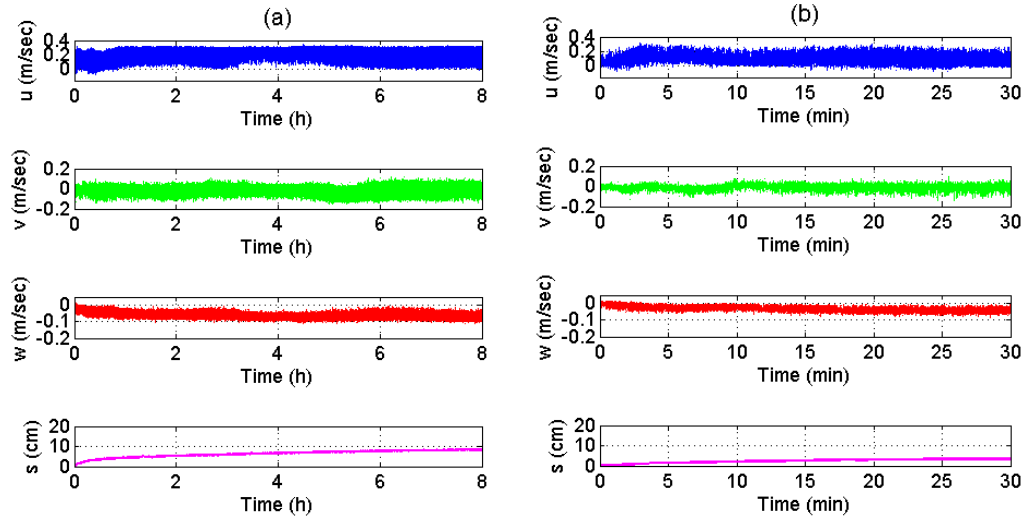


**Figure A.14 :** (a) The change in the velocities and the scour depth over time for 24 cm regular HACC experiment for 8 hours.(b) The change in the velocities and the scour depth over time for 24 cm regular HACC experiment for 30 minutes.

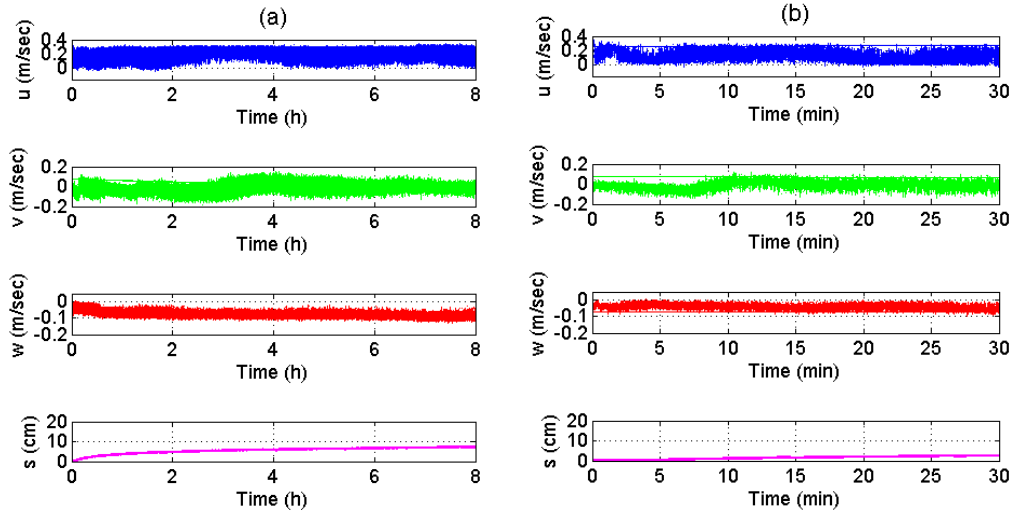


**Figure A.15 :** (a) The change in the velocities and the scour depth over time for 24 cm staggered HACC experiment for 8 hours.(b) The change in the velocities and the scour depth over time for 24 cm staggered HACC experiment for 30 minutes.

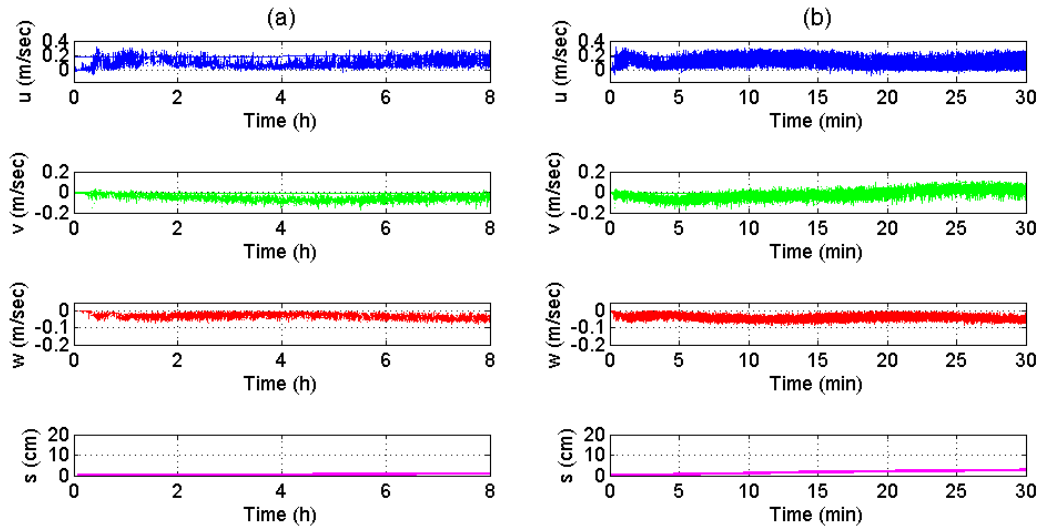


**Figure A.16 :** (a) The change in the velocities and the scour depth over time for 24 cm angled HACC experiment for 8 hours.(b) The change in the velocities and the scour depth over time for 24 cm angled HACC experiment for 30 minutes.

## APPENDIX B

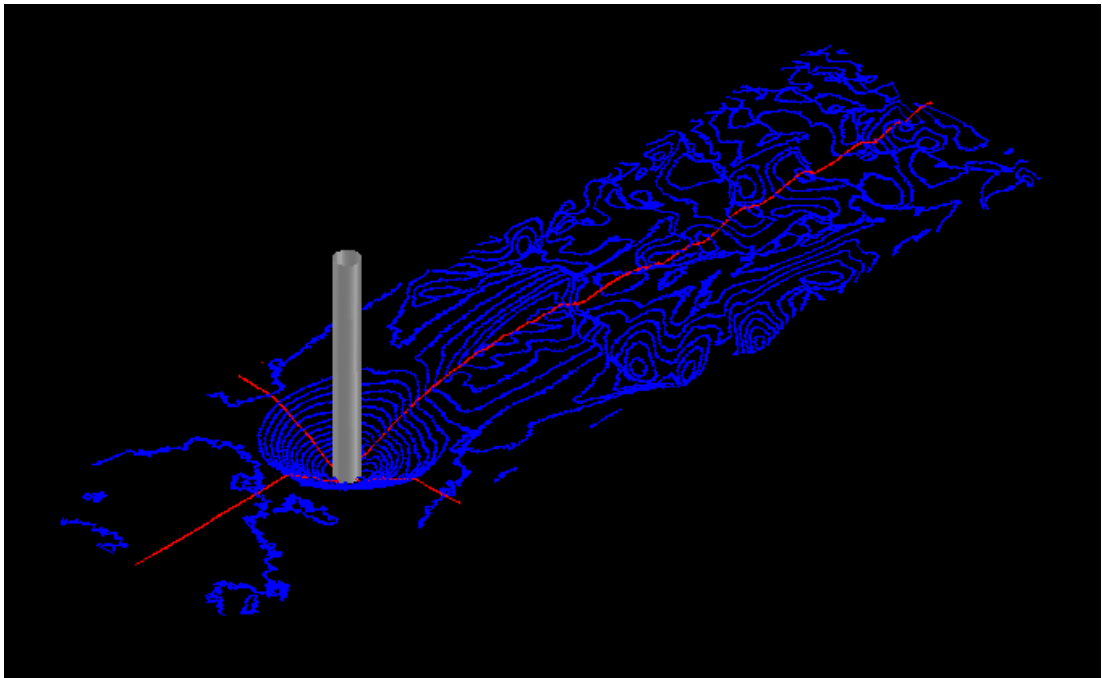


**Figure B.1 :** Contourlines for the final bed topography for 9 cm solid cylinder experiment.

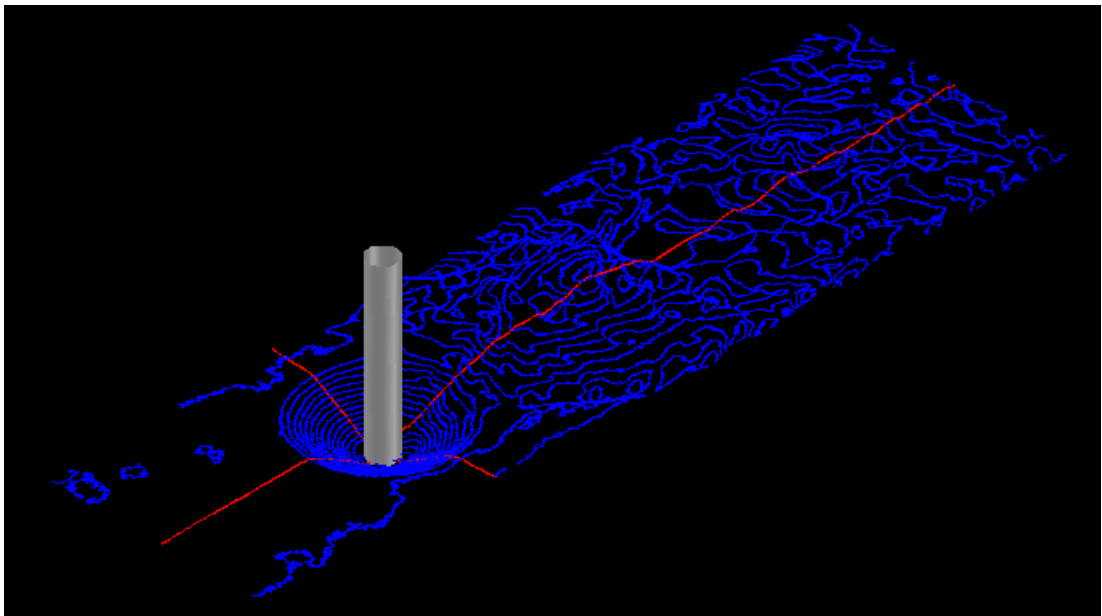


**Figure B.2 :** Contourlines for the final bed topography for 12 cm solid cylinder experiment.

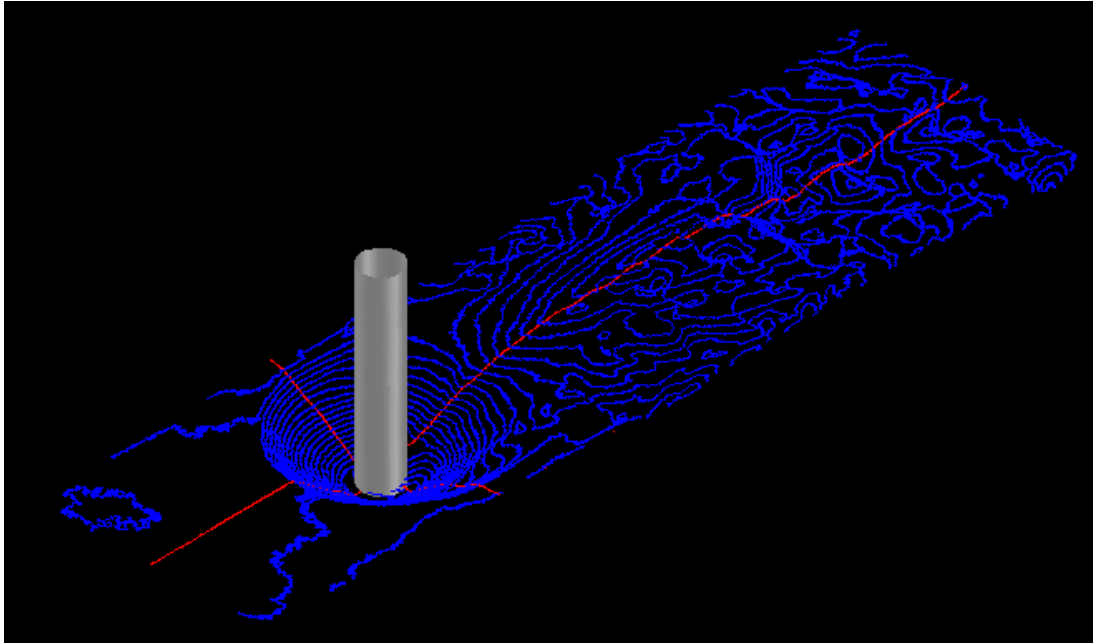


**Figure B.3 :** Contourlines for the final bed topography for 16 cm solid cylinder experiment.

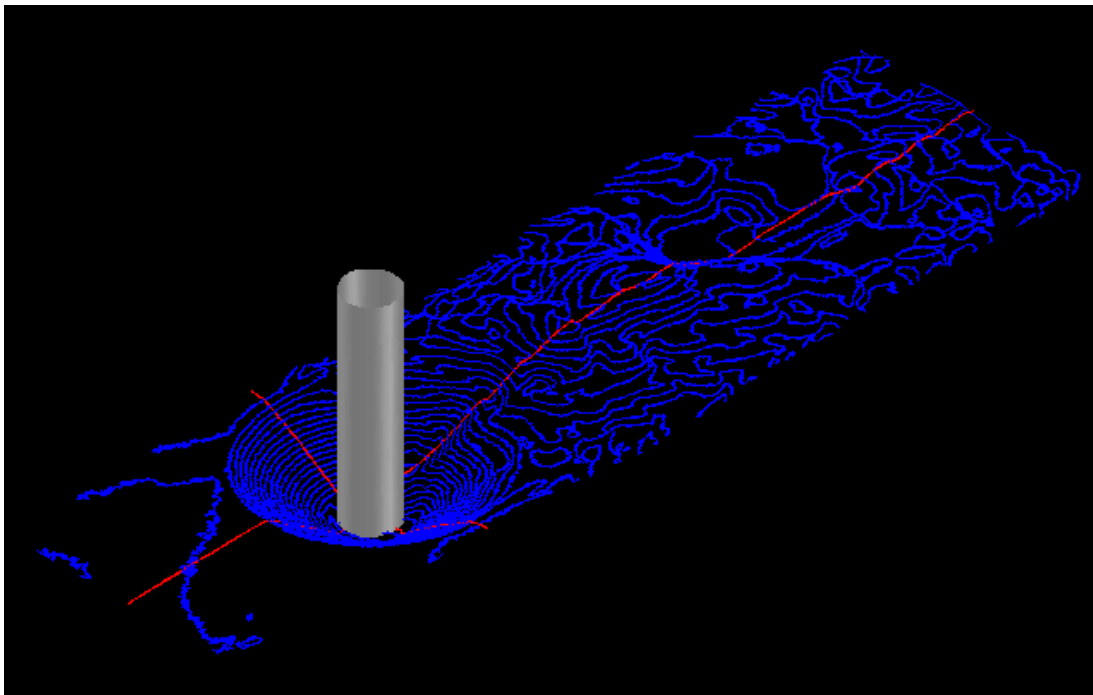


**Figure B.4 :** Contourlines for the final bed topography for 20 cm solid cylinder experiment.



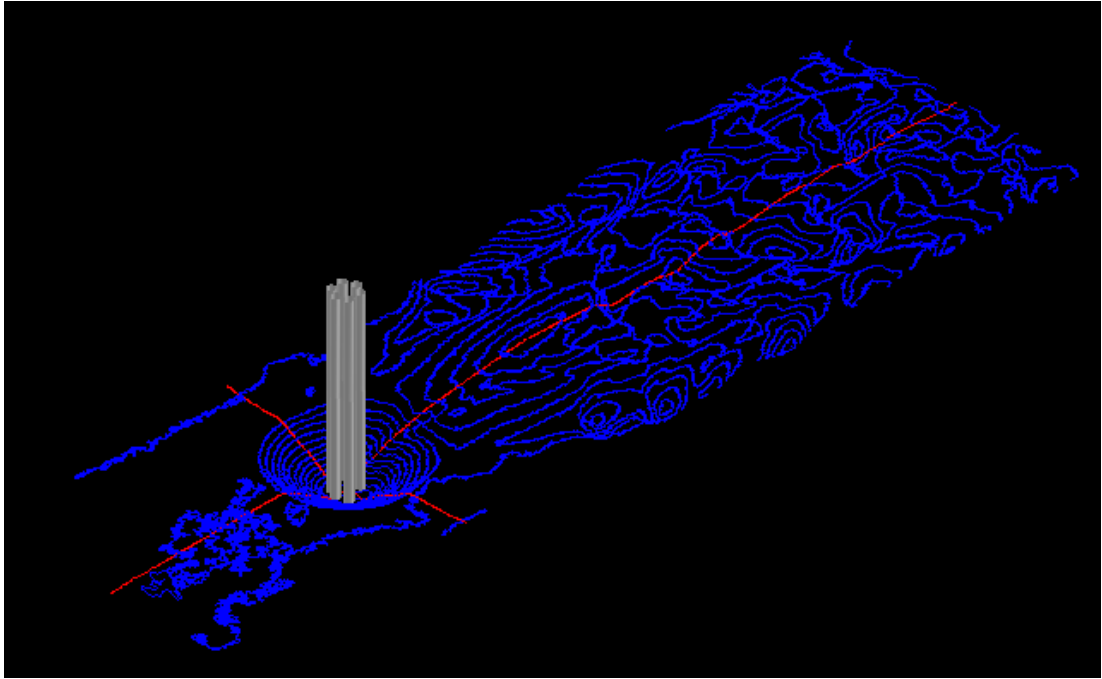


**Figure B.5 :** Contourlines for the final bed topography for 12 cm regular HACC experiment.

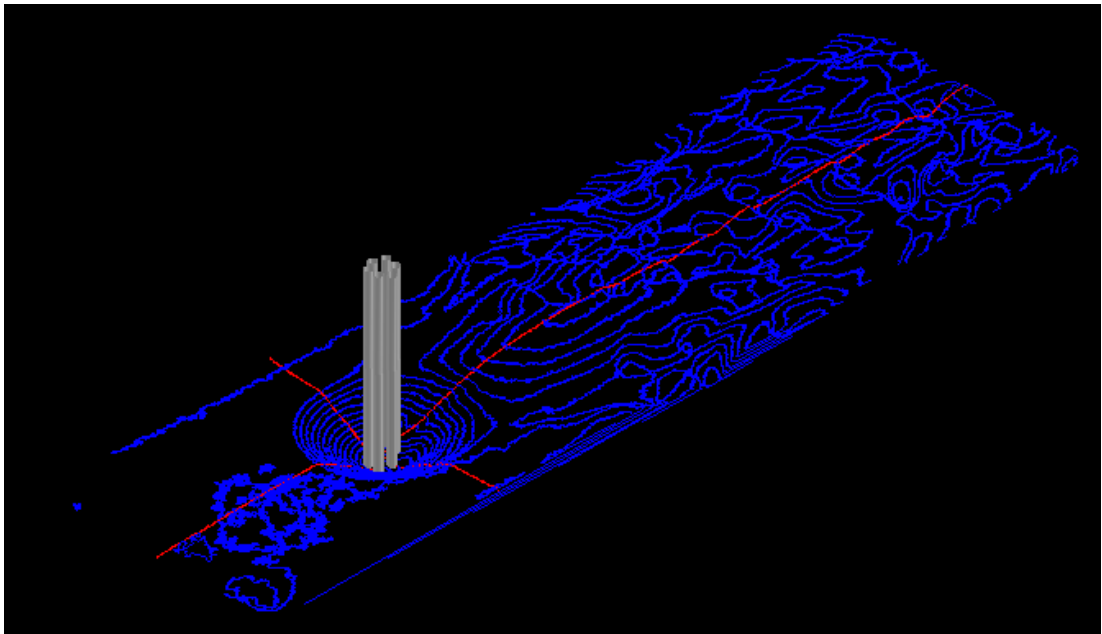


**Figure B.6 :** Contourlines for the final bed topography for 12 cm staggered HACC experiment.

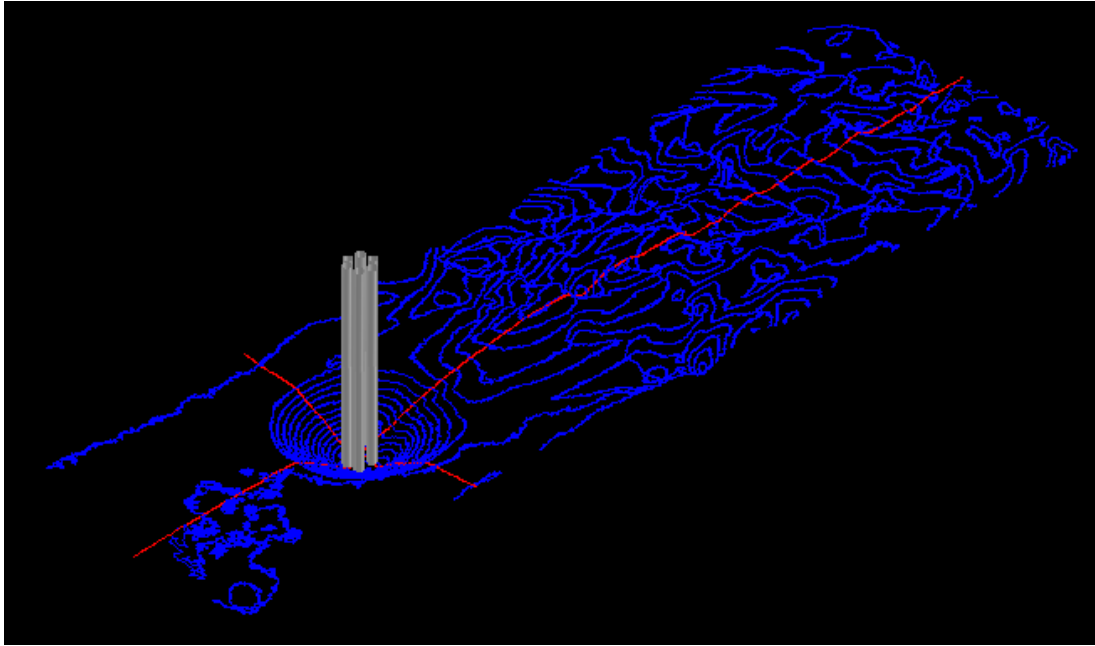


**Figure B.7 :** Contourlines for the final bed topography for 12 cm angled HACC experiment.

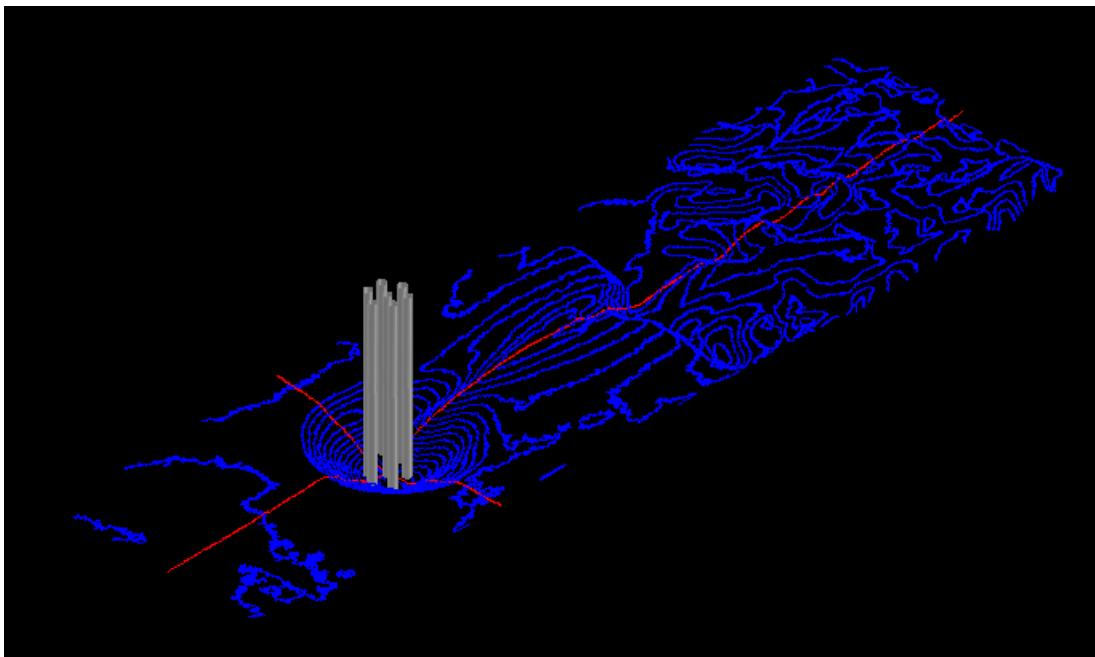


**Figure B.8 :** Contourlines for the final bed topography for 16 cm regular HACC experiment.

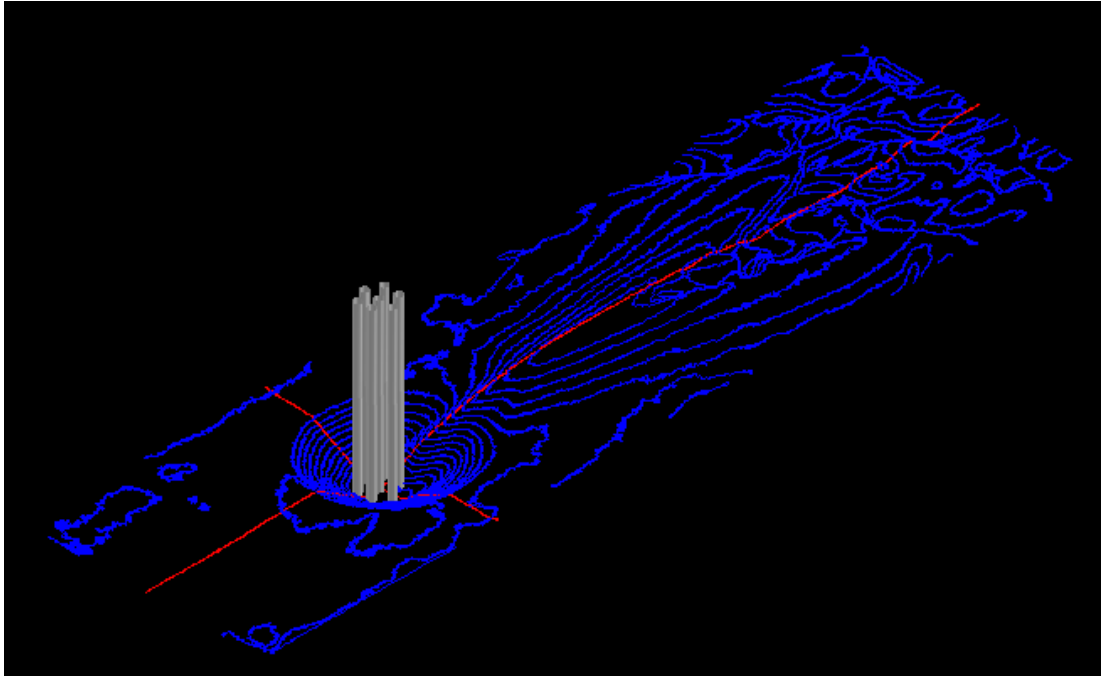


**Figure B.9 :** Contourlines for the final bed topography for 16 cm staggered HACC experiment.

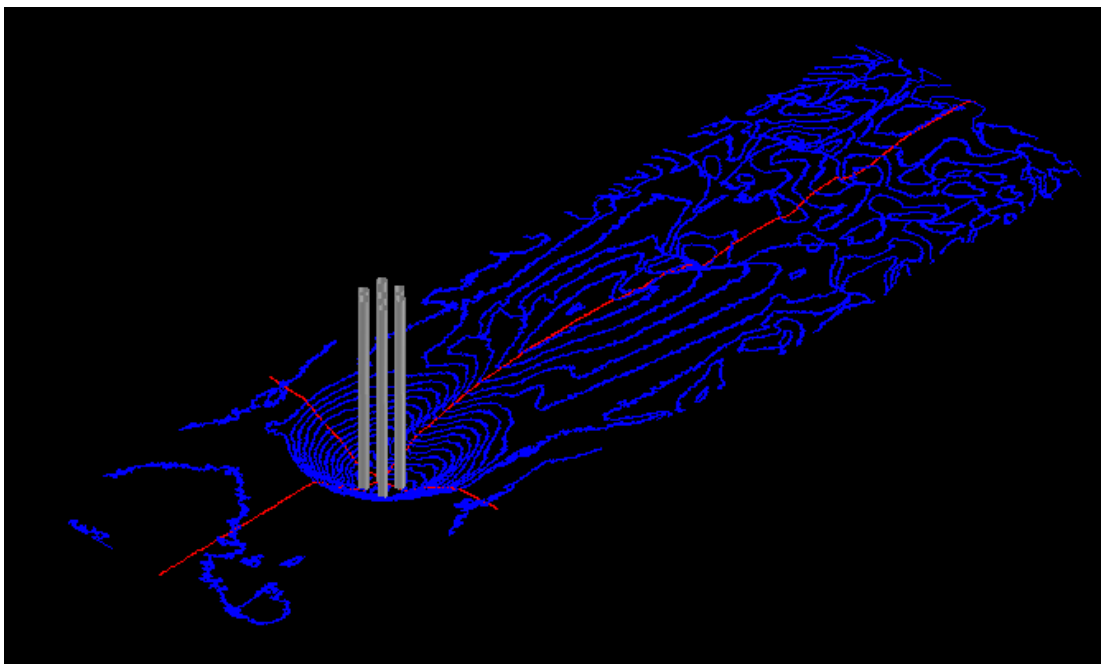


**Figure B.10 :** Contourlines for the final bed topography for 16 cm angled HACC experiment.

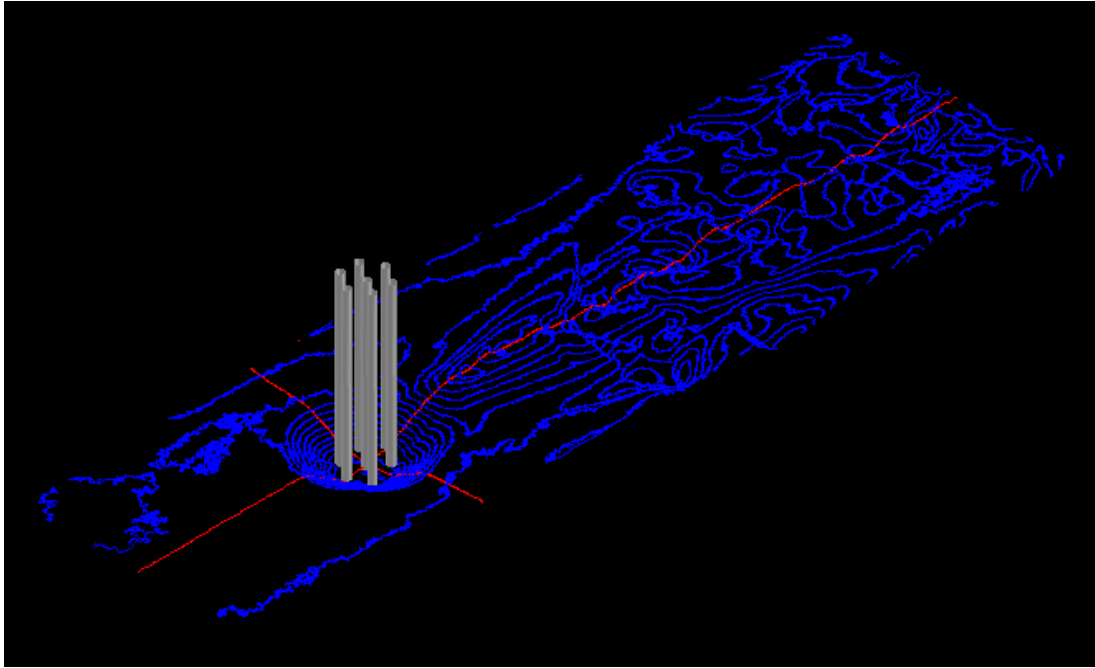


**Figure B.11 :** Contourlines for the final bed topography for 20 cm regular HACC experiment.

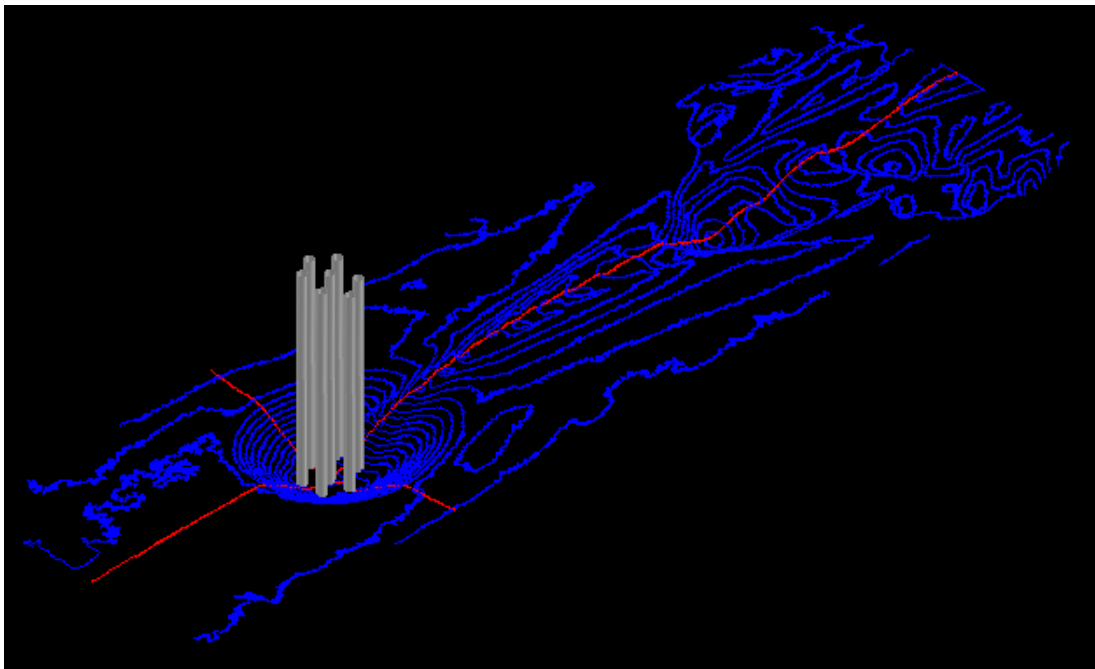


**Figure B.12 :** Contourlines for the final bed topography for 20 cm staggered HACC experiment.

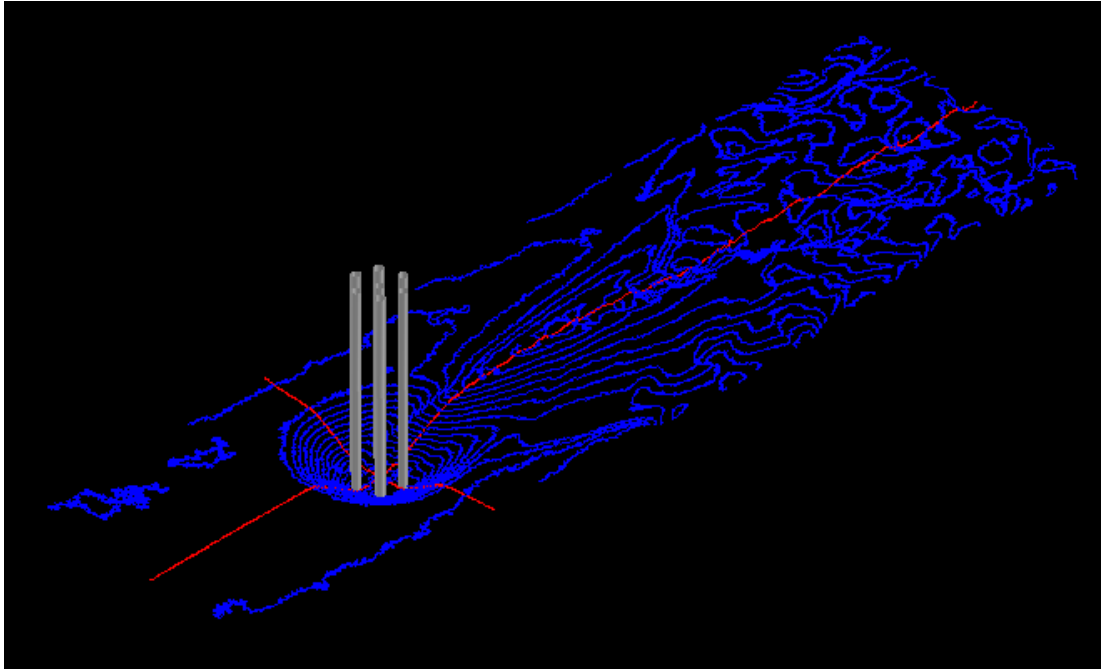


**Figure B.13 :** Contourlines for the final bed topography for 20 cm angled HACC experiment.

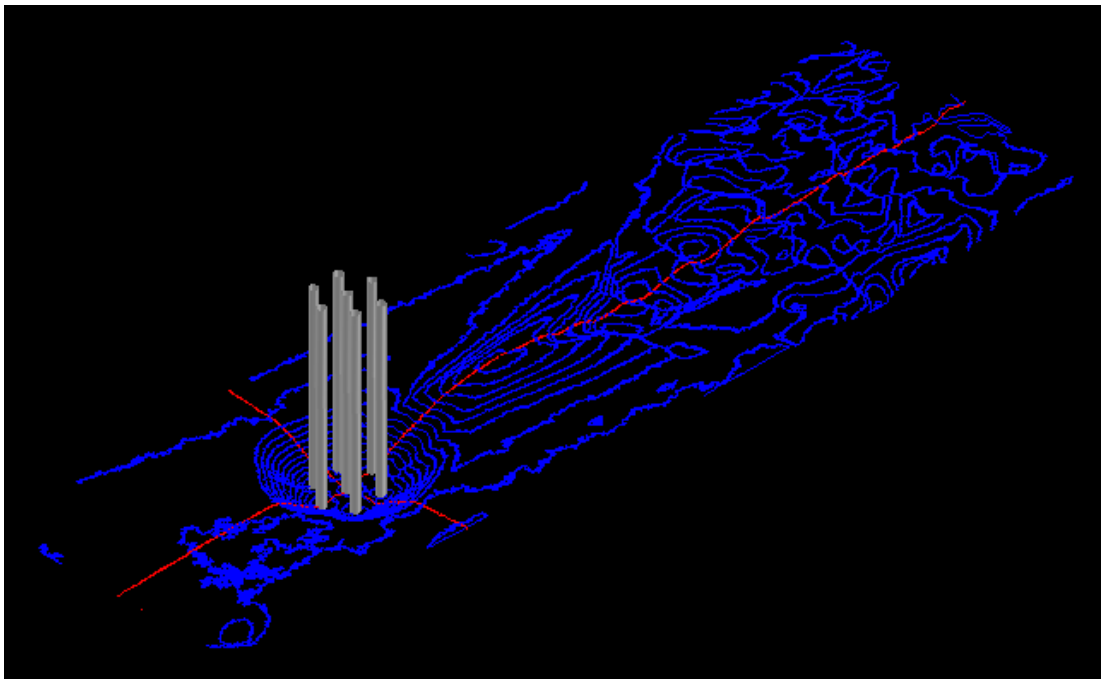


**Figure B.14 :** Contourlines for the final bed topography for 24 cm regular HACC experiment.

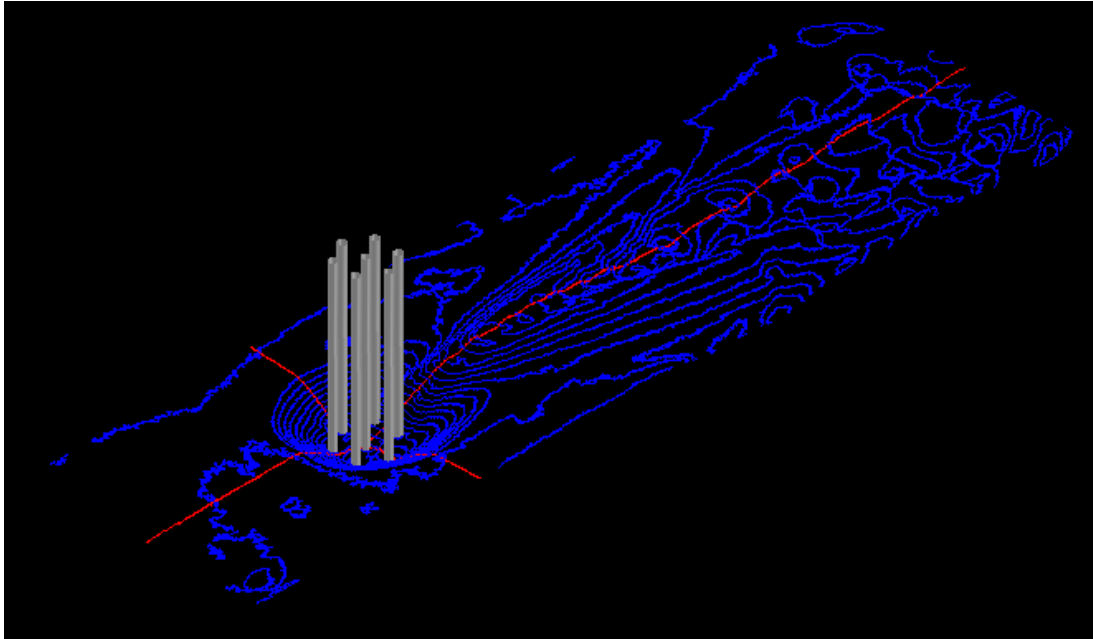


**Figure B.15 :** Contourlines for the final bed topography for 24 cm staggered HACC experiment.

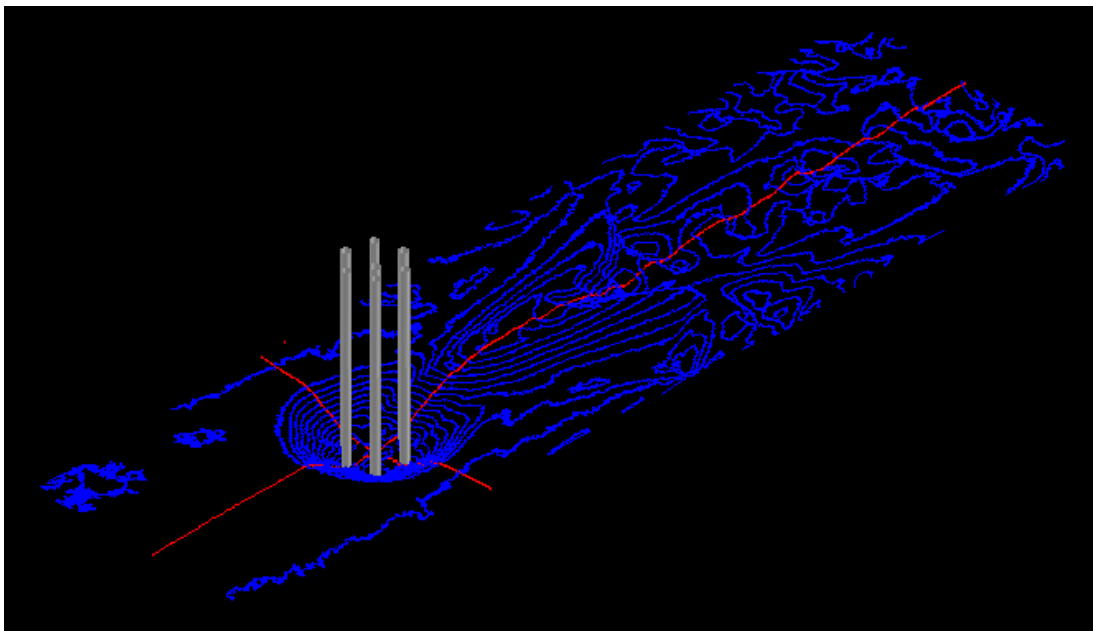


**Figure B.16 :** Contourlines for the final bed topography for 24 cm angled HACC experiment.

## **CURRICULUM VITAE**



**Name Surname** : İşılsu Yıldırım  
**Place and Date of Birth** : Gölcük / 06.05.1991  
**E-Mail** : isilsuyildirim@gmail.com

### **EDUCATION** :

- **B.Sc.** :2009-2014, İstanbul Technical University, Faculty of Civil Engineering, Department of Civil Engineering
- **M.Sc.** :2014-2016, İstanbul Technical University, Department of Civil Engineering, Hydraulics and Water Resources Engineering Programme